Technical Report Documentation Page

1. Report No. SWUTC/12/476660-00027-1	2. Government Accession No.	3. Recipient's Catalog No.

4. Title and Subtitle PREDICTING DAMAGE IN CONCRETE DUE TO EXPANSIVE AGGREGATES: MODELING TO ENABLE SUSTAINABLE MATERIAL DESIGN	5. Report Date April 2012 6. Performing Organization Code
7. Author(s) Syeda Rahman and Zachary Grasley	8. Performing Organization Report No. Report 476660-00027-1
9. Performing Organization Name and Address Texas Transportation Institute Texas A&M University System College Station, Texas 77843-3135	10. Work Unit No. (TRAIS) 11. Contract or Grant No. DTRT07-G-0006
12. Sponsoring Agency Name and Address Southwest Region University Transportation Center Texas Transportation Institute Texas A&M University System College Station, Texas 77843-3135	13. Type of Report and Period Covered Final Report Jan 2011 - Dec 2011 14. Sponsoring Agency Code

15. Supplementary Notes

Supported by a grant from the U.S. Department of Transportation, University Transportation Centers Program.

16. Abstract

A poroelastic model is developed that can predict stress and strain distributions and, thus, ostensibly damage likelihood in concrete under freezing conditions caused by aggregates with undesirable combinations of geometry and constitutive properties. Sensitivity of the stress distributions to the aggregate and matrix constitutive parameters are assessed to allow improved concrete design. The proposed model does not account for the viscoelastic stress relaxation and may over-predict the stress results. The model is evaluated experimentally through acoustic emission analysis under freeze-thaw cyclic loading, which reveals that air-entrained concrete may undergo durability cracking (D-cracking) if deleterious materials are present. It is determined that high-porosity, low-permeability aggregates with fine pore structure are the most vulnerable to D-cracking in non-air-entrained concrete, and the destructive tensile stress is generated at the aggregate boundary by the Mandel-Cryer effect. On the other hand, low-porosity, high-permeability aggregates relax the pore liquid pressure rapidly and prove to be beneficial for the non-air-entrained concrete. Reduction in aggregate size is found to be effective in quickly relaxing the tensile tangential stress, which eventually helps mitigate D-cracking of concrete. The difference between the coefficients of thermal expansion of the coarse aggregate and the matrix in which they are embedded should not be too high since it may cause tensile stress at the aggregate boundary or interfacial transition zone. Low water-to-cement mass ratio and addition of pozzolans help increase the bulk modulus, reduce the porosity of the porous body, and improve durability. It is also observed that increase in cooling rate decreases concrete durability under freezing temperatures through the reduction in time available to relax pore pressure buildup and the related tangential stresses in the aggregate and matrix.

17. Key Words D-Cracking, Poroelastic, Aggregate Size, Porosity, Permeability, Bulk Modulus, Coefficient of Thermal Expansion, Mandel-Cryer Effect, Acoustic Emission	18. Distribution Statement No restrictions. This document is available to the public through NTIS: National Technical Information Service Alexandria, Virginia 22312

19. Security Classif.(of this report) Unclassified	20. Security Classif.(of this page) Unclassified	21. No. of Pages 139	22. Price

Form DOT F 1700.7 **(8-72)** **Reproduction of completed page authorized**

PREDICTING DAMAGE IN CONCRETE DUE TO EXPANSIVE AGGREGATES: MODELING TO ENABLE SUSTAINABLE MATERIAL DESIGN

Prepared by

Syeda Rahman

and

Zachary Grasley

SWUTC/12/476660-00027-1

Southwest Region University Transportation Center
Texas Transportation Institute
Texas A&M University System
College Station, Texas 77843-3135

April 2012

EXECUTIVE SUMMARY

Expansion of aggregates in concrete pavements is often associated with freeze-thaw cycles (resulting in durability cracking [D-cracking]) and alkali-silica reaction (ASR) during wet-dry cycles. The primary focus of this research is to utilize poromechanical modeling to predict D-cracking in concrete due to expansion of aggregates caused by freezing of the aggregates. Sensitivity of the damage growth to the aggregate and matrix constitutive parameters is assessed. This modeling approach could also be utilized to predict damage in concrete due to the formation of ASR gel.

A poroelastic spherical model consisting of an aggregate core surrounded by a cement paste or mortar matrix shell is developed. Using this model, pore pressure, tangential stress, and bulk strain results are analyzed to predict the influence of constitutive parameters on the stress magnitude and damage propensity. The model is evaluated experimentally through acoustic emission analysis under freeze-thaw cyclic loading, which reveals that air-entrained concrete may undergo D-cracking if deleterious materials are used. It is found that low-porosity, low-permeability aggregates embedded in a relatively less stiff matrix may create high tangential tensile stress in the interfacial transition zone. This damage can be prevented if a high-porosity, high-permeability (e.g., lightweight) aggregate and stiff matrix are used.

It is determined that high-porosity, low-permeability aggregates with fine pore structure are the most vulnerable to D-cracking in non-air-entrained concrete, and the destructive tensile stress is generated at the aggregate boundary by the Mandel-Cryer effect. This Mandel-Cryer effect is induced by the strain differential caused by the expansive aggregate center. On the other hand, low-porosity, high-permeability aggregates relax the pore liquid pressure rapidly and prove to be beneficial for the non-air-entrained concrete. Moreover, reduction in aggregate size is found to be effective in quickly relaxing the tensile tangential stress, which eventually helps mitigate D-cracking of concrete under freezing temperatures.

It is observed that the difference between the coefficients of thermal expansion (CTEs) of the coarse aggregate and the matrix in which they are embedded should not be too high since it may cause tensile stress at the aggregate boundary or interfacial transition zone (ITZ). Higher CTE of the high-porosity, low-permeability aggregate may exacerbate D-cracking by

substantially increasing the delayed tensile tangential stress at the aggregate boundary induced by the Mandel-Cryer effect.

It is found that a high-porosity, low-permeability aggregate and a less stiff matrix may deteriorate concrete resistance to D-cracking. Low water-to-cement mass ratio (w/c) and addition of pozzolans help increase the bulk modulus, reduce the porosity of the porous body, and improve durability. It is also observed that increase in cooling rate decreases concrete durability under freezing temperatures through the reduction in time available to relax pore pressure buildup and the related tangential stresses in the aggregate and matrix.

The proposed model is a poroelastic model and may over-predict the stress since it does not account for the viscoelastic stress relaxation. Dependence of saturation on pore pressure, presence of dissolved species in the pore fluid, presence of entrapped air pockets inside the concrete, degradation of material properties with damage and time, and interaction between aggregate particle stress/strain fields are neglected to avoid complications in the solutions.

Other than including the above-mentioned factors that have been neglected to simplify the analytical solution, this model can be modified to account for the damage caused by the expansion of the alkali-silica hydrate gel during ASR reaction and degradation. The gel can be treated as a separate band of material in between the matrix shell and the aggregate core, or it can be treated as an integrated part of the expansive aggregate core that develops tensile tangential stress in the matrix. In addition, incorporation of an appropriate fatigue-based damage model for both D-cracking and ASR problems will further improve the model and help predict damage caused by the expansive aggregates.

TABLE OF CONTENTS

LIST OF FIGURES

LIST OF TABLES

DISCLAIMER

ACKNOWLEDGMENT

The authors recognize that support for this research was provided by a grant from the U.S. Department of Transportation, University Transportation Centers Program to the Southwest Region University Transportation Center. The authors would like to thank Dr. Kyle A. Riding and Brett Blackwell from Kansas State University for their collaborative work and supply of specimens.

1 INTRODUCTION

Based on previous Texas Transportation Institute (TTI) research, the Federal Highway Administration (FHWA) reported that about 10% of the nation's 208,000 km (129,000 mi) of Portland cement concrete pavements was affected by damage due to expansion of aggregates in 1997 [1], with the percentage likely much higher now. Expansion of aggregates in concrete pavements is often associated with freeze-thaw cycles (resulting in durability cracking [D-cracking]) and alkali-silica reaction (ASR) during wet-dry cycles. On average, pavements distressed by expansive aggregate-induced damage will require extensive rehabilitation after 10 years of service. Texas and other states have a severe problem with both ASR and D-cracking, as demonstrated by the many research projects sponsored by the state departments of transportation (DOTs) in this region dealing with these topics. However, while much research has already been performed and millions of dollars expended studying ASR and D-cracking, the research has thus far focused primarily on empirical or semi-empirical experimental investigations of mechanisms and/or effects on structural capacity. Little work has been done to investigate the role of mechanics and constitutive properties of concrete phases in the formation and growth of damage in concrete due to ASR and freezing of aggregates.

Reducing the temperature of concrete below 0° C may cause aggregates within the concrete to expand (due to freezing of pore water and associated pore water pressure), causing tensile stresses in the surrounding cement paste matrix. The extent of the expansion and resulting damage depends on many factors, including the pore structure of the aggregates and surrounding cement paste, the rate of temperature change and minimum temperature achieved, and the mechanical properties of the aggregates and cement paste. Poroelastic theory [2], [3] has been used successfully to model the behavior of cement paste exposed to freezing temperatures [4–7] but has not been applied to the problem of freezing aggregates within concrete.

ASR involves the dissolution of certain glassy siliceous aggregates within concrete and the subsequent formation of an amorphous alkali-silica hydrate that imbibes water. The imbibition of water results in swelling of the gel, which creates tensile stresses in the surrounding cement paste and subsequent damage growth. The magnitude of the stress in the cement paste surrounding the expanding gel-coated aggregate depends on the mechanical properties of the aggregate, gel, and cement paste, but also potentially on the pore structure of the aggregate and cement paste. Since the gel is a viscoelastic material, it may flow through the pore network under shear stresses, which would relax stresses in the paste. Poroelasticity has been applied to the ASR problem [8] but has not been utilized to study the magnitude of the stress relaxation possible by optimizing material parameters.

The primary focus of this research was to utilize poromechanical modeling to predict D-cracking in concrete due to expansion of aggregates caused by freezing of the aggregates. This modeling approach can also be utilized to predict damage in concrete due to the formation of ASR gel.

D-cracking, which appears as a series of closely spaced, crescent-shaped cracks along joints in concrete slabs, is a progressive structural deterioration of the concrete beginning in certain types of susceptible coarse aggregates and caused by repeated freezing and thawing after absorbing moisture [9–11]. It is initiated when moisture penetrates the tiny pores of certain types of aggregates (some limestones and fine-grained sedimentary rocks). When frozen, the trapped moisture expands to form ice. As thawing occurs, more moisture is able to penetrate the newly formed cracks created by the destructive expansion of the previous freeze. The next freeze then produces more destructive cracking, and so on. Large particles of the same type are more susceptible to D-cracking than small particles. This is because the larger the particle, the longer the water flow path, and the more cracks will form, since the water cannot escape during freezing. Again, the higher the permeability, the faster water can escape during freezing, causing less damage. Therefore, in the same material, the smaller size aggregates with high permeability perform better than the larger ones. The problem is less prevalent in very cold regions where fewer cycles of freezing occur.

When the temperature of concrete is reduced below 0 °C, aggregates within the concrete may undergo cryo-deformation due to freezing of pore water and associated pore water pressure, causing tensile stress gradient in the surrounding cement paste matrix. Powers first came up with a hydraulic pressure model, which illustrates that when water in the pore network freezes to ice, liquid pressure is built up by the expulsion of excess water due to the increase in volume [12]. As a result, cracks develop when the concrete strength fails to resist the excess pressure. Powers proposed that suitably spaced air voids would prevent the development of the excess pore pressure. However, subsequent work by Powers and Helmuth showed that air-entrained pastes still suffer stress and expansion caused by the crystallization pressure [13]. The importance of crystallization pressure was later expanded by Scherer and Valenza, who concluded that the primary source of stress during freezing is the crystallization pressure, not the hydraulic pressure [14]. In support of the crystallization pressure mechanism, they referred to the work of Beaudoin and MacInnis, which showed that concrete still expands when water is replaced by organic liquid, which contracts upon freezing, since expansive hydraulic pressure is absent in this case [15]. According to this mechanism, the harmful stress is created by the repulsive van der Waals forces between the ice crystal and the minerals in the pore walls. At the ice, water, and mineral interface, additional attributions to the disjoining pressure may come from the electrostatic forces or the structuring of the solvent at the solid surface. This repulsion is so high in magnitude that a liquid film separating the ice and pore walls always exists and permits the crystal to grow while pushing away the pore walls [14].

In addition to these two mechanisms, at a temperature below the bulk freezing point, confined water can partially remain liquid provided it depressurizes relative to the adjacent ice crystals, provoking in turn a cryo-pumping of the distant liquid water [5]. As a result, properly air-entrained concrete contracts upon freezing because the liquid water transforms to ice instantaneously when entering entrained air voids and causes cryo-suction in the air-void vicinity owing to the liquid-crystal thermodynamic equilibrium [4], [5], [13], [14], [16]. In this regard, Coussy, and Coussy and Monteiro, attributed freeze-thaw-induced damage to the following various combined actions [5], [6]:

- The difference of density between the liquid water and the ice crystal; this density difference provokes the expansion of the solid matrix surrounding the crystal in formation, as well as the expulsion of some liquid water from the freezing sites toward the pores still filled by liquid water.
- The surface tension arising between the different constituents, which eventually governs the crystallization process in connection with the pore radius distribution.
- The drainage of the liquid water expelled from the freezing sites toward the air voids.
- The cryo-suction process, which drives liquid water toward the already-frozen sites as the temperature further decreases.
- The elastic thermomechanical coupling between the pressurized pore space and the surrounding solid matrix, which governs the overall cryo-deformation.

The proposed poromechanical model accounts for the above-mentioned damage mechanisms and predicts D-cracking in the concrete caused by freezing temperatures. Using this model, a sensitivity of the damage growth to the aggregate and matrix constitutive parameters is assessed. This, in turn, will allow improved concrete design and spawn new ideas for preventing and mitigating damage due to expansive aggregates.

2 MODEL DEVELOPMENT

In this chapter, a poroelastic concrete sphere is considered with a coarse aggregate core of radius R_i embedded inside a mortar or cement paste matrix shell (throughout this report, the terms “aggregate” and “matrix” will be used to represent the coarse aggregate core and the paste or mortar shell, respectively) of outer radius R_o , as shown in Figure 4. An elastic model is first developed based on the classical elastic theory proposed by Timoshenko and Goodier [17]. It is then extended to include poromechanical constitutive properties based on the theory developed by Biot [2] and discussed by Coussy [3], [5], and Coussy and Monteiro [6], [7]. The elastic case is presented in Section 2.1, and the unsaturated poroelasticity is presented in Section 2.2. Throughout this report, the following sign convention is used:

- Pore pressure (liquid or crystal) is positive for compression and negative for suction or tension.
- Stress and strain are positive for tension and negative for compression.
- Change in temperature, ΔT (= T_m-T), is positive for cooling and negative for heating, since it is measured with respect to the melting temperature T_m in the absolute scale.

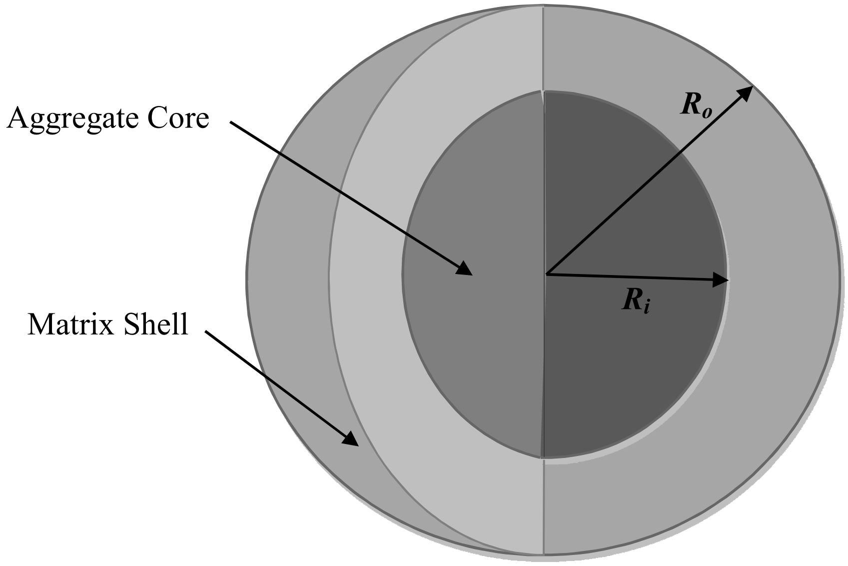

Figure 4. Geometry of the proposed model representing a coarse aggregate core of radius R_i embedded in a cement paste or mortar matrix shell of outer radius R_o.

2.1 Elasticity

Determination of the elastic stress and strain components given in this section follows much of Timoshenko and Goodier's work [17], with the only exception being that thermal strain is replaced by free strain. A simple case of a temperature symmetrical with respect to the center and a function of radius, *r*, is considered. On account of the axial symmetry, the non-zero radial (subscript *r*) and two tangential (subscript *θ* and □) stress (σ) and strain (ε) components in the principal directions are given by:

$$\sigma_r = \frac{3K}{(1+\nu)}[(1-\nu)\varepsilon_r + 2\nu\varepsilon_t - (1+\nu)\varepsilon_f] \tag{0}$$

$$\sigma_\theta = \sigma_\phi = \frac{3K}{(1+\nu)}[\varepsilon_t + \nu\varepsilon_r - (1+\nu)\varepsilon_f] \tag{0}$$

$$\varepsilon_r = \frac{\partial u_r}{\partial r} \tag{0}$$

$$\varepsilon_\theta = \varepsilon_\phi = \frac{u_r}{r} \qquad (0)$$

where u_r is the radial deformation, *K* and *v* are the bulk modulus and the Poisson's ratio of the isotropic linear elastic porous material, and ε_f is the free strain and a function of pore pressure and temperature. The above stress components must satisfy the condition of equilibrium given by:

$$\frac{d\sigma_r}{dr} + \frac{2}{r}(\sigma_r - \sigma_t) = 0 \qquad (0)$$

Substituting (0)–(0)in the equilibrium equation (0), we get the differential equation for u_r:

$$(1-\nu)\frac{d^2u_r}{dr^2} + \frac{2\nu}{r^2}\left(r\frac{du_r}{dr} - u_r\right) - (1+\nu)\frac{d}{dr}(\varepsilon_f) + (1-2\nu)\frac{2}{r}\frac{du_r}{dr} - (1-2\nu)\frac{2u_r}{r^2} = 0 \qquad (0)$$

which can be simplified as:

$$(1-\nu)\frac{d^2u_r}{dr^2} + \frac{2\nu}{r}\frac{du_r}{dr} - \frac{2\nu u_r}{r^2} + (1-2\nu)\frac{2}{r}\frac{du_r}{dr} - (1-2\nu)\frac{2u_r}{r^2} = (1+\nu)\frac{d}{dr}(\varepsilon_f)$$

$$\Rightarrow (1-\nu)\frac{d^2u_r}{dr^2} + (1-\nu)\frac{2}{r}\frac{du_r}{dr} - (1-\nu)\frac{2u_r}{r^2} = (1+\nu)\frac{d}{dr}(\varepsilon_f)$$

$$\Rightarrow \frac{d^2u_r}{dr^2} + \frac{2}{r}\frac{du_r}{dr} - \frac{2u_r}{r^2} = \frac{(1+\nu)}{(1-\nu)}\frac{d}{dr}(\varepsilon_f)$$

$$\Rightarrow \frac{d}{dr}\left[\frac{1}{r^2}\frac{d}{dr}(r^2u_r)\right] = \frac{(1+\nu)}{(1-\nu)}\frac{d}{dr}(\varepsilon_f) \qquad (0)$$

Integrating both sides of (0) with respect to *r*, we get:

$$\frac{1}{r^2}\frac{d}{dr}(r^2u_r) = \frac{(1+\nu)}{(1-\nu)}\varepsilon_f + C_1' \qquad (0)$$

where C_1' is the first integration constant. Rearranging (0) and then integrating again with respect to *r*, we find:

$$r^2u_r = \frac{(1+\nu)}{(1-\nu)}\int_{r=a}^{r=r}\varepsilon_f r^2 dr + C_1'\frac{r^3}{3} + C_2 \qquad (0)$$

where C_2 is the second integration constant. Finally, after simplification, the solution can be written as:

$$u_r = \frac{(1+\nu)}{(1-\nu)} \frac{1}{r^2} \int_{r=a}^{r=r} \varepsilon_f r^2 dr + C_1 r + \frac{C_2}{r^2} \tag{0}$$

This solution can be substituted in equations (0)–(0) to obtain:

$$\varepsilon_r = -2\frac{(1+\nu)}{(1-\nu)} \frac{1}{r^3} \int_{r=a}^{r=r} \varepsilon_f r^2 dr + \frac{(1+\nu)}{(1-\nu)} \varepsilon_f + C_1 - \frac{2C_2}{r^3} \tag{0}$$

$$\varepsilon_\theta = \varepsilon_\phi = \frac{(1+\nu)}{(1-\nu)} \frac{1}{r^3} \int_{r=a}^{r=r} \varepsilon_f r^2 dr + C_1 + \frac{C_2}{r^3} \tag{0}$$

$$\sigma_r = -6K \frac{(1-2\nu)}{(1-\nu)} \frac{1}{r^3} \int_{r=a}^{r=r} \varepsilon_f r^2 dr + 3KC_1 - \frac{(1-2\nu)}{(1+\nu)} \frac{6K}{r^3} C_2 \tag{0}$$

$$\sigma_\theta = \sigma_\phi = 3K \frac{(1-2\nu)}{(1-\nu)} \frac{1}{r^3} \int_{r=a}^{r=r} \varepsilon_f r^2 dr - 3K\varepsilon_f + 3KC_1 + \frac{(1-2\nu)}{(1+\nu)} \frac{3K}{r^3} C_2 \tag{0}$$

We will now consider aggregate core and matrix shell separately. For aggregate core, the lower limit *a* of the integrals will be taken as zero. At the center (*r = 0*), radial displacement is zero, which from (0) gives $C_2 = 0$, since $\lim_{r \to 0} \frac{1}{r^2} \int_{r=0}^{r=r} \varepsilon_f{}^a r^2 dr = 0$. This means the term with C_2 vanishes for aggregates. Rewriting equations (0)–(0)for aggregates and denoting by superscript *a,* we obtain:

$$u_r{}^a = \frac{(1+\nu^a)}{(1-\nu^a)} \frac{1}{r^2} \int_{r=0}^{r=r} \varepsilon_f{}^a r^2 dr + C_1^a r \tag{0}$$

$$\varepsilon_r{}^a = -2\frac{(1+\nu^a)}{(1-\nu^a)} \frac{1}{r^3} \int_{r=0}^{r=r} \varepsilon_f{}^a r^2 dr + \frac{(1+\nu^a)}{(1-\nu^a)} \varepsilon_f{}^a + C_1^a \tag{0}$$

$$\varepsilon_\theta{}^a = \varepsilon_\phi{}^a = \frac{(1+\nu^a)}{(1-\nu^a)} \frac{1}{r^3} \int_{r=0}^{r=r} \varepsilon_f{}^a r^2 dr + C_1^a \tag{0}$$

$$\sigma_r{}^a = -6K^a \frac{(1-2\nu^a)}{(1-\nu^a)} \frac{1}{r^3} \int_{r=0}^{r=r} \varepsilon_f{}^a r^2 dr + 3K^a C_1^a \tag{0}$$

$$\sigma_\theta{}^a = \sigma_\phi{}^a = 3K^a \frac{(1-2\nu^a)}{(1-\nu^a)} \frac{1}{r^3} \int_{r=0}^{r=r} \varepsilon_f{}^a r^2 dr - 3K^a \frac{(1-2\nu^a)}{(1-\nu^a)} \varepsilon_f{}^a + 3K^a C_1^a \tag{0}$$

In the case of the matrix shell, the lower limit of the integral is taken to be the radius at the interface of the aggregate core and the matrix shell, R_i. Rewriting equations (0)–(0) for paste or mortar matrix and denoting by superscript p, we find:

$$u_r{}^p = \frac{\left(1+\nu^p\right)}{\left(1-\nu^p\right)} \frac{1}{r^2} \int_{r=R_i}^{r=r} \varepsilon_f{}^p r^2 dr + C_1{}^p r + \frac{C_2{}^p}{r^2} \tag{0}$$

$$\varepsilon_r{}^p = -2\frac{\left(1+\nu^p\right)}{\left(1-\nu^p\right)} \frac{1}{r^3} \int_{r=R_i}^{r=r} \varepsilon_f{}^p r^2 dr + \frac{\left(1+\nu^p\right)}{\left(1-\nu^p\right)} \varepsilon_f{}^p + C_1{}^p - \frac{2C_2{}^p}{r^3} \tag{0}$$

$$\varepsilon_\theta{}^p = \varepsilon_\phi{}^p = \frac{\left(1+\nu^p\right)}{\left(1-\nu^p\right)} \frac{1}{r^3} \int_{r=R_r}^{r=r} \varepsilon_f{}^p r^2 dr + C_1{}^p + \frac{C_2{}^p}{r^3} \tag{0}$$

$$\sigma_r{}^p = -6K^p \frac{\left(1-2\nu^p\right)}{\left(1-\nu^p\right)} \frac{1}{r^3} \int_{r=R_i}^{r=r} \varepsilon_f{}^p r^2 dr + 3K^p C_1{}^p - \frac{\left(1-2\nu^p\right)}{\left(1+\nu^p\right)} \frac{6K^p}{r^3} C_2{}^p \tag{0}$$

$$\sigma_t{}^p = 3K^p \frac{\left(1-2\nu^p\right)}{\left(1-\nu^p\right)} \frac{1}{r^3} \int_{r=R_i}^{r=r} \varepsilon_f{}^p r^2 dr - 3K^p \frac{\left(1-2\nu^p\right)}{\left(1-\nu^p\right)} \varepsilon_f{}^p + 3K^p C_1{}^p + \frac{\left(1-2\nu^p\right)}{\left(1+\nu^p\right)} \frac{3K^p}{r^3} C_2{}^p \tag{0}$$

The three unknown integration constants, C_1^a, C_1^p, and C_2^p, are determined using the Solve function Solve in Mathematica [18] and applying the following three boundary conditions. The boundary conditions are:

- At the aggregate core-matrix shell interface ($r = R_i$), radial displacement and radial stress are the same in the matrix and aggregate, so:

  $\left[u_r{}^a\right]_{r=R_i} = \left[u_r{}^p\right]_{r=R_i}$ in order to ensure a continuous displacement field, and (0)

  $\left[\sigma_r{}^a\right]_{r=R_i} = \left[\sigma_r{}^p\right]_{r=R_i}$ to satisfy equilibrium. (0)

- At the outer surface ($r = R_o$) of the matrix shell, radial stress, $\sigma_r{}^p$, is equal to the negative applied pressure, p_{app}, so:

  $$\left[\sigma_r{}^p\right]_{r=R_o} = -p_{app} \tag{0}$$

- The Mathematica notebook with the determination of the integration constants is provided in the Appendix. Substituting the integration constants in the equation of bulk strain, $\varepsilon_{kk} = \varepsilon_r + \varepsilon_\theta + \varepsilon_\phi$, for aggregate core, we obtain:

$$\varepsilon_{kk}{}^{a} = X\left\langle \varepsilon_{f}{}^{a}\right\rangle + 3\beta\varepsilon_{f}{}^{a} + W\left\langle \varepsilon_{f}{}^{p}\right\rangle - \frac{p_{app}R_o^3}{Z}\left(1+2\chi_{p}{}^{p}\right) \tag{0}$$

and for matrix shell:

$$\varepsilon_{kk}{}^{p} = U\left\langle \varepsilon_{f}{}^{a}\right\rangle + 3\beta^{p}\varepsilon_{f}{}^{p} + V\left\langle \varepsilon_{f}{}^{p}\right\rangle - \frac{p_{app}R_o^3}{Z}\frac{\left(K^{a}+2K^{p}\chi^{p}\right)}{K^{p}} \tag{0}$$

where the angle brackets indicate a volumetric average, such that:

$$\left\langle x\right\rangle = \frac{3}{b^3-a^3}\int_a^b x\left(r\right)\, r^2 dr \tag{0}$$

$$\beta = \frac{1+\nu}{3\left(1-\nu\right)} \tag{0}$$

$$\chi = \frac{1-2\nu}{1+\nu} \tag{0}$$

Superscripts *a* and *p* denote aggregate and matrix, respectively. Coefficients *U*, *V*, *W*, *X*, and *Z* are functions of material constants and are given in the Appendix.

2.2 Unsaturated Poroelasticity

The fundamental equations needed to model the deformations in concrete exposed to freezing conditions, including thermal effect, hydraulic pressure, and cryo-suction, have already been developed by Coussy [3] and Coussy and Monteiro [6], [7].These equations are modified to determine the damage in concrete caused by the harmful aggregates under the freeze-thaw cycle. For simplicity, the following assumptions are made:

- We assume that the rate of thermal equilibration is orders of magnitude faster than the fluid flux such that a uniform temperature (T) field in our model is a reasonable approximation.
- Ice and water flow so slowly in comparison to the cooling timescale that change in liquid or crystal saturation is assumed to be uniform and instantaneous with the applied change in temperature.
- When cooling freezes water in the pore network, ice blocks the passages and reduces permeability. Dependence of the poromechanical properties (e.g., permeability and viscosity) and the thermal properties (e.g., coefficient of thermal expansion [CTE] of liquid water) on the temperature was neglected and assumed to be constant with time.

- Damage accretion with each successive freeze-thaw cycle and subsequent change in poromechanical properties (e.g., permeability, Biot's coefficient and modulus, bulk modulus) were also neglected.

For a porous material under freezing condition, the solid-liquid thermodynamic equilibrium is given by [19]:

$$(1-\rho_c/\rho_l)(p_l-p_{atm})+p_c-p_l=\Sigma_m(T_m-T)=\Sigma_m\Delta T \tag{0}$$

where ρ_c and ρ_l are the un-deformed densities of the crystalline and liquid phases, respectively; p_c and p_l are the pressures in the crystalline and liquid phases, respectively; T_M is the melting temperature for water when the radius of curvature is infinite; T is the melting temperature for water when the mean radius of interfacial curvature is d ; ΔT is the change in temperature; and p_{atm} is the atmospheric pressure. The term $\Sigma_m=(s_l-s_c)$ is the mass-specific melting entropy where s_c and s_l are the mass-specific entropies of the crystalline and liquid phases, respectively. The constitutive law for a linear isotropic thermoelastic porous material subjected to uniform pore pressure p can be expressed as [20]:

$$\boldsymbol{\varepsilon}=\frac{1}{2G}\left[\boldsymbol{\sigma}-\frac{\nu}{1+\nu}\operatorname{tr}(\boldsymbol{\sigma})\mathbf{I}\right]+\frac{b}{3K}p\mathbf{I}-\alpha\Delta T\mathbf{I} \tag{0}$$

where $\boldsymbol{\varepsilon}$ is the strain tensor, $\boldsymbol{\sigma}$ is the externally applied stress tensor, G is the shear modulus of the porous body, p is the pressure within the pore fluid, α is the linear CTE of the porous body, and $\mathbf{I}$ is the identity tensor. The term b is Biot's coefficient and can be written as:

$$b=1-\frac{K}{K_s} \tag{0}$$

where K_s is the bulk modulus of the solid phase comprising the solid skeleton. Under stress-free condition ($\boldsymbol{\sigma}=0$), equation (0) simplifies to:

$$\varepsilon_f=\frac{bp}{3K}-\alpha\Delta T \tag{0}$$

such that:

$$\varepsilon_d=3\varepsilon_f=\frac{bp}{K}-3\alpha\Delta T \tag{0}$$

where ε_d is the scalar dilatational free strain. According to Coussy [5] and Coussy and Monteiro [6], [7], in the case of a freezing water-infiltrated porous material, pore pressure is no longer uniform since the porous space is partly occupied by ice crystals and partly occupied by the liquid water, and thus (0) becomes:

$$\varepsilon_f = \frac{b_c p_c + b_l p_l - 3K\alpha\Delta T}{3K} \tag{0}$$

where subscript c refers to the ice crystal and subscript l refers to the liquid water, and:

$$b_c + b_l = b \tag{0}$$

Assuming that all pores subjected to the same pore pressure deform the same, we get:

$$b_j = S_j b \tag{0}$$

where S_j is the volume fraction of the pores occupied by species j such that:

$$\sum_j S_j = 1 \tag{0}$$

In order to calculate ε_f from (0), it is necessary to determine p_l and p_c. p_c can be determined in terms of p_l using equation (0). Assuming p_{atm} to be the gauge pressure, and substituting p_c from equation (0) into (0), we obtain:

$$\varepsilon_f = \frac{b_l p_l + b_c \frac{\rho_c}{\rho_l} p_l + \left(b_c \Sigma_m - 3K\alpha\right)\Delta T}{3K} \tag{0}$$

which for aggregates can be written as:

$$\varepsilon_f{}^a = \frac{b_l{}^a p_l{}^a + b_c{}^a \frac{\rho_c}{\rho_l} p_l{}^a + \left(b_c{}^a \Sigma_m - 3K^a\alpha^a\right)\Delta T}{3K^a} \tag{0}$$

and for matrix:

$$\varepsilon_f{}^p = \frac{b_l{}^p p_l{}^p + b_c{}^p \frac{\rho_c}{\rho_l} p_l{}^p + \left(b_c{}^p \Sigma_m - 3K^p\alpha^p\right)\Delta T}{3K^p} \tag{0}$$

Now, assuming that Darcy's law governs the liquid water flow, and substituting equation (0) and (0) in equations (0) and (0), respectively, liquid pressure in the aggregate and the matrix, as well as their corresponding strains, can be determined. This can be done by calculating the total mass of water, m_w (both liquid and crystal), currently contained in the porous material per unit initial volume. According to Coussy and Monteiro [7], m_w can be given as:

$$m_w = \rho_l \phi_o + \rho_l \left(\vartheta_{\Delta p} + \vartheta_{\varphi}\right) \tag{0}$$

where ϕ_o is the initial porosity of the porous material, while:

$$\vartheta_{\Delta\rho} = \left(\frac{\rho_c}{\rho_l} - 1 \right) \phi_o S_c \tag{0}$$

and

$$\vartheta_{\varphi} = b\varepsilon_{kk} + \frac{p_l}{M_l} + \frac{p_c}{M_c} + 3\left(\phi_o S_l \alpha_l + \phi_o S_c \alpha_c + a_l + a_c \right) \Delta T \tag{0}$$

where

$$\frac{1}{M_j} = \frac{b_j - \phi_o S_j}{K_s} + \frac{\phi_o S_j}{K_j} \tag{0}$$

$$\frac{1}{M} = \frac{1}{M_c} + \frac{1}{M_l} \tag{0}$$

$$a_j = \alpha\left(b_j - \phi_o S_j \right) \tag{0}$$

Here, a_j is the coefficient related to the thermal volumetric dilation of the pore volume occupied by the species j. M_j is the Biot's modulus of the species j. Using the mass balance equation along with Darcy's law, we can write:

$$\frac{1}{\rho_l} \frac{dm_w}{dt} = \frac{d\left(\vartheta_{\Delta\rho} + \vartheta_{\varphi} \right)}{dt} = \frac{k}{\eta_l} \nabla^2 p_l = \frac{k}{\eta_l} \frac{1}{r^2} \frac{d}{dr} \left(r^2 \frac{d}{dr} p_l \right) \tag{0}$$

where k is the intrinsic permeability with dimensions of length squared, and η_l is the viscosity of the pore fluid.

Equation (44) should be solved for p_l for both the aggregate and matrix. In order to solve for p_l^a and p_l^p, the following initial and boundary conditions are applied:

- Initially, the pore pressure is uniform and equal to atmospheric pressure, so:

  $$\left(p_l^p \right)_{t=0} = p_{atm} \tag{0}$$

- Thereafter, the surface can be subjected to arbitrary applied pressure p_{app}; in this case $p_{app} = p_{atm}$; hence:

  $$\left(p_l^p \right)_{r=R_o} = p_{atm} \tag{0}$$

- At the aggregate-matrix interface, continuity of the pressure requires the liquid pressure in the aggregate, p_l^a, and that in the matrix, p_l^p, to be the same:

  $$\left(p_l^a \right)_{r=R_i} = \left(p_l^p \right)_{r=R_i} \tag{0}$$

Based on the mass conservation, the liquid flow into the matrix must equal the heat flow out of the aggregate (and vice versa). Therefore:

$$k^a \left(\frac{dp_l{}^a}{dr} \right)_{r=R_i} = k^p \left(\frac{dp_l{}^p}{dr} \right)_{r=R_i} \tag{0}$$

- Due to the radial symmetry, no flow condition occurs in the center, which gives:

$$\left(\frac{dp_l{}^a}{dr} \right)_{r=0} = 0 \tag{0}$$

The solution can be readily obtained by use of the Laplace transform, as shown in the Appendix. The pore pressure, stress, and strain results obtained in the Laplace transformed domain is then inverted numerically into the time domain with the Stehfest Algorithm [21] using the script from [22] in Mathematica.

3 PREDICTING DAMAGE: NUMERICAL EVALUATION

To implement the proposed model, and to estimate pore pressure and the resulting deformation of the concrete under freezing condition, a coarse aggregate core of 0.051 m (2 inches) ($R_i =$ 0.0254 m) is considered to be embedded in the matrix shell, as proposed in Section 2.1. The body is assumed to be completely saturated and surrounded by free water. Temperature is decreased instantaneously to -25 °C in a single step. This results in uniform change of temperature throughout the body. Diameter of the outer radius, R_o, of the matrix shell is calculated from the dry-rodded coarse aggregate volume fraction, which depends on the maximum coarse aggregate size and fineness moduli of sands. For example, for a 2 inch maximum coarse aggregate size, the dry-rodded coarse aggregate volume per unit volume of concrete may vary from 72% to 78% for different fineness moduli of sands if the concrete mixture is designed according to American Concrete Institute (ACI) procedures [23]. Therefore, if a fineness modulus of 2.7 is assumed, the volume fraction of the dry-rodded coarse aggregate is 75%, and the outer diameter of the concrete sphere is found to be 2.2 inches (outer radius, R_o, of the sphere is 0.028 m). In addition, typical values consistent with concrete are adopted for both the aggregate core and matrix shell, such that $\phi_o^a = \phi_o^p = 0.2$, $k^a = k^p = 1\times10^{-21}\ \mathrm{m}^2$, $K_s^a = K_s^p = 45\times10^3\ \mathrm{MPa}$, $\alpha^a = \alpha^p = 10\times10^{-6}\ {}^\circ\mathrm{C}^{-1}$, and $v^a = v^p = 0.2$. This is done to verify the proposed model for a very simple structure with uniform properties. In the following section, multiple cases are examined, and these properties are changed to see how they affect concrete freeze-thaw response, especially the tensile stresses that may cause cracking to initiate. Bulk modulus of the porous body, *K*, is then determined in terms of K_s and ϕ_o [24], [25] according to:

$$K = (1-\phi_0)^2 K_s \tag{0}$$

Furthermore, we let $K_l = 1.79\times10^3$ MPa and $\alpha_l = -98.77\times10^{-6}\ \mathrm{K}^{-1}$ at 263 K for supercooled water, and $K_c = 7.81\times10^3$ MPa and $\alpha_c = 51.67\times10^{-6}\ \mathrm{K}^{-1}$ at 263 K for ice crystal [5]. Liquid density, ρ_l, and crystal density, ρ_c, are assumed to be 999.8 kg m^{-3} and 916.7 kg m^{-3} at 273 K, respectively [5]. Additionally, Σ_m is considered to be 1.2 MPa K^{-1} [5], and liquid degree of saturation, S_l, is derived using the same approach depicted by Coussy [5]:

$$S_l = \left[1 + \left(\frac{1}{\Im} \left(\Delta T - \frac{1}{\Sigma_m} \left(1 - \frac{\rho_c}{\rho_l} \right) p_l \right) \right)^{\frac{1}{1-m}} \right]^{-m} \quad (0)$$

where m is the shape factor relating the pore size distribution, and $0 < m < 1$. The closer m is to 1, the more narrow banded the pore radius distribution is. $\Im$ is a characteristic cooling related to both the porous material geometry and the interface properties and can be determined in terms of capillary modulus, $\aleph$ [5], using the following relationship:

$\Im = 0.4734 \times \aleph$

where $\aleph$ ranges from a few MPa for rocks up to about 35 MPa for cement pastes [3]. The term associated with p_l in (0) is neglected, and the reason behind this assumption is twofold. First, temperature change is assumed to be so fast compared to the pore liquid flow timescale that S_l can be assumed to be primarily dependent on temperature rather than pore pressure. Second, dependence of saturation on pore pressure makes (0) highly complicated even in the Laplace transformed domain, and in that case (0), the Laplace transformed domain needs to be solved numerically. Thus, determination of pore pressure becomes much simplified, and it is possible to obtain an analytical solution in the Laplace transformed domain if the pore pressure term in (0) is eliminated. However, this assumption is only valid when low pore pressure (≈80 MPa) is generated. S_c is then calculated from the constraint:

$$S_c = 1 - S_l \quad (0)$$

In the present case, it is assumed that the outer boundary of the concrete sphere is surrounded by free water at all times, and it is in equilibrium with the atmospheric pressure. This might not be the case when the pavement is surrounded by pure water, which freezes instantly when the temperature is reduced below the melting point. However, continuous traffic movement and presence of dissolved salt may prevent complete freezing of the liquid water. Instant cooling of the concrete sphere to -25 ºC results in uniform freezing of liquid water in the entire pore network. As a result, positive pressure builds up, caused by the volume increase associated with the ice formation and the resulting pore volume change. At the very beginning, pore liquid pressure is the same everywhere. However, this pressure relaxes immediately to atmospheric pressure and attains equilibrium at the outer boundary of the sphere as the excess water is expelled instantly to the surrounding free water body. However, high positive pressure at the center cannot dissipate at once because of the high distance that the excess water must travel to the boundary to relax it. Moreover, the relaxation time can be on the order of hours for a material with a very low permeability. Hence, a pressure gradient is generated in the liquid from the peak positive pressure at the center to the atmospheric pressure at the outer surface. This is shown in Figure 5. As temperature is held constant, the excess water from inside the body is expelled to the outer periphery to relieve the gradient, and the pressure equilibrates everywhere. It is also seen that as the distance the water has to travel to equilibrate the positive pressure becomes higher toward the center, more time is required to relax the pressure.

As Figure 5(b) illustrates, as pore pressure dissipates from the outer layer, the outer part of the sphere contracts. Consequently, due to the strain compatibity requirement, a sudden pressure jump, namely the Mandel-Cryer effect [20] occurs in the inner part right before the pressure starts to dissipate. Accordingly, that interior layer starts to shrink (Figure 6), but the center does not shrink that much, and increasing tensile tangential stress (Figure 7) is developed at that interior layer. As more time passes and water starts to dissipate from the interior, this Mandel-Cryer effect shifts toward the center, creating over-pressurization. The tangential stress thus transfers toward the center with time, as shown in Figure 7.

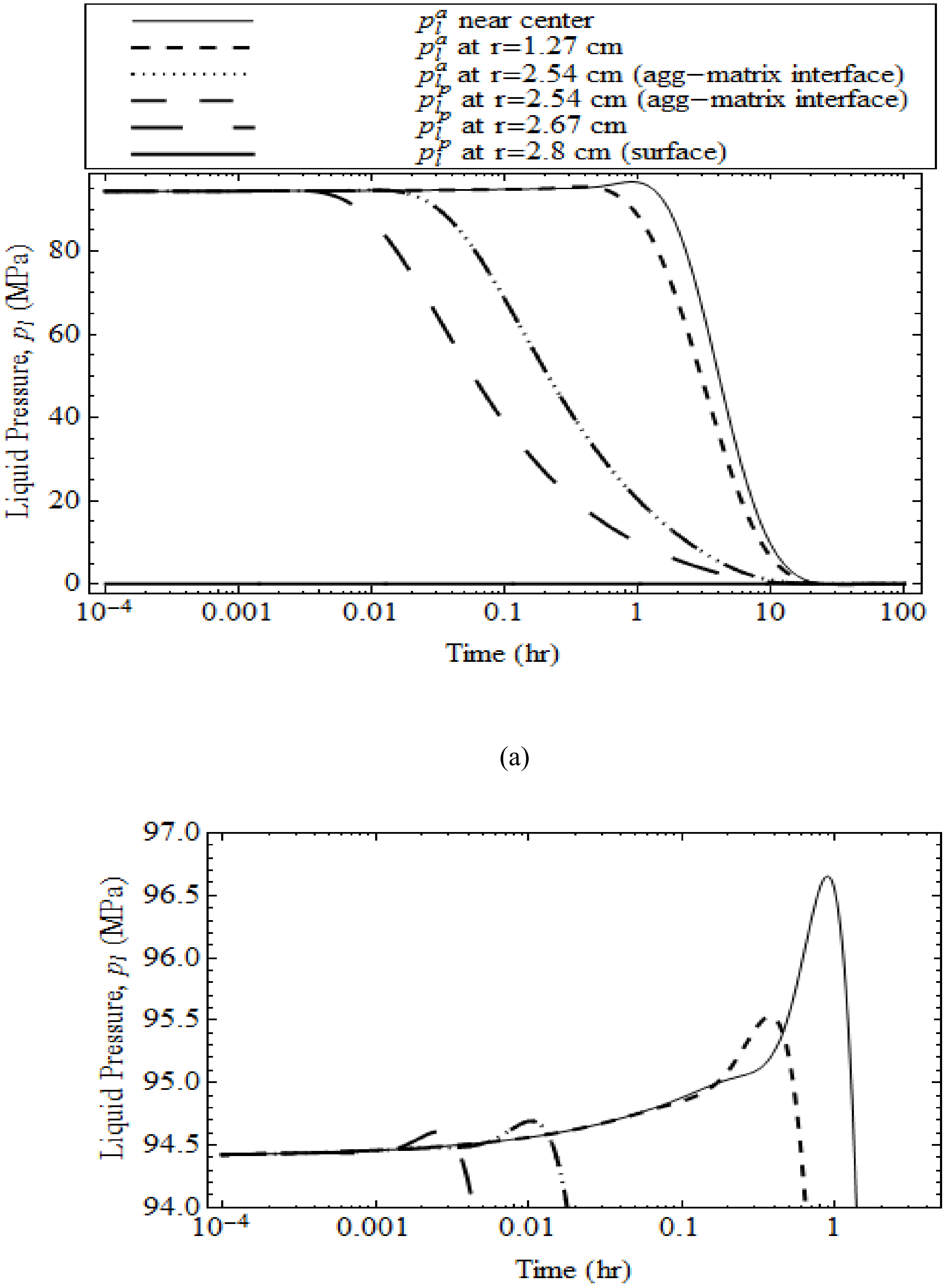

(a)

(b)

Figure 5. (a) Pressure gradient in the concrete sphere. The peak hydraulic pressure at the center takes the longest time to equilibrate with the atmospheric pressure at the boundary. (b) As water starts to dissipate from the interior, the Mandel-Cryer effect shifts toward the center.

When the temperature drops, various deformations occur for different species (solid skeleton, ice, and water) and affect the dimensional change of the body. Water shows highly complex and anomalous behavior due to its intra-molecular hydrogen bonding [26]. Unlike other liquids, water has a nonlinear CTE, which reduces increasingly at low temperatures and becomes negative below 0 °C [26]. As a result, when water freezes at 0 °C, its volume increases by about 9% under atmospheric pressure. Moreover, under freezing temperatures, the unfrozen water expands, whereas the frozen ice contracts. The deformation that will dominate over the other is dictated by the physical and poromechanical properties of both the aggregate and matrix. Initially, as shown in Figure 6, contraction caused by the cryo-suction process is offset by the dilation resulting from the hydraulic pressure and the thermal deformation, and a uniform expansion is observed. However, initial dilation of the outermost fiber of the matrix shell is negligible due to the immediate equilibration of the pore pressure. As a result, strain differential develops throughout the concrete sphere. With time, this dilation and strain differential disappear as the pore liquid pressure decays to the atmospheric pressure to reach equilibrium, resulting in a net contraction contributed by the thermal deformation and the cryo-suction process.

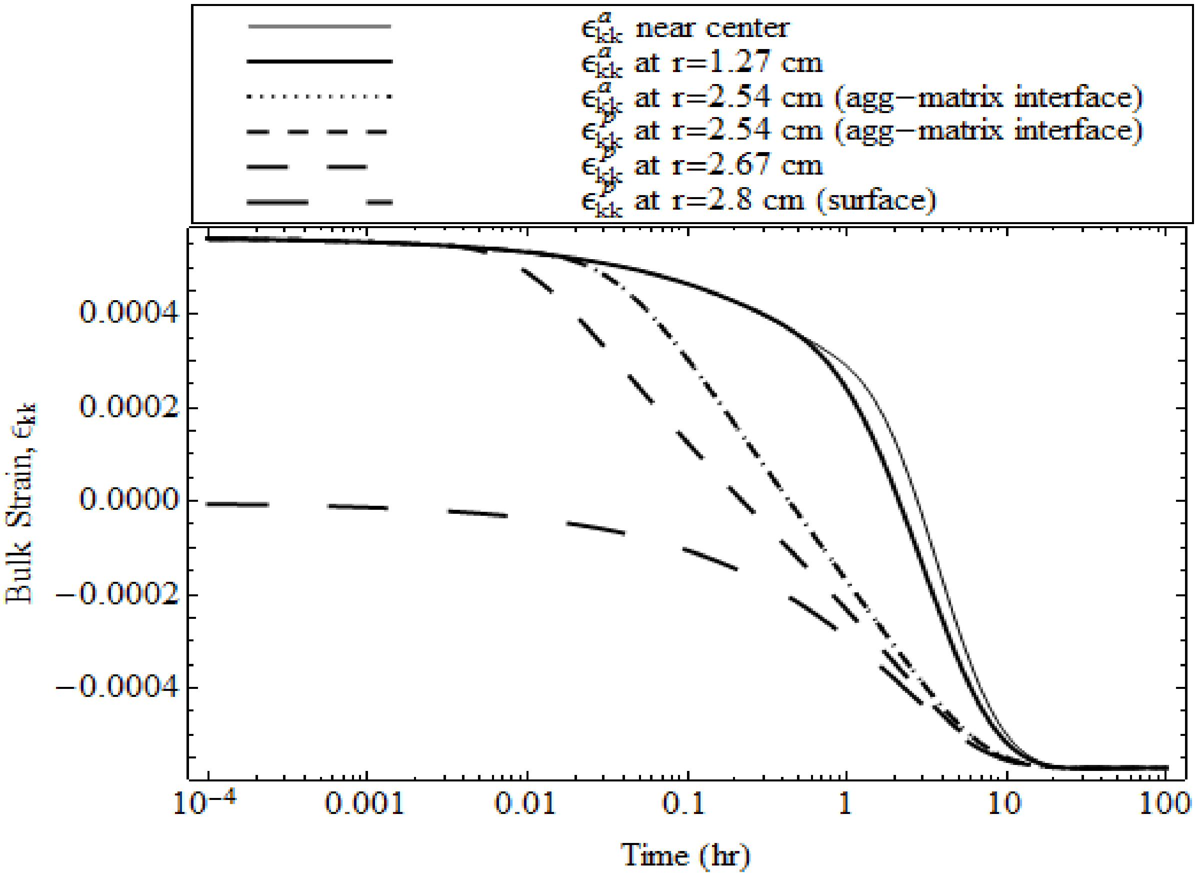

Figure 6. Bulk strain distribution created by the pore pressure gradient in the concrete sphere. Uniform contraction is achieved once pore pressure dissipates to reach equilibrium.

Figure 7 provides the tangential stress distribution caused by the combined action of the crystallization and the hydraulic pressure. As water solidifies to ice, the crystal sustains a water film between the pore wall and the crystal, allowing it to grow and push the wall away. The pressure that ice generates this way creates tensile stress [14]. Moreover, pore pressure gradient (Figure 5) created by the density difference between the ice and water results in strain differential (Figure 6), which in turn generates tangential stress gradient in the body. This is because the center has the peak positive pressure and dilates more than the boundary. However, the boundary, which is at equilibrium with the atmospheric pressure, does not allow it to dilate and thus puts it under compression. Similarly, higher dilation at the center than the boundary exerts tensile stress at the surface. However, with time, as the matrix shell starts to contract more than the aggregate core due to the pore water dissipation, over-pressurization occurs at the center, induced by the Mandel-Cryer effect [20]. This in turn results in high tensile stress at the aggregate boundary and high compressive stress at the center. The stress gradient eventually dissipates as the pore pressure relaxes and the strain becomes uniform. An initial peak stress of about 24.5 MPa is developed at the outermost fiber of the matrix by the instantaneous cooling of the material to -25 ºC, which is unlikely to occur in the practical field. In real life, cooling rate is much slower than the rate assumed here and is incapable of developing this high stress. This is further discussed in detail in Section 4.1.1. However, at time t = 2 hours, by when a significant amount of pore water pressure is dissipated, the stresses in the sphere are still high enough to initiate cracks. Thus, successive cycles of freezing and thawing have potential to create cracks, as the tensile stresses may exceed the matrix or aggregate tensile strength under freezing temperatures. Once again, it is to be noted that for this particular example, tensile stress can be developed in the sphere even though there is no distinction between aggregate core and matrix shell constituent properties. This implies that crack initiating stress in this case is generated by the strain differential and pressure gradient. The Mandel-Cryer effect further exacerbates this tensile stress and reduces concrete durability.

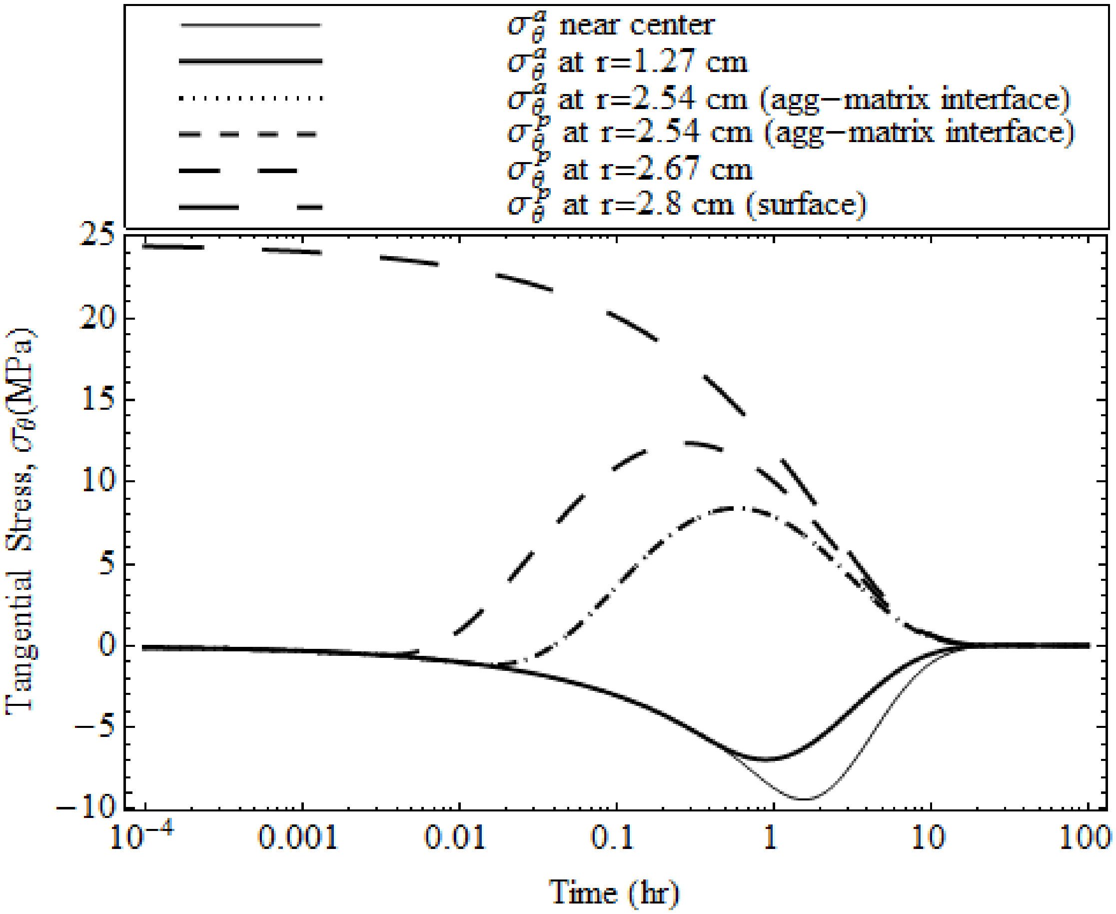

Figure 7. Tangential stress distribution, caused by the hydraulic pressure gradient and strain differential.

4 SENSITIVITY

When concrete is exposed to repeated cycles of freezing and thawing, D-cracking can occur if the concrete contains a sufficient quantity of aggregate particles that are susceptible to D-cracking. Severity of the damage can be attributed to various material properties such as aggregate size, pore size distribution, aggregate and matrix permeability, thermal properties (e.g., CTE of ice, water, aggregates, and matrix), and aggregate and matrix bulk modulus. In addition, air entrainment and cooling rate play key roles in determining concrete durability. This section presents the sensitivity of the damage propensity to these various factors. The section is divided into four subsections: the first two include effects of aggregate and matrix properties on the extent of the damage development, and the third and fourth subsections describe the effect of the air entrainment and cooling rate, respectively. For each sensitivity analysis, only the parameters being discussed are varied, keeping the others the same as assumed in Section 1. Also, to predict field results, typical material property values found in the existing literature are used.

4.1 Effect of the Aggregate Properties

Concrete subjected to freezing and thawing usually suffers D-cracking when pore pressure is generated in a critically saturated, nondurable aggregate and the resulting tensile stress exceeds the tensile strength of the aggregate. This in turn causes cracking of the aggregate particle and the surrounding matrix and creates additional channels for the migration of moisture in the aggregate particles. The newly formed cracks then become potential sites for the formation of ice during the next freeze-thaw cycle [10]. Numerous studies have been performed to investigate the role of aggregate properties on the concrete resistance to freeze-thaw and D-cracking [10], [27–31]. Researchers found that the critical aggregate parameters influencing D-cracking are maximum particle size, permeability, porosity, and pore size distribution. The purpose of this section is to examine the influence of these properties on the damage growth propensity in concrete subjected to freeze-thaw cycles. Furthermore, the effect of thermal properties (CTE) of aggregates on concrete frost resistance is also investigated here.

4.1.1 Aggregate Pore Structure: Porosity, Permeability, and Pore Size Distribution

Various studies have already established that the pore characteristics of aggregate significantly influence the frost resistance of concrete [10], [27], [30]. Although the volume of pores in most natural aggregates is usually under 3% and rarely exceeds 10% [32], [33], the coefficient of permeability of marble, trap rock, diorite, basalt, and dense granite is generally of the order of 1 to $10\times10^{-21}\,\mathrm{m}^2$. Some varieties of granite, limestone, sandstone, and chert show values that are higher by two orders of magnitude [33]. For example, for limestone, intrinsic permeability is reported to be $1.7\times10^{-21}\,\mathrm{m}^2$ [34], and for sandstone, it can be as high as $1.28\times10^{-15}\,\mathrm{m}^2$ [33], [35]. The reason why some aggregates with only 10% porosity show much higher permeability is that the size of capillary pores in aggregates is usually much larger than 10 μm on average [33]. Some cherts and limestones contain considerable content of fine pores with low permeability, making them vulnerable to expansion and cracking associated with slow moisture movements and the resulting hydrostatic pressure [33]. Therefore, based on the previous studies on the aggregate response under freezing conditions, the following classes of aggregates are considered for analyzing the proposed model:

- High-porosity ($\phi_o^a = 0.1$), low-permeability ($k^a = 1.7\times10^{-21}\,\mathrm{m}^2$) aggregate with fine pore structure ($m^a = 0.5$).
- Low-porosity ($\phi_o^a = 0.003$), high-permeability ($k^a = 1.28\times10^{-15}\,\mathrm{m}^2$) aggregate with coarse pore structure ($m^a = 0.9$).
- High-porosity ($\phi_o^a = 0.1$), high-permeability ($k^a = 1.28\times10^{-15}\,\mathrm{m}^2$) aggregate with intermediate pore structure ($m^a = 0.7$).
- Low-porosity ($\phi_o^a = 0.003$), low-permeability ($k^a = 1.7\times10^{-21}\,\mathrm{m}^2$) aggregate with fine pore structure ($m^a = 0.5$).

4.1.1.1 High-Porosity, Low-Permeability Aggregate with Fine Pore Structure

According to Verbeck and Landgren, high-porosity but low-permeability aggregates, typical of cherts with a fine pore structure, can cause failure because of high internal pressures built in the aggregates [27]. In the same study, they estimated that the pressure created at the beginning of freezing of the low-permeability chert should be approximately 100 times greater than for the high-permeability dolomite [27]. Later, Kaneuji established a correlation between pore size distribution of aggregates to the concrete freeze-thaw durability and reported that the pore size of aggregates affects the durability of concrete greatly in the diameter range of 10 μm to 0.1 μm, and the durability drastically decreases for aggregates with a pore size larger than 1 μm [36]. However, pores smaller than 45 Å do not affect the durability, probably because they are so small that the water needs a much lower temperature to freeze in them [36]. Also, Mehta and Monteiro associated D-cracking with the coarse aggregates that contain high pore volume in the narrow pore size range (0.1 to 1 μm) [33]. Therefore, a 0.051 m (2 inch) aggregate with high porosity, $\phi_o^a = 0.1$, low permeability, $k^a = 1.7 \times 10^{-21}\,\mathrm{m}^2$, and fine pore structure, $m^a = 0.5$, is analyzed here. The resulting plots are provided in Figure 8, Figure 9, and Figure 10.

As shown in Figure 8, a pore pressure of about 96 MPa is initially developed throughout the porous body. Because of the low permeability, a very tortuous path is created through which water has to travel to the boundary to relax this pressure. As a result, a relaxation time of about 7 hours is required for the complete dissipation of the pore pressure at the center of the aggregate, which may cause substantial damage to the concrete. In the beginning, as shown in Figure 9, the outer part of the matrix shell contracts due to the immediate relaxation of the pore pressure, whereas the interior part expands. Additionally, the matrix shell interior expands more than the aggregate core. This may be the consequence of the various thermal deformations that are occurring simultaneously in difference species: the solid skeleton and ice are contracting, while the unfrozen water is dilating. Since the pore volume in the aggregate ($\phi_o^a = 0.1$) is smaller than the pore volume fraction in the matrix ($\phi_o^p = 0.2$), and K_s is the same for both elements, bulk modulus of the porous body, *K*, and Biot's modulus, *M*, for the aggregate are bigger than for the matrix, whereas Biot's coefficient *b* is smaller for the aggregate than the matrix. As a combined effect of this, initially the aggregate expands less during cooling to -25 °C than the matrix interior and exhibits tensile stress, as illustrated in Figure 10. Consequently, the matrix interior undergoes compressive tangential stress at first. As the aggregate is assumed to contain a high volume of fine pores with low permeability, the tangential stress developed at the outermost fiber of the aggregate attains the peak value at around t = 0.25 hours due to the strain distribution imposed by the Mandel-Cryer effect. Furthermore, it is interesting to note that at the equilibrium, as the entire pore pressure relaxes to the atmospheric pressure, the aggregate shows higher contraction than the matrix and therefore experiences tensile stress. Hence, several cycles of freezing and thawing can eventually generate tensile stress exceeding the tensile strength of the aggregate and initiate cracks inside the aggregate. Thus, it is found that the high-porosity, low-permeability aggregate is susceptible to D-cracking, which is in accord with previous findings [27], [33].

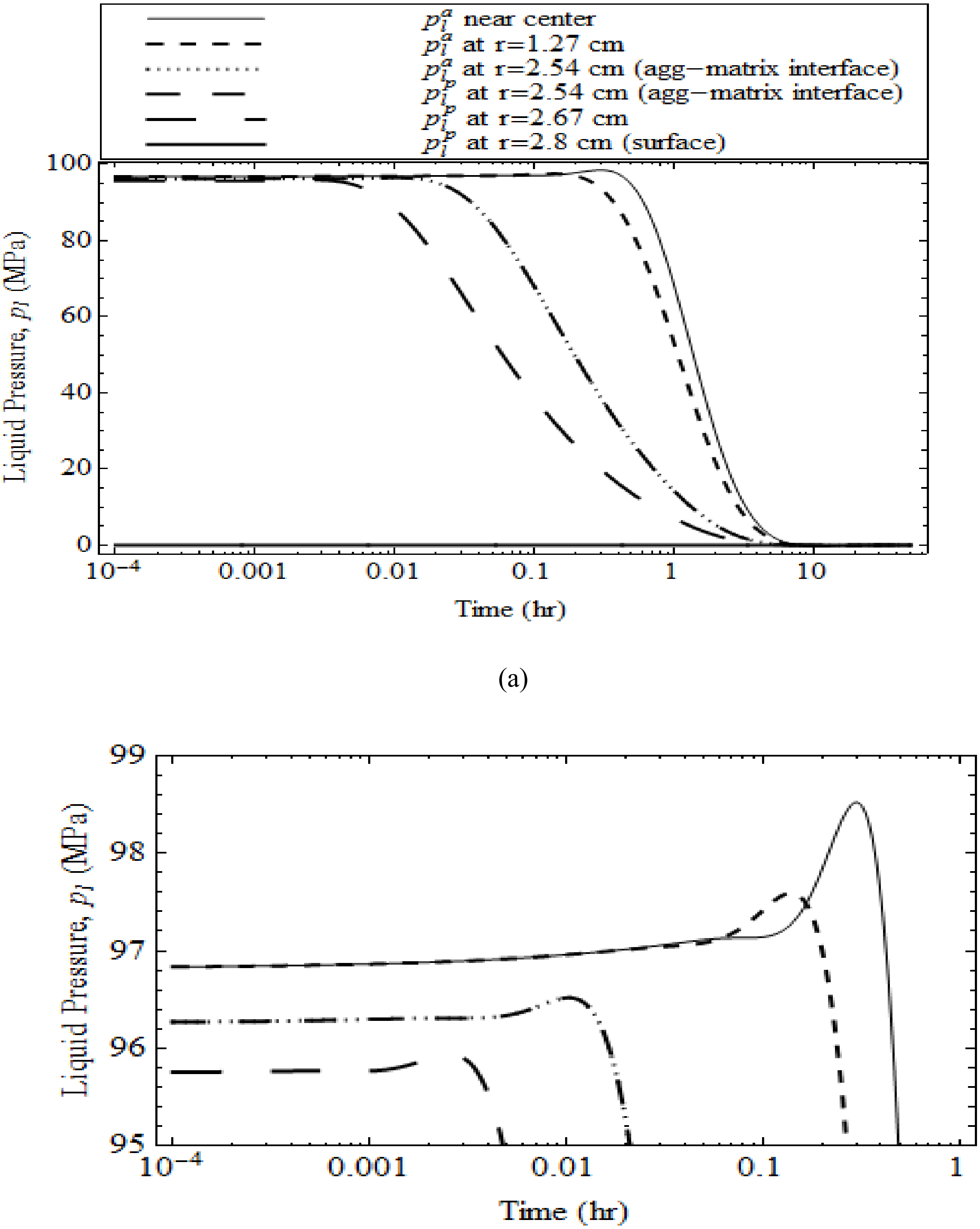

(a)

(b)

Figure 8. (a) Pore pressure distribution caused by the high-porosity ($\phi_o^a = 0.1$), low-permeability ($k^a = 1.7\times10^{-21}\,\mathrm{m}^2$), and fine-pore-structured ($m^a = 0.5$) aggregate. (b) Transfer of Mandel-Cryer effect toward the center delays the peak stress formation in the aggregate's outermost fiber (see Figure 10).

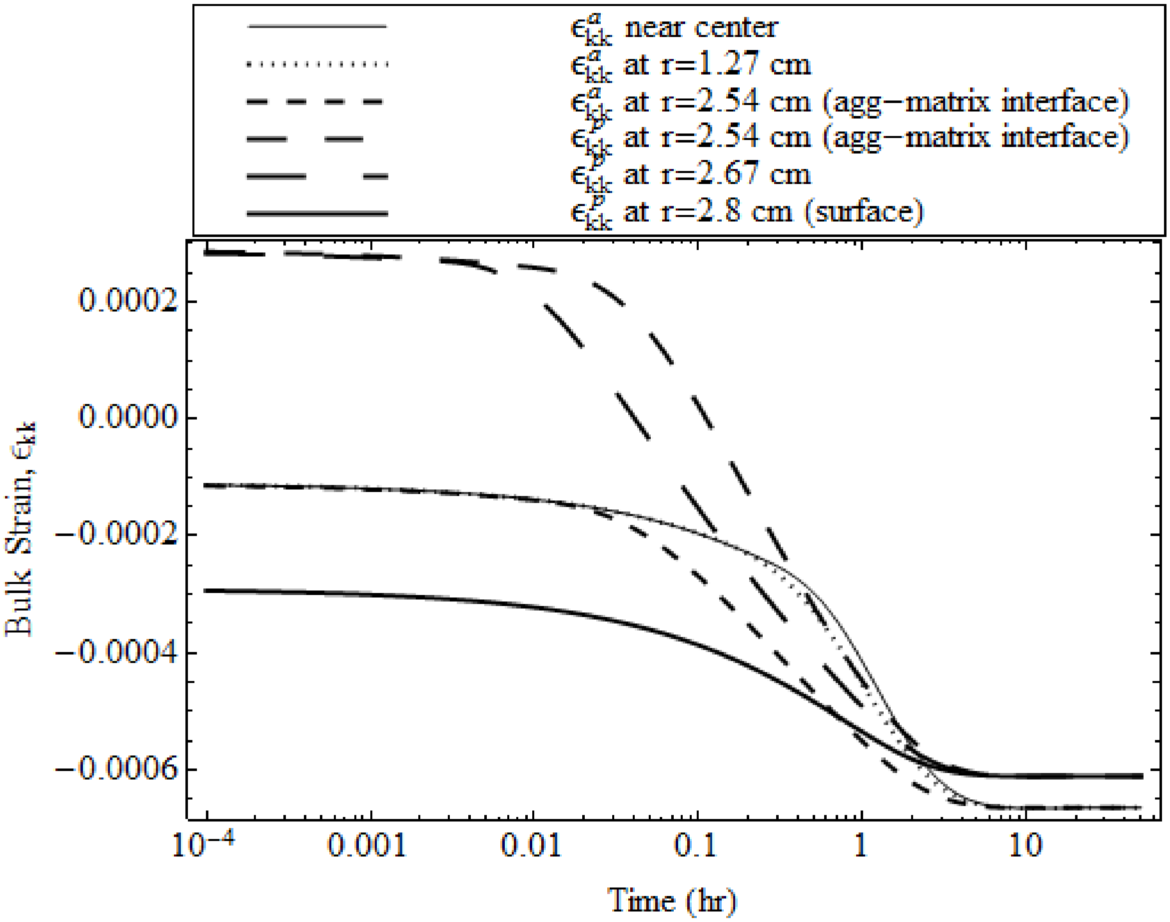

Figure 9. Strain differential caused by the high-porosity ($\phi_o^a = 0.1$), low-permeability ($k^a = 1.7\times10^{-21}\,\mathrm{m}^2$), and fine-pore-structured ($m^a = 0.5$) aggregate.

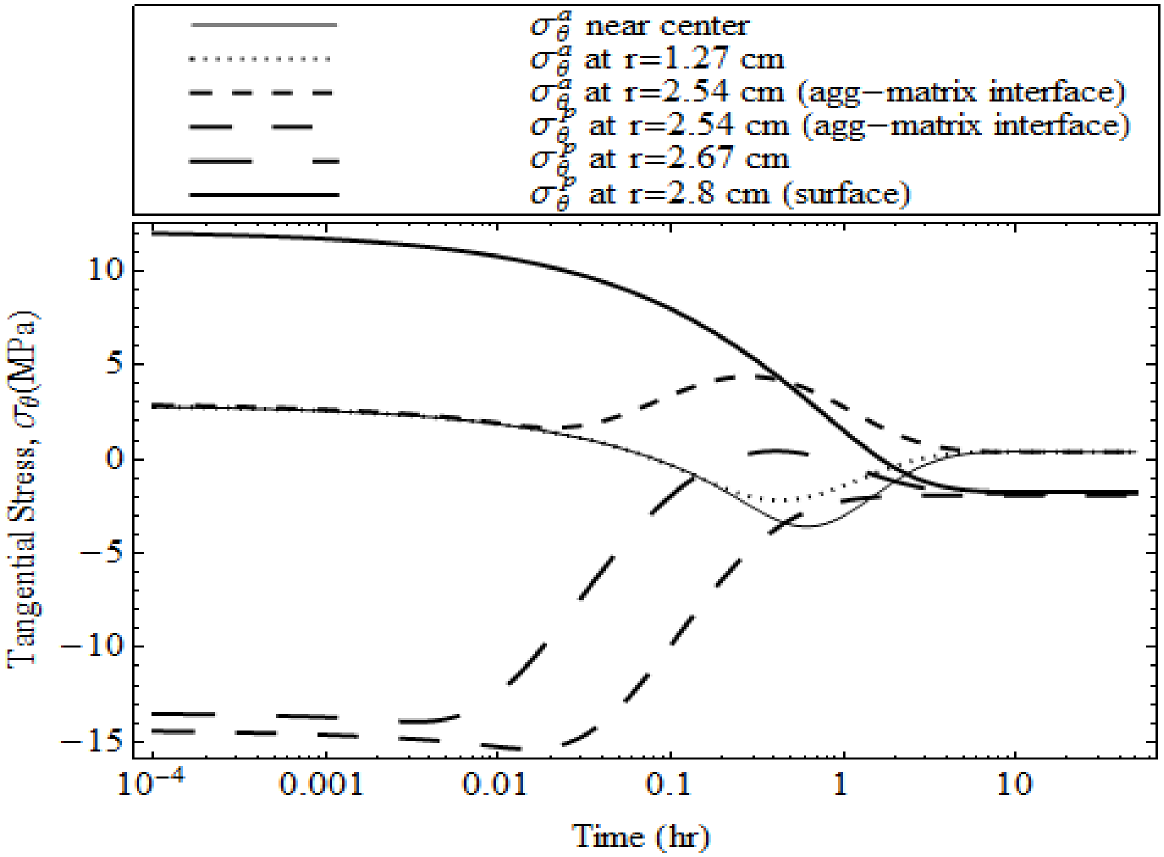

Figure 10. Delayed formation of the tensile stress (caused by the Mandel-Cryer effect and the associated shrinkage) at the outmost fiber of the high-porosity ($\phi_o^a = 0.1$), low-permeability ($k^a = 1.7 \times 10^{-21} \mathrm{m}^2$), and fine-pore-structured ($m^a = 0.5$) aggregate makes it vulnerable to D-cracking.

4.1.1.2 Low-Porosity, High-Permeability Aggregate with Coarse Pore Structure

Verbeck and Landgren also recognized that the low-porosity ($\phi_o^a = 0.003$), high-permeability aggregates with coarse pore structure can cause failure due to the high external pressure built up in the matrix [27]. Examples of such aggregates are quartzite sand marbles. In order to verify this phenomenon, the porosity is lowered from 0.1 to 0.003 with coarse pore structure ($m^a = 0.9$) and high permeability ($k^a = 1.28 \times 10^{-15} \mathrm{m}^2$). As shown in Figure 11, a high magnitude of initial pore liquid pressure of about 250 MPa is generated in the aggregate and in the interfacial transition zone (ITZ), which agrees with Verbeck and Landgren's study [27]. However, an initial uniform strain of -0.0006 in the aggregate generates a uniform tensile stress of about 3 MPa, while the matrix interior exhibits expansion and generates compressive stress of about -23 MPa in the ITZ. These results are shown in Figure 11, Figure 12, and Figure 13, respectively. As coarse pore structure with low pore volume fraction is assumed in the present example, about 98% of the pore volume is invaded by the ice at -25 ºC. Therefore, an initial dilation caused by the micro-cryo-suction process and mass density difference between the constituent species in the pore volume should have offset the thermal shrinkage [6]. Yet, the geometry and the equilibrium condition used in this model give rise to a complicated strain distribution where atmospheric pressure at the periphery causes the outermost fiber of the sphere to shrink (Figure 12). As a combined effect of all these deformations, a uniform initial strain of about -0.0006 is observed in the aggregate core, whereas a huge dilation of about 0.0011 is seen at the matrix fiber at the aggregate-matrix interface, which created a huge pressure of about 250 MPa in the aggregate. Additionally, magnitude of the tangential stress in the aggregate is relaxed substantially, as high permeability allows fast dissipation of the pore pressure (Figure 11), whereas the matrix shell exhibits wide distribution of pressure, stress, and strain because of the low permeability

($k^p = 1\times 10^{-21}\,\mathrm{m}^2$). Therefore, it is found that due to low porosity, the aggregate exhibits contraction and exerts compressive stress on the ITZ, and therefore no damage is expected in this layer, even though a very high pressure of 250 MPa is generated in the ITZ. Finally, for the reasons mentioned above, it can be concluded that although low-porosity, high-permeability aggregates create high pressure in the ITZ, they can seldom cause damage to the paste matrix unless a very big aggregate is used where the tensile stress takes hours to decay and create cracks within the aggregate.

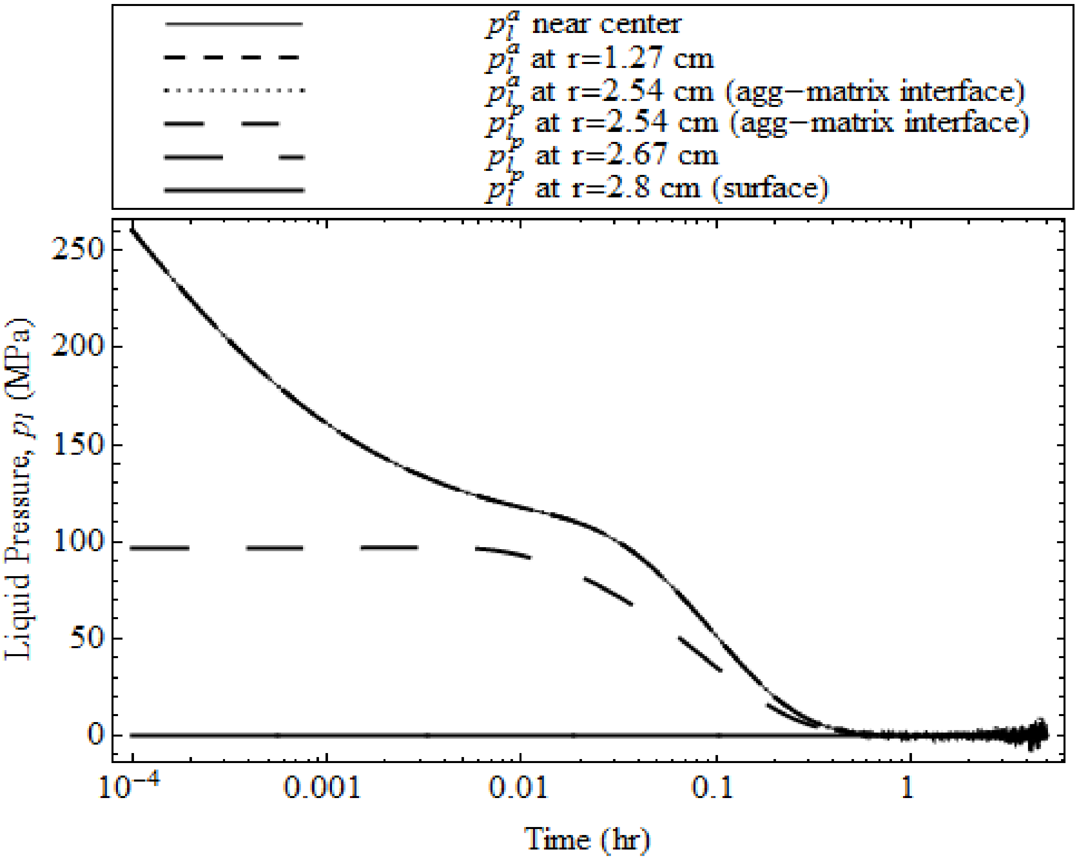

Figure 11. Pore pressure caused by the low-porosity ($\phi_o^a = 0.003$), high-permeability ($k^a = 1.28 \times 10^{-15}\,\mathrm{m}^2$), coarse-pore-structured ($m^a = 0.9$) aggregate.

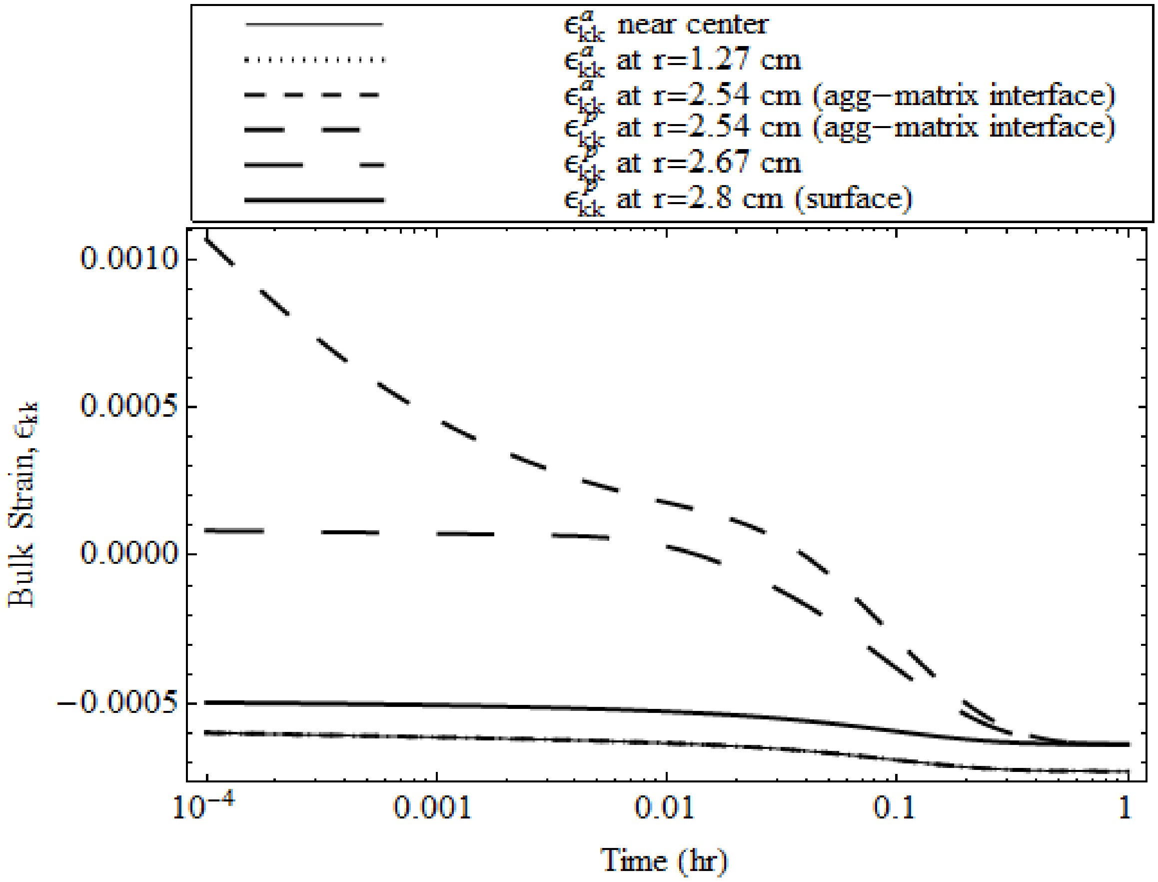

Figure 12. Strain differential generated in the concrete sphere caused by the low-porosity ($\phi_o^a = 0.003$), high-permeability ($k^a = 1.28\times10^{-15}\,\mathrm{m}^2$), coarse-pore-structured ($m^a = 0.9$) aggregate.

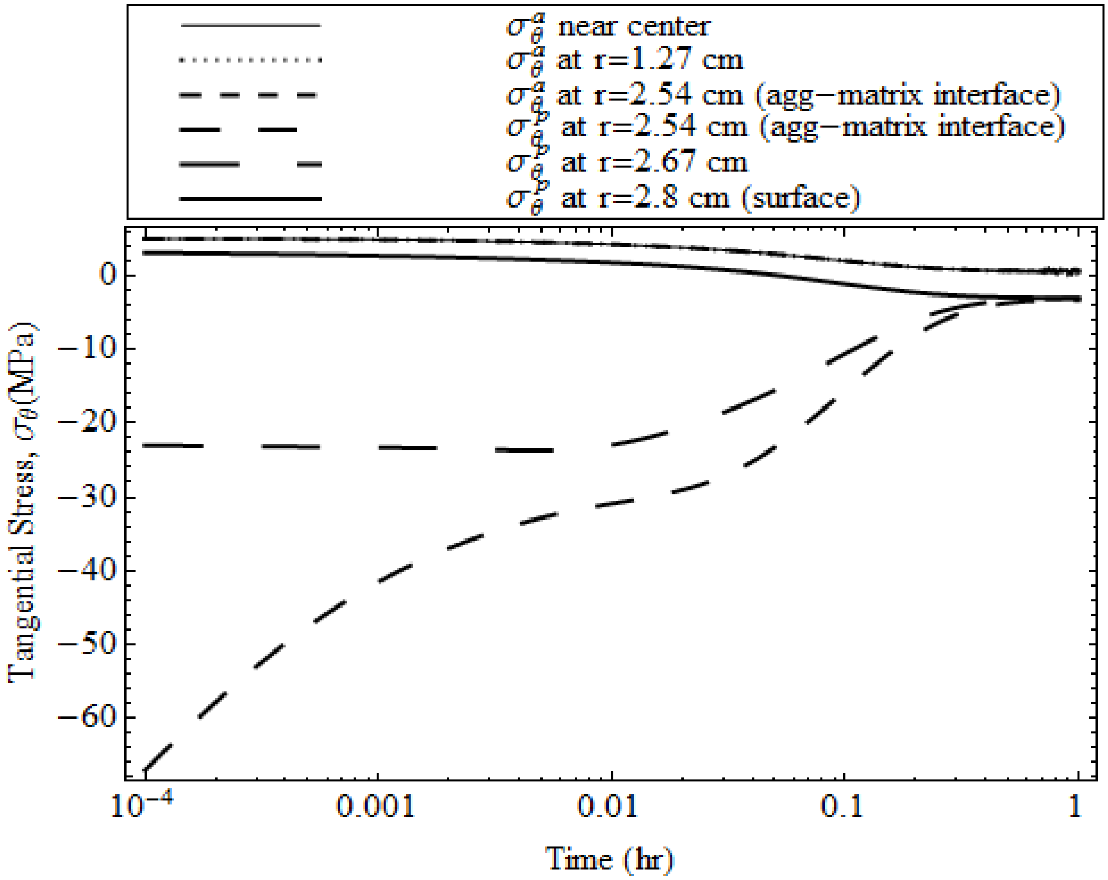

Figure 13. Stress gradient generated in the concrete sphere caused by the low-porosity ($\phi_o^a = 0.003$), high-permeability ($k^a = 1.28 \times 10^{-15}\,\mathrm{m}^2$), coarse-pore-structured ($m^a = 0.9$) aggregate.

4.1.1.3 High-Porosity, High-Permeability Aggregate with Intermediate Pore Structure

In this section, high-porosity but relatively high-permeability aggregates are considered, for which failure depends on the rate of temperature drop and the distance water must travel to find an escape boundary [27]. Typical examples of this type of aggregate are limestones, dolomites, and sandstones.

Figure 14, Figure 15, and Figure 16, respectively, show the pore pressure, tangential stress, and bulk strain generated in a concrete sphere made out of a high-porosity ($\phi_o^a = 0.1$), high-permeability ($k^a = 1.28 \times 10^{-15}\,\mathrm{m}^2$), fine-pore-structured ($m^a = 0.7$) aggregate. In Figure 14, it is seen that a uniform positive pore pressure of about 95 MPa is generated in the aggregate. The stress and strain distributions, as well as the relaxation time, are the same as found in the previous examples. However, a very low tangential stress of about 1 MPa is created in the aggregate, whereas a high initial stress of about 20 MPa is developed in the matrix, which dissipates to a negative value (compression) of 3 MPa as water flows to the escape boundary. Therefore, high-permeability, high-porosity aggregates reduce the potential to initiate cracks. It should be added here that high-porosity, high-permeability aggregates with open pore structure resemble lightweight aggregates, which proved beneficial under freeze-thaw cycles with improved durability [37], [38]. However, the bigger size of such aggregates may delay the relaxation and cause damage to the concrete by creating cracks in the matrix outermost boundary.

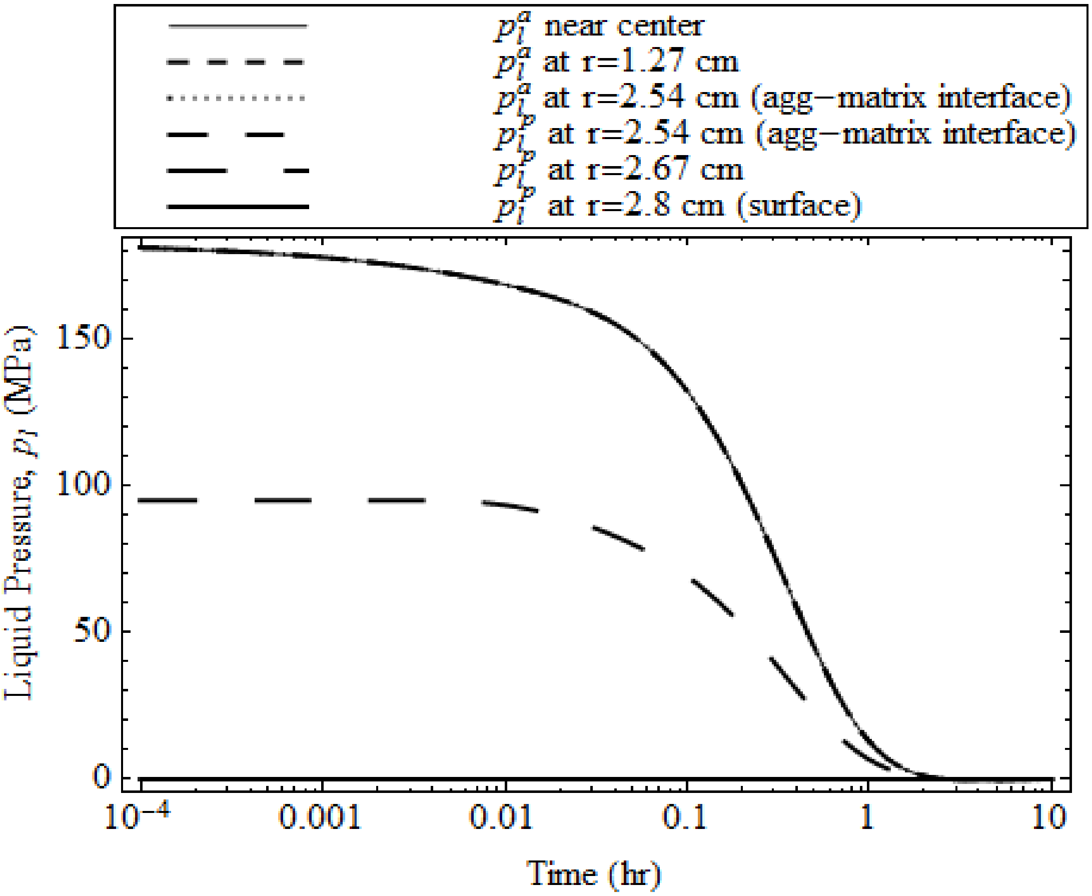

Figure 14. Pore pressure generated in the concrete sphere caused by the high-porosity ($\phi_o^a = 0.1$), high-permeability ($k^a = 1.28\times10^{-15}\,\mathrm{m}^2$), intermediate-pore-structured ($m^a = 0.7$) aggregate.

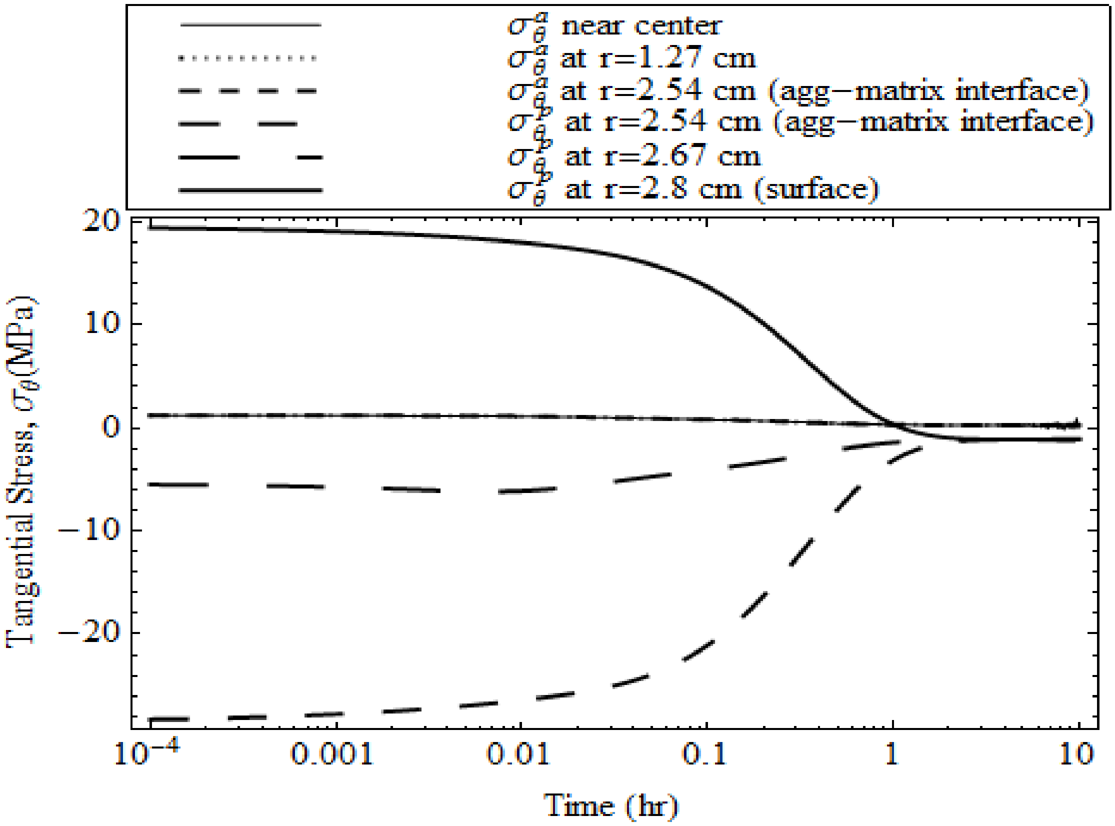

Figure 15. Stress gradient generated in the concrete sphere caused by high-porosity ($\phi_o^a = 0.1$), high-permeability ($k^a = 1.28 \times 10^{-15}\,\mathrm{m}^2$), intermediate-pore-structured ($m^a = 0.7$) aggregate.

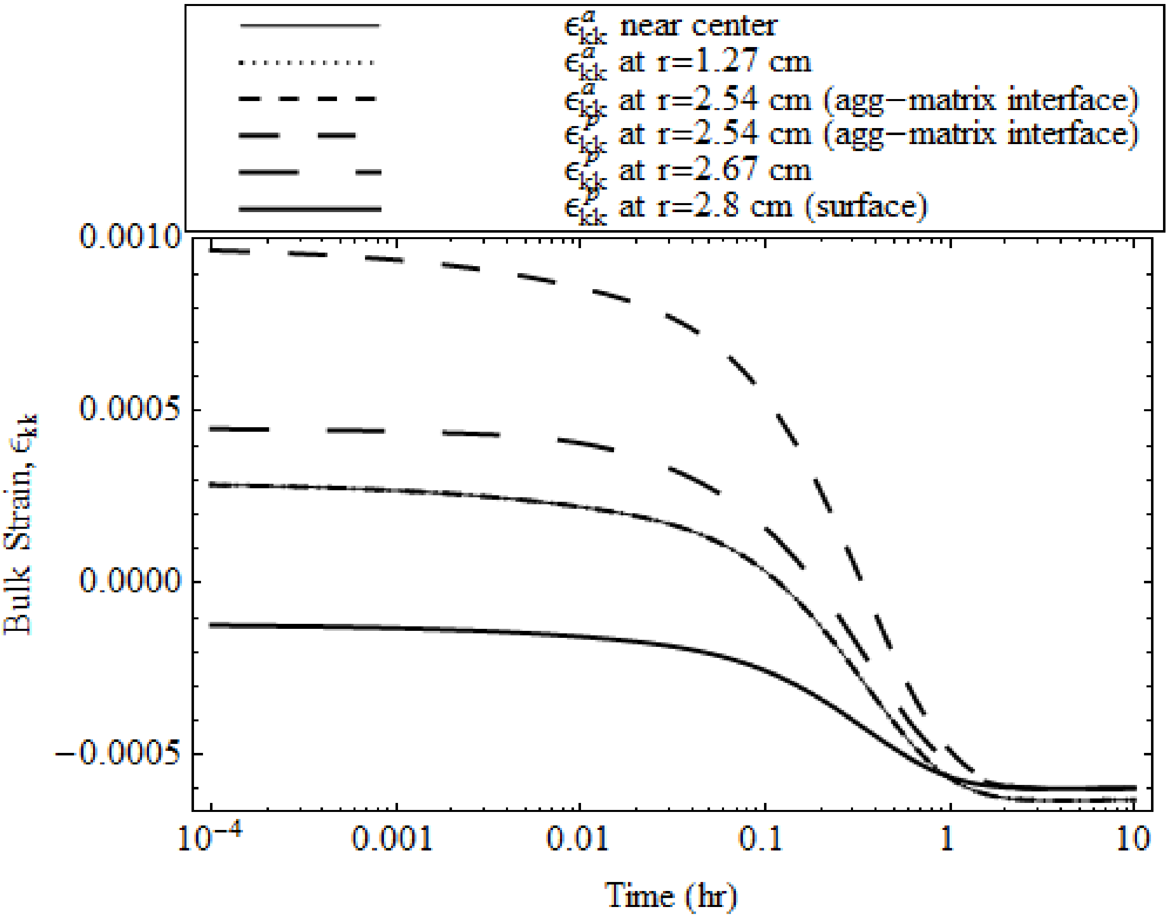

Figure 16. Strain differential generated in the concrete sphere caused by the high-porosity ($\phi^a_o = 0.1$), high-permeability ($k^a = 1.28\times10^{-15}\,\mathrm{m}^2$), intermediate-pore-structured ($m^a = 0.7$) aggregate.

4.1.1.4 Low-Porosity, Low-Permeability Aggregate with fine Pore Structure

As seen in Subsection 4.1.1.1 and 4.1.1.2, high-porosity, low-permeability aggregates are susceptible to creating delayed harmful stress caused by the Mandel-Cryer effect, whereas low-porosity, high-permeability aggregates are capable of producing high initial peak stress in both the aggregate and matrix outermost fiber. Therefore, in this section, aggregates with low porosity and low permeability with fine pore structure are assumed, and results are provided in Figure 17, Figure 18, and Figure 19. As shown in Figure 17, a peak pore pressure of about 98 MPa is developed in the aggregate center. However, as compared to the high-porosity, low-permeability aggregate (see Figure 8[b]), small pressure jumps occur in this case due to the Mandel-Cryer effect. Moreover, comparison of the results obtained in this section (Figure 18) to those in Subsections 4.1.1.1 and 4.1.1.2 shows that the low-porosity aggregate exhibits an initial contraction, whereas the high-porosity aggregate shows dilation at the very beginning. Therefore, the expansive matrix shell creates uniform tensile tangential stress in the aggregate, as shown in Figure 19.

In order to visualize the effect of aggregate properties on the damage propensity under freeze-thaw cycles, peak tensile stresses in the aggregate for the above four cases are plotted in Figure 20. It is found that the unique combination of high porosity, low permeability, and fine pore structure makes the aggregate most vulnerable to D-cracking due to the delayed stress formation, which is crucial for most freeze-thaw cycles that last longer than an hour, whereas the high initial peak stress developed for the low-porosity aggregate dissipates before it can create any damage to the aggregate. This peak stress is developed due to the instantaneous cooling of the material, which is unexpected in the practical field where cooling rate is reported to have a value of 0.8 to 0.9 ºC/hour [39]. Such low freezing rate is incapable of creating this high initial peak stress. This can be seen if the temperature is reduced to -25 ºC at a cooling rate of 5 ºC/hour instead of freezing the material instantaneously in a single step. Two types of aggregates are assumed in this case: one with high porosity and low permeability, and the other with low porosity, low permeability, and fine pore structure. The representative plots are shown in Figure 21, where the initial tensile tangential stress is the same for both types of materials. However, delayed peak tensile stress is developed in the high-porosity, low-permeability, fine-pore-structured aggregate, which takes several hours to relax, making concrete susceptible to D-cracking under freezing temperatures.

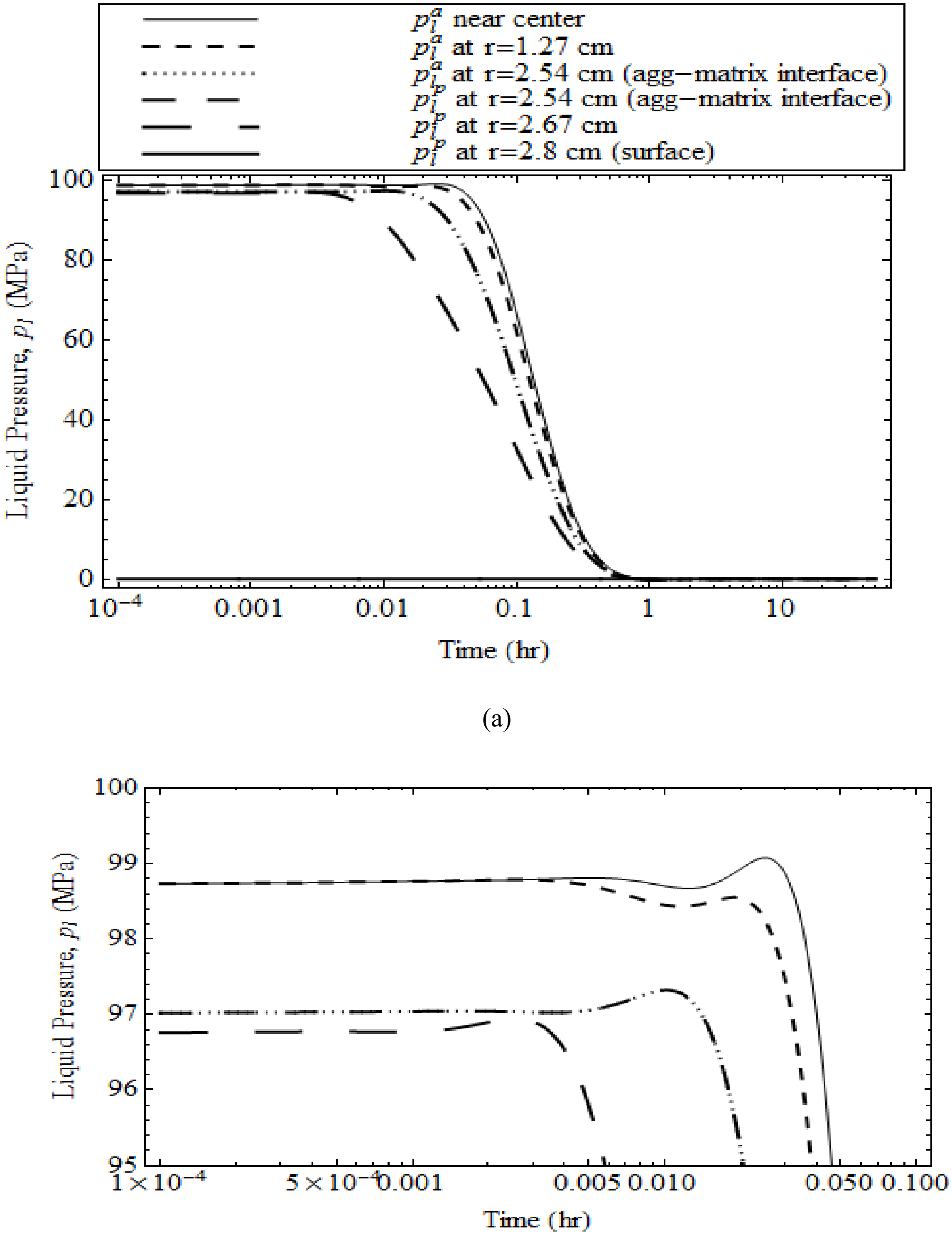

Figure 17. (a) Pore pressure developed due to the low-porosity, low-permeability aggregates with fine pore structure. (b) Relatively low Mandel-Cryer effect compared to high-porosity, low-permeability aggregate (Figure 8) is observed.

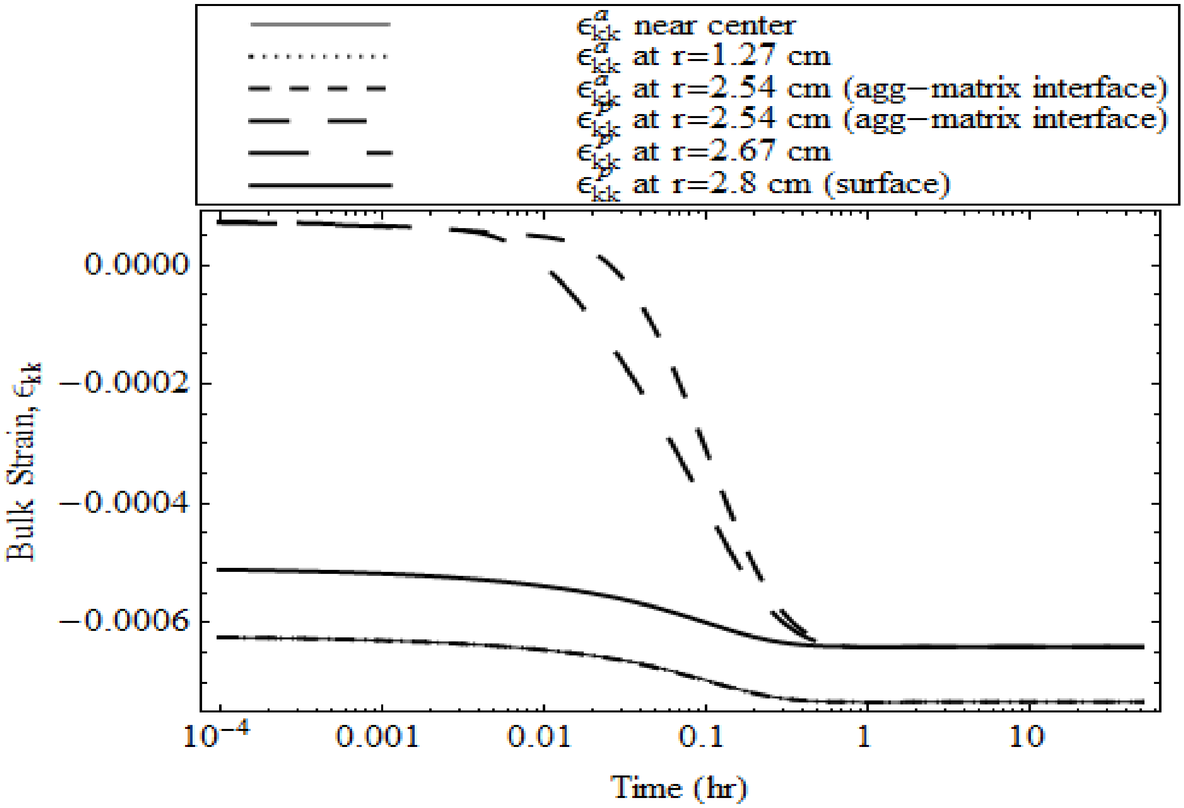

Figure 18. Unlike high-porosity, low-permeability aggregates (Section 4.1.1.1, Figure 11), low-porosity, low-permeability aggregates exhibit uniform contraction that creates high initial peak stress in the aggregate for a severe cooling condition.

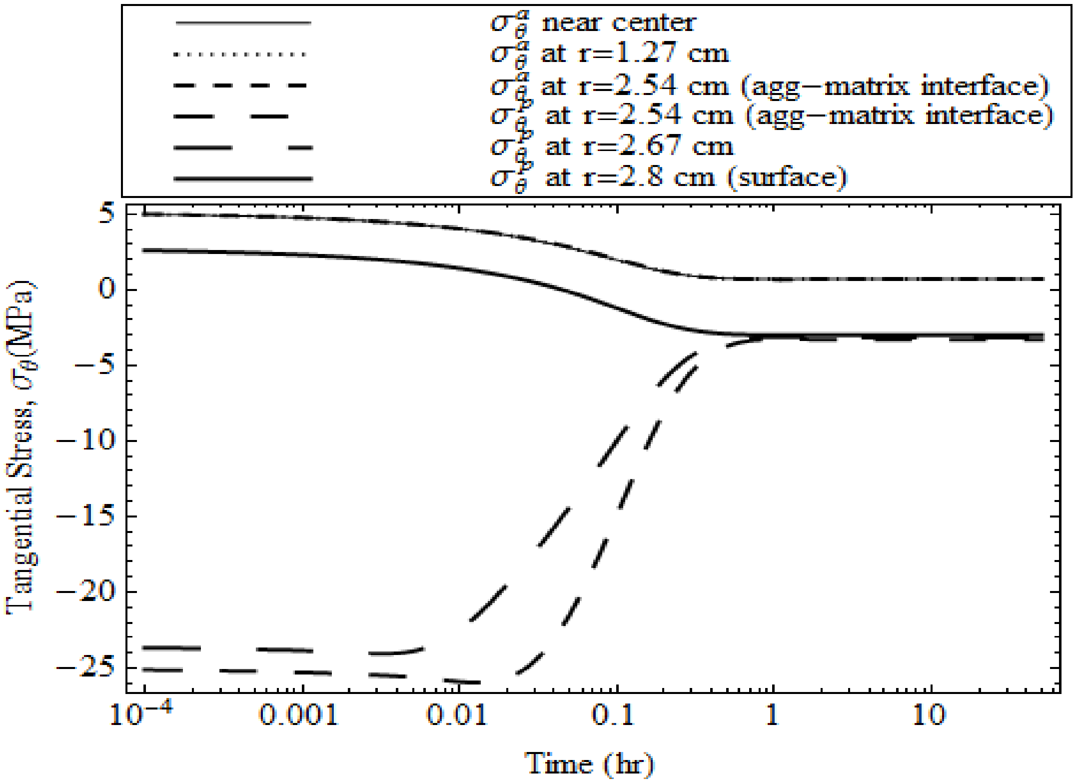

Figure 19. Tangential stress developed in the low-porosity, low-permeability aggregates with fine pore structure. The high initial peak stress in the aggregate that developed due to the instantaneous cooling of the sphere to -25 ºC dissipates within an hour without causing damage to the concrete.

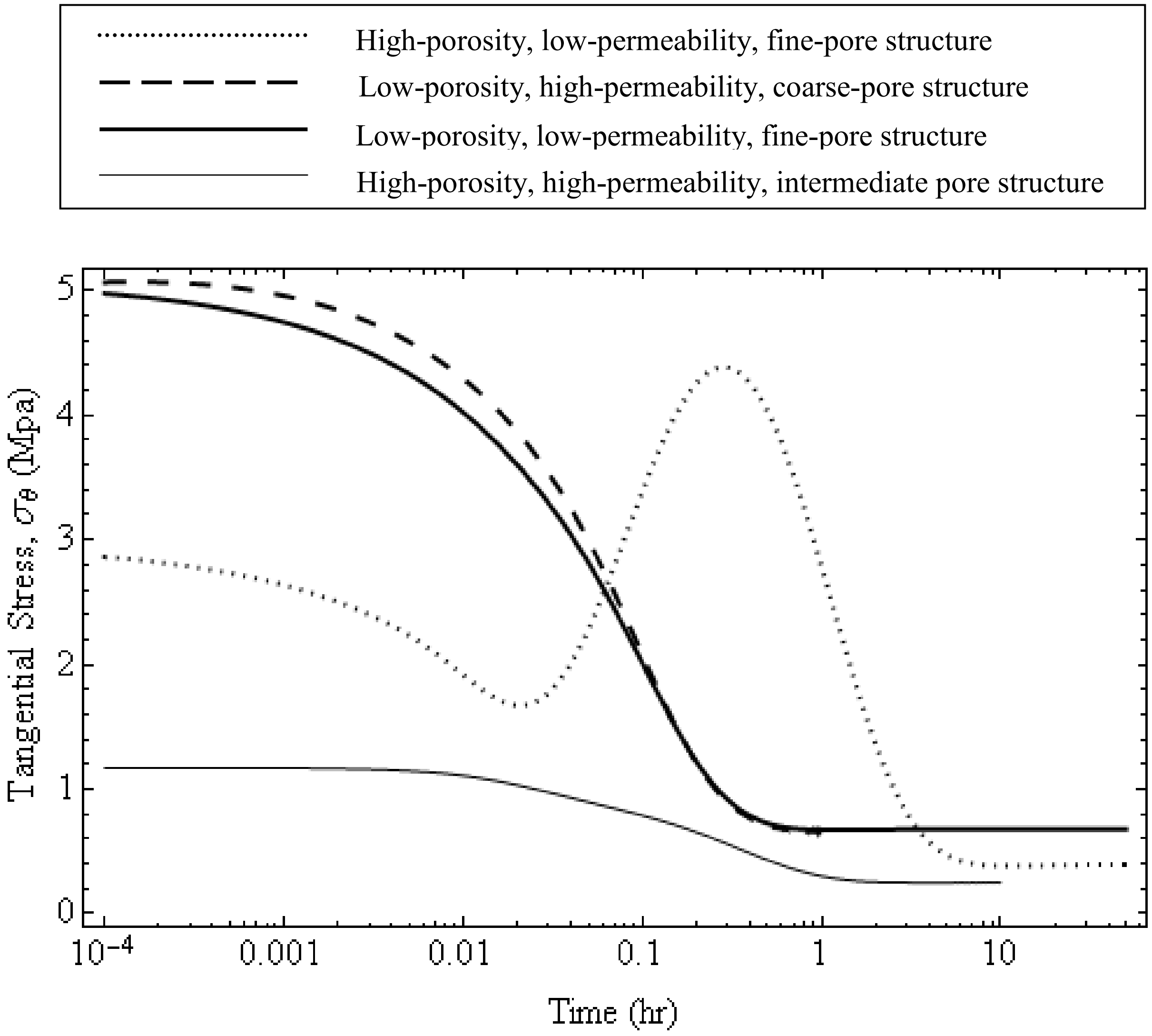

Figure 20. Effect of aggregate pore properties on the peak tangential stress generated in the aggregate fiber at the aggregate-matrix interface. Delayed development of the peak stress and slow relaxation make the high-porosity, low-permeability, fine-pore-structured aggregates most vulnerable to D-cracking, whereas high-porosity, high-permeability aggregates, for which the low stress is developed and quickly relaxed to the equilibrium value, are the least susceptible to D-cracking.

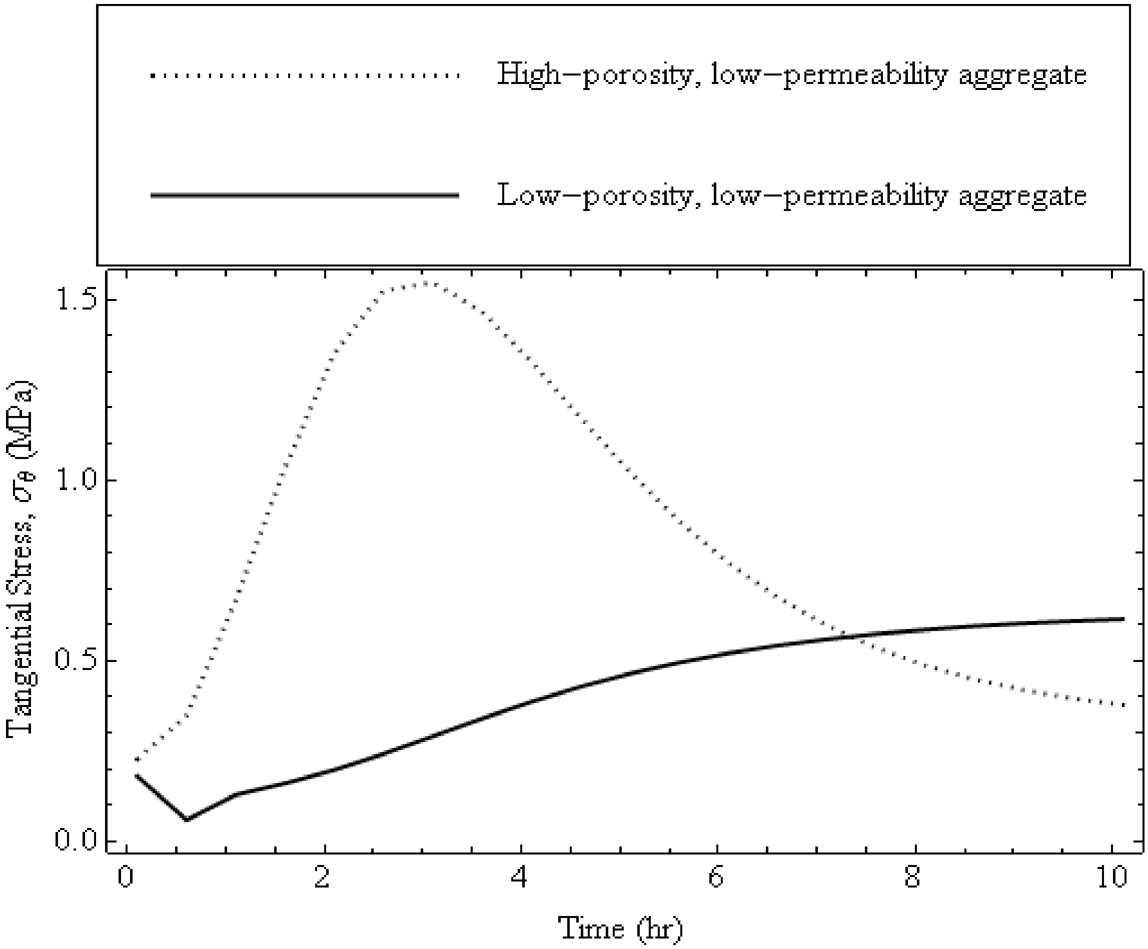

Figure 21. The initial peak tangential stress disappears as the cooling rate of 5 ºC/hour is used instead of the single-step cooling of 25 ºC. Hence, it is evident that high-porosity, low-permeability, fine-pore-structured aggregates are the most susceptible to D-cracking.

4.1.2 Aggregate Size

Several studies have recommended that reducing the maximum size of D-cracking susceptible aggregate particles improves the freeze-thaw durability of concrete and slows down the rate of development of D-cracking [10], [28–30]. Verbeck and Landgren argued that the pressure required to expel excess water from the frozen particles increases with the maximum aggregate size, as the distance that the water must travel through the pores also increases [30]. They claimed that a 1.3 cm (0.5 inch) chert type aggregate of moderate absorption but low permeability (fine pores) can survive freeze-thaw cycles successfully, whereas for a high-permeability aggregate such as dolomite, the critical aggregate size to withstand frost damage can be as high as 83.8 cm (33 inches) [27]. Another study performed by Stark and Klieger verified that the reduction in the nominal maximum size of crushed limestone aggregates improves the durability of concrete pavement [29].

To investigate the role of maximum aggregate size on D-cracking, two examples are examined:

- A high-porosity ($\phi_o^a = 0.1$), low-permeability ($k^a = 1.7\times10^{-21}\text{m}^2$) aggregate with fine pore structure ($m^a = 0.5$), which is vulnerable to D-cracking, is considered. The size of the aggregate is reduced in this case to examine if it improves the aggregate performance under freezing temperature.
- A high-porosity ($\phi_o^a = 0.1$), high-permeability ($k^a = 1.28\times10^{-15}\text{m}^2$) aggregate with fine pore structure ($m^a = 0.5$) and big aggregate size is considered to investigate if it deteriorates the problem.

4.1.2.1 High-Porosity, Low-Permeability Aggregate with Fine Pore Structure

It has already been shown that the high-porosity, low-permeability aggregate with fine pore structure and 0.052 m (2 inch) maximum aggregate size can develop harmful tensile stress at the center of the aggregate. Thus, the size of the aggregate particle is reduced from 0.052 m (2 inches; Subsection 4.1.1.1) to 0.013 m (0.5 inch). For 0.013 m (R_i = 0.00635 m) maximum aggregate size, if a sand of 2.7 fineness modulus is used, the dry-rodded volume fraction of the coarse aggregate is found to be 56% if the concrete is designed according to ACI procedures [23]. The outer diameter of the matrix shell is thus found to be 0.016 m (0.62 inch), with R_o being 0.008 m. Pore liquid pressure, bulk strain, and tangential stress are plotted in Figure 22, Figure 23, and Figure 24, respectively. It is seen that the reduction of maximum aggregate size by four times does not reduces the peak pore pressure but reduces the relaxation time substantially from about 7 hours to 0.7 hours. However, the initial pore pressure being the same, reduction in the pore volume associated with the reduction in the aggregate size increases the initial dilation and correspondingly increases the initial tangential stress, while faster relaxation accompanies faster decay of stress and reduces the magnitude of the peak tensile stress at the outermost fiber of the aggregate. The comparative effect of the aggregate size reduction on the peak stress in the outmost fiber of the aggregate is shown in Figure 25. Thus, this model proves that reducing the size of the high-porosity, low-permeability, fine-pore-structured aggregate improves the performance of the concrete under freezing conditions, which agrees with the empirical findings in the literature [27].

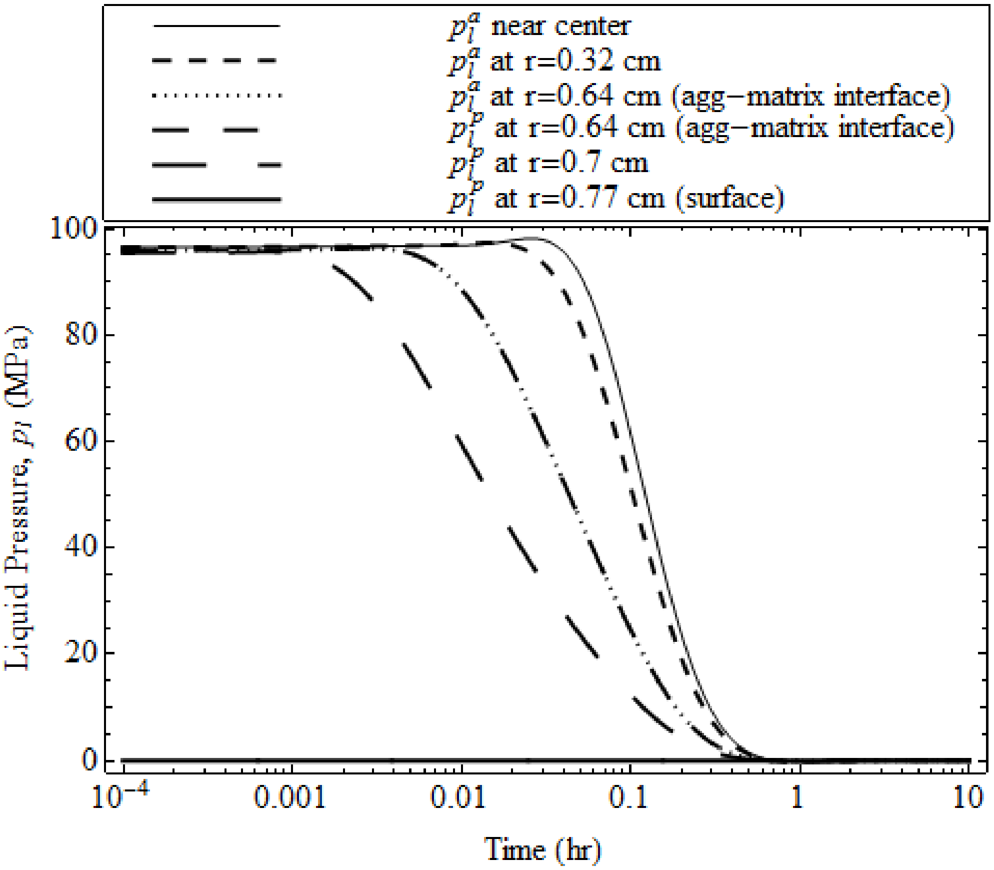

Figure 22. Reduction in aggregate size from 0.052 m to 0.013 m does not reduce the peak pressure of the high-porosity ($\phi_o^a = 0.1$), low-permeability ($k^a = 1.7\times10^{-21}\,\mathrm{m}^2$) aggregate but reduces the relaxation time by an order of magnitude.

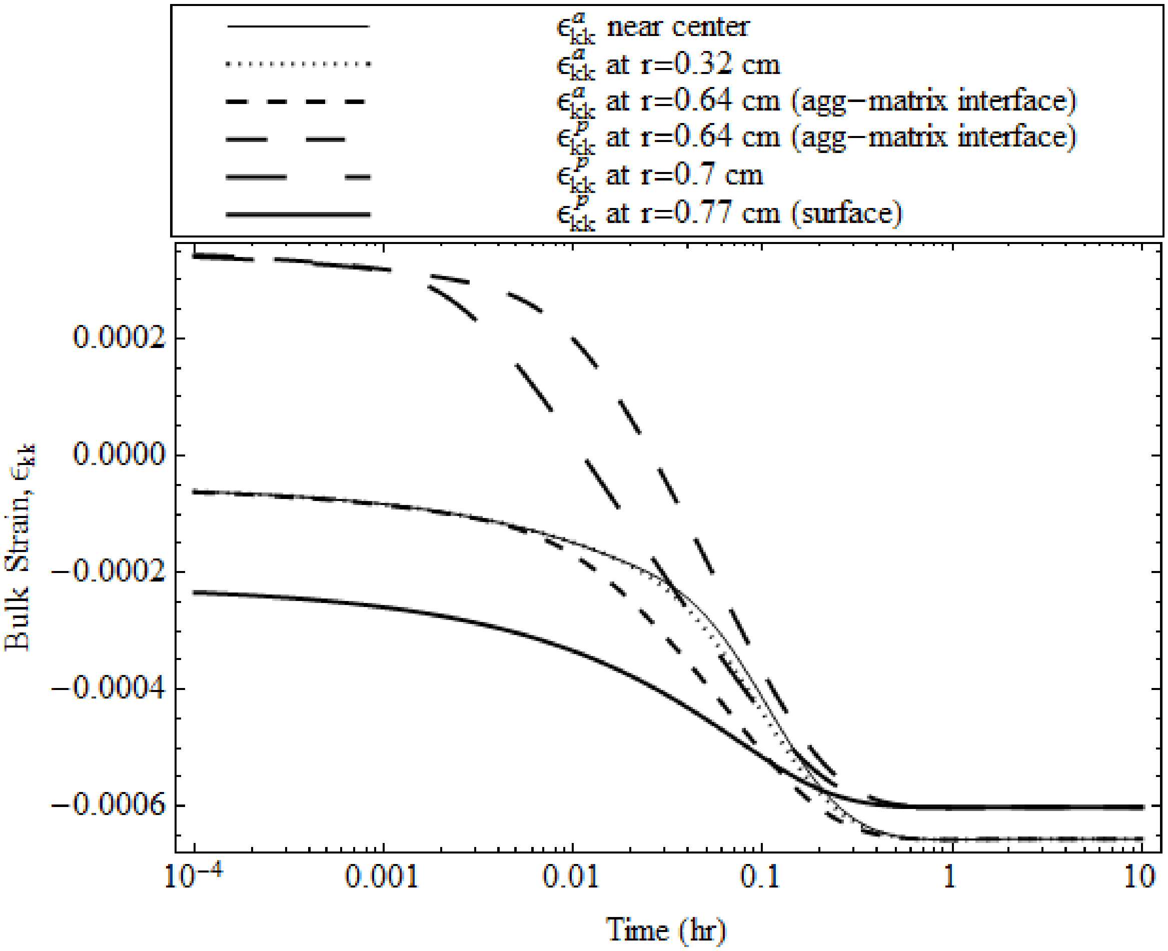

Figure 23. Reduction in aggregate size from 0.052 m to 0.013 m relaxes the strain gradient faster in the high-porosity ($\phi^a_o = 0.1$), low-permeability ($k^a = 1.7\times10^{-21}\,\mathrm{m}^2$) aggregate. However, high pore pressure at the beginning increases the initial dilation to accommodate the reduction in pore volume.

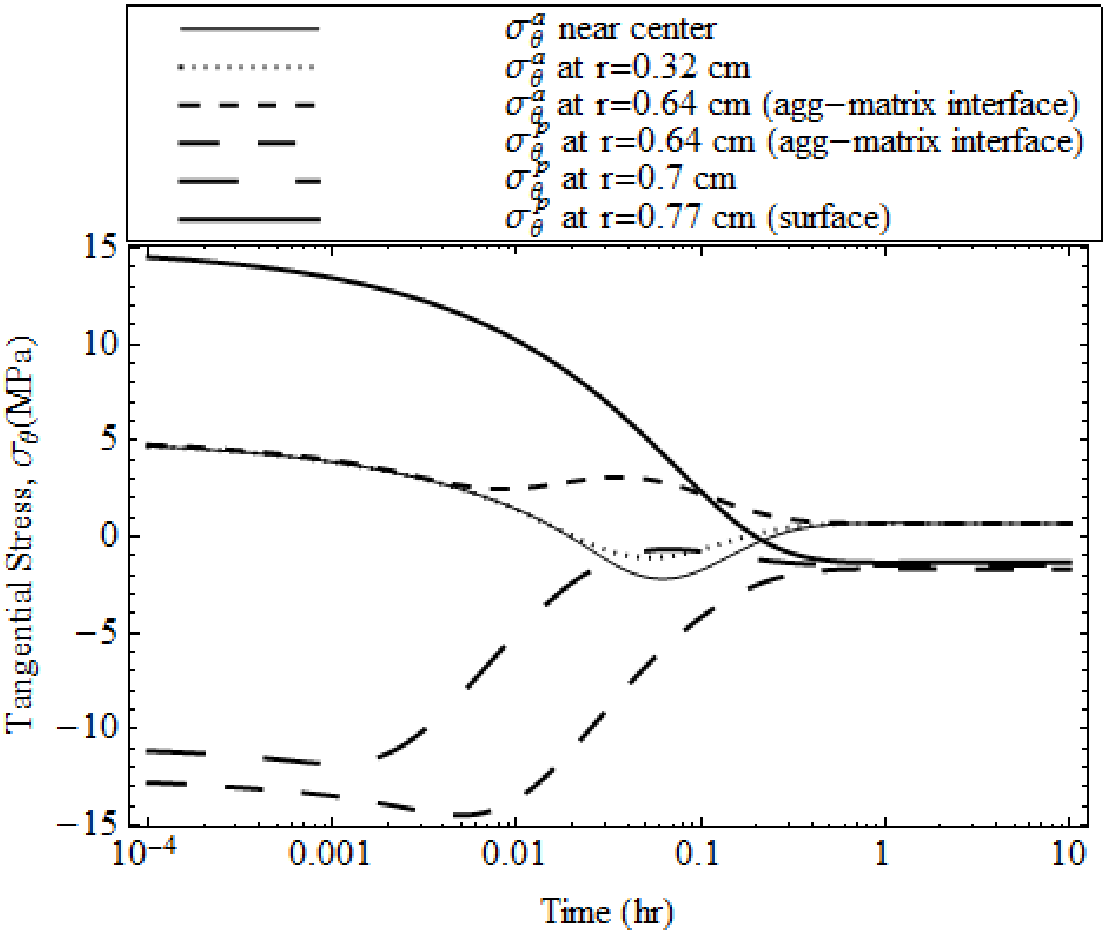

Figure 24. Reduction in aggregate size relaxes the stress faster and reduces the peak tensile tangential stress in the outermost fiber of the aggregate to a negligible amount.

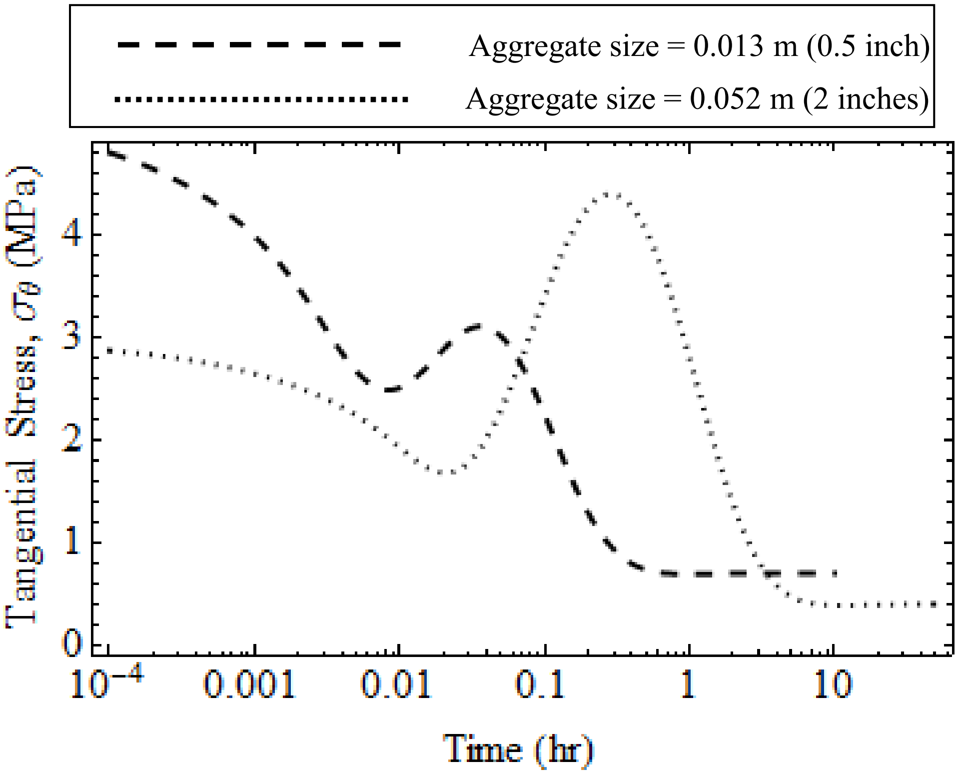

Figure 25. Effect of aggregate size on the peak tensile stress generated in the outermost fiber of the high-porosity ($\phi_o^a = 0.1$), low-permeability ($k^a = 1.7\times10^{-21}\,\mathrm{m}^2$), fine-pore-structured ($m^a = 0.5$) aggregate. Reduction in aggregate size develops higher initial stress to accommodate expansion caused by the high initial pore pressure. However, faster relaxation in the small aggregate reduces the damage propensity and improves the performance under freezing conditions.

4.1.2.2 High-Porosity, High-Permeability Aggregate with Fine Pore Structure

As seen in Subsection 4.1.1.3, high-porosity ($\phi_o^a = 0.1$), high-permeability ($k^a = 1.28\times10^{-15}\,\mathrm{m}^2$), fine-pore-structured ($m^a = 0.5$) aggregates with 0.052 m (2 inch) maximum aggregate size cause high tensile stress at the outermost fiber of the matrix shell but do not cause damage to concrete because of the quick relaxation time. In order to verify if this type of aggregate is prone to damaging the concrete, a bigger aggregate size of 0.15 m (6 inches) is considered. For this maximum aggregate size (R_i = 0.00635 m), according to ACI design procedures, if a sand with a fineness modulus of 2.7 is assumed, the dry-rodded volume fraction of the coarse aggregate is found to be 84% [23]. The outer diameter of the matrix shell is calculated to be 0.16 m (6.34 inches), with R_o being 0.08 m. Results obtained for this analysis are provided in Figure 26, Figure 27, and Figure 28. In this case, increase of aggregate size from 0.052 m (2 inches) to 0.15 m (6 inches) does not increase the peak pore pressure as expected. As a result, increase in pore volume due to the increase in aggregate size reduces the initial dilation (Figure 27) and the associated tensile tangential stress (Figure 28) at the matrix boundary. These high values are the consequence of the instant cooling to a -25 °C, which is unexpected in the field. However, as shown in Figure 29, use of bigger aggregates delays the relaxation time a significant amount, thus exhibiting a high stress in the matrix for a longer period. This may in turn create cracks in the matrix shell, even for slow cycles of freezing and thawing where fatigue tensile stress exceeds the tensile strength of the matrix. Although such freeze-thaw damage originated in the cement matrix resembles the cracking caused by nondurable coarse aggregates, it is not considered D-cracking [10]. However, development of cracks in the matrix may alter the stress state and help initiate and accelerate D-cracking during the successive freeze-thaw cycles when unsound aggregates are present in the concrete. In general, it can be concluded that the use of a small aggregate is beneficial because the harmful tensile tangential stresses at the boundary of the aggregate and the matrix are relaxed quickly due to the short travel path to the escape boundary.

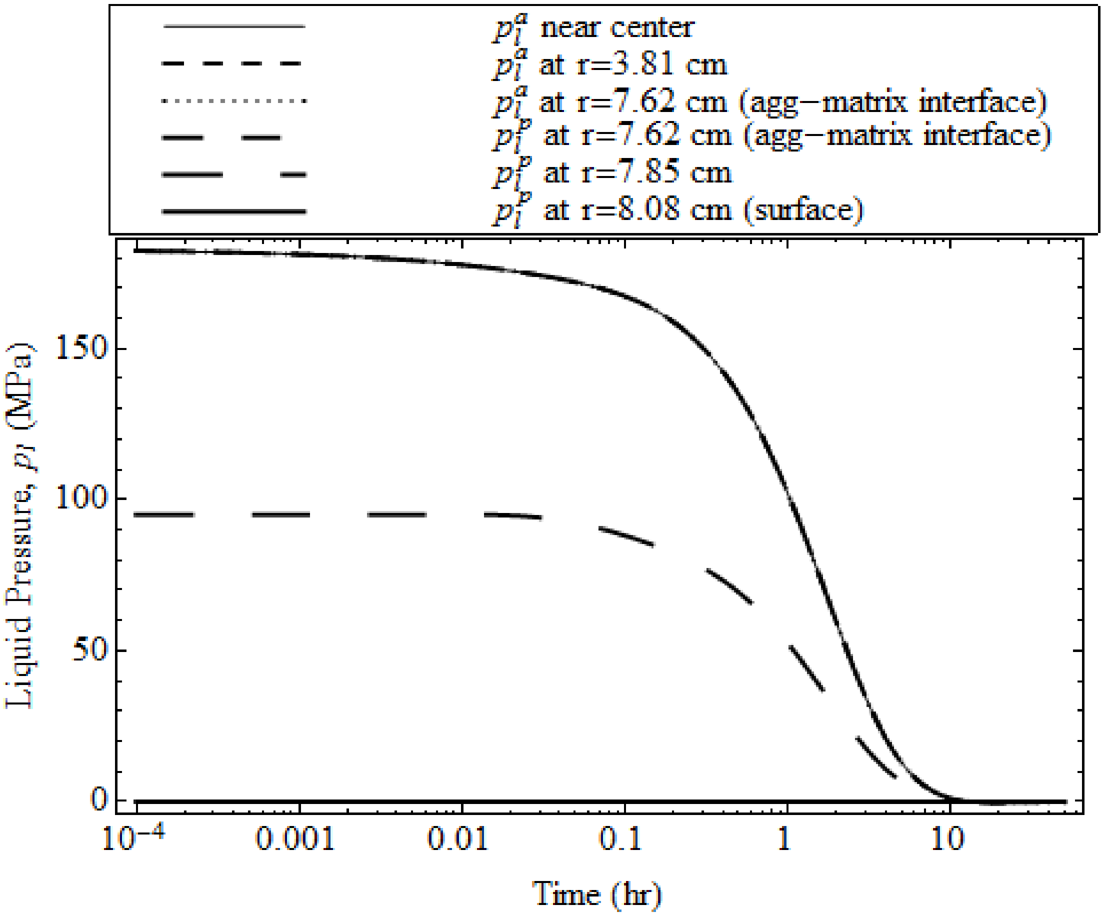

Figure 26. Increase in aggregate size from 0.052 m (2 inches) to 0.15 m (6 inches) does not affect the initial peak pore pressure (see Figure 11) but delays the relaxation time.

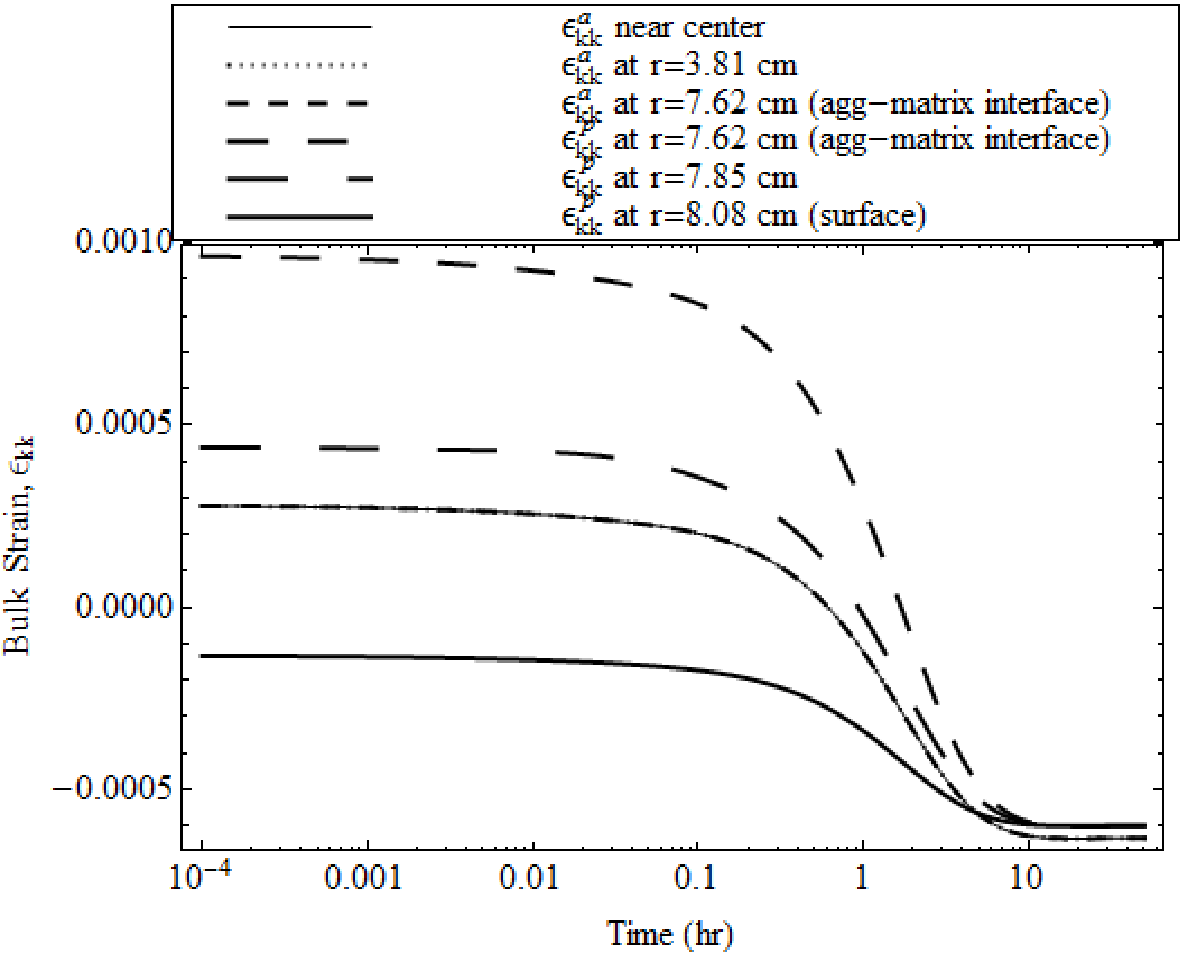

Figure 27. Increase in aggregate size from 0.052 m (2 inches) to 0.15 m (6 inches) decreases the initial dilation but takes hours to reach equilibrium.

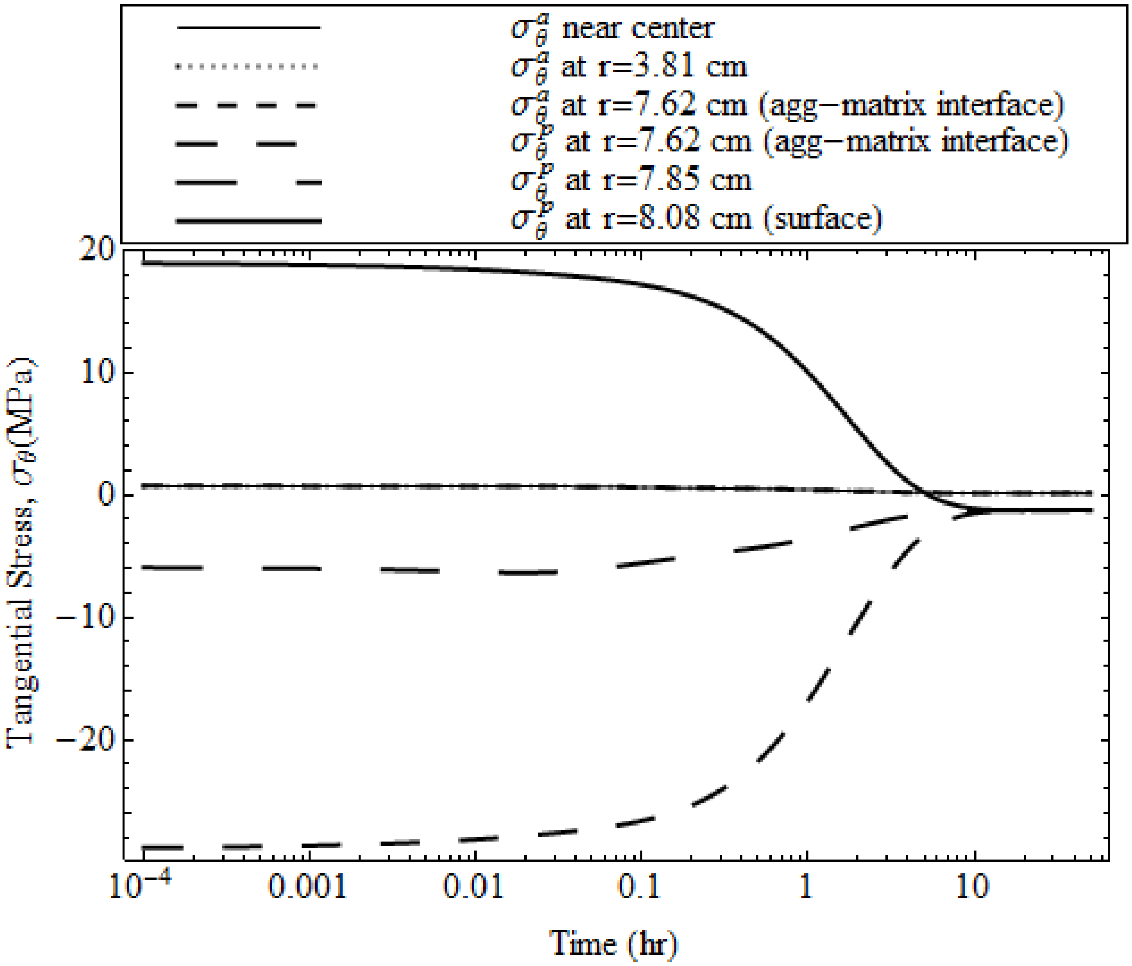

Figure 28. Increase in aggregate size delays the pore pressure relaxation, and the outer boundary of the matrix shell exhibits the peak tensile stress for a long time when a high-porosity ($\phi_o^a = 0.1$), high-permeability ($k^a = 1.28\times10^{-15}\,\mathrm{m}^2$), fine-pore-structured ($m^a = 0.5$) aggregate is used.

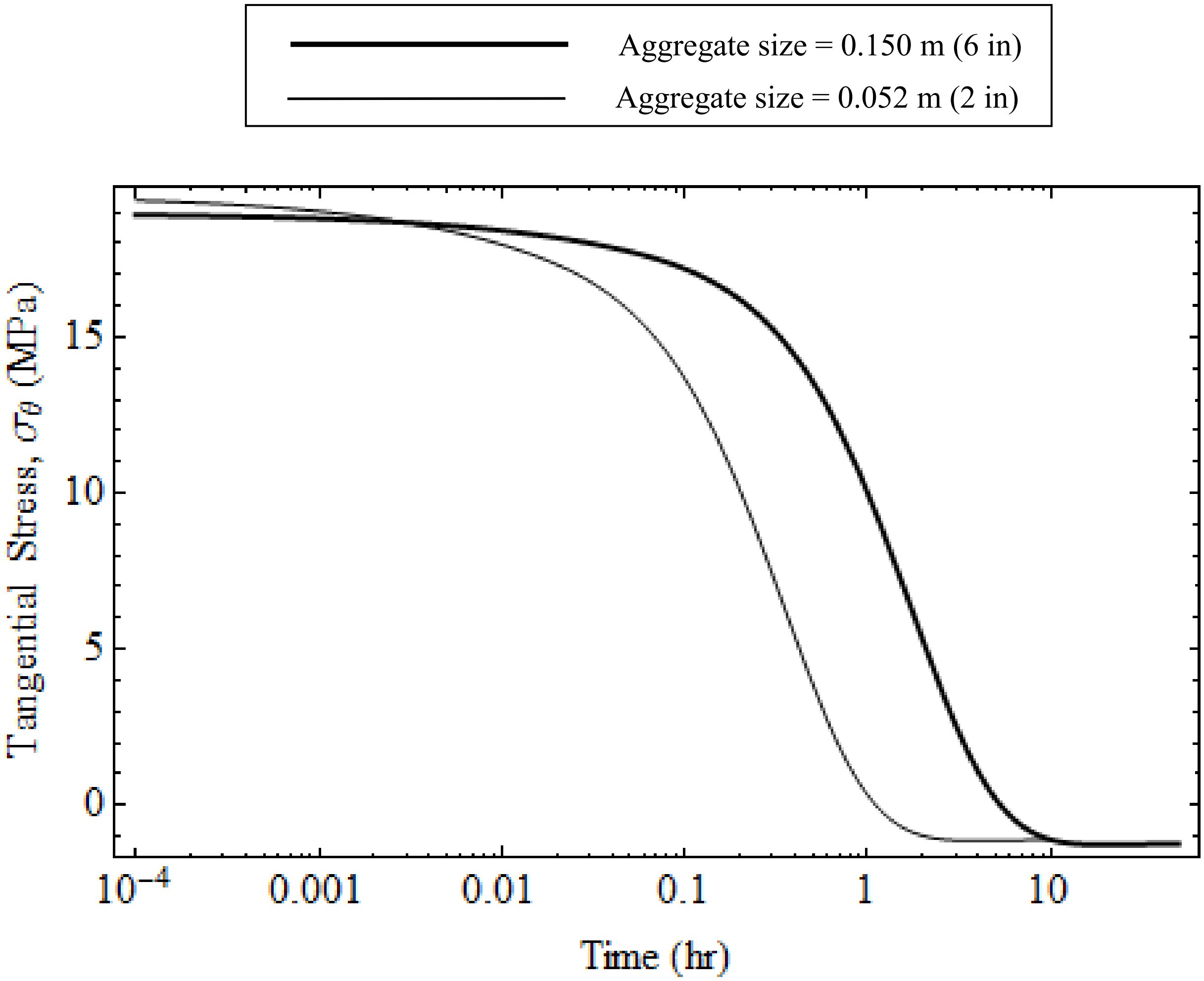

Figure 29. Increase in aggregate size from 0.052 m (2 inches) to 0.15 m (6 inches) slightly decreases the initial peak tensile stress at the boundary of the matrix shell but delays relaxation time by an order of magnitude that is capable of creating cracks in the matrix outmost fiber.

4.1.3 Aggregate Thermal Properties

As reported by Alexander and Mindess [32], the importance of aggregate CTE to the performance of concrete under thermal cycling is twofold: first, it influences the CTE of the concrete and hence thermal movements in structures; and second, it may contribute to the development of internal stresses if there are large differences between the CTEs of the various constituents. Typical values for CTE for various aggregates are reported to vary from $4\times10^{-6}\,^\circ C^{-1}$ to $13\times10^{-6}\,^\circ C^{-1}$ [23], whereas for cement paste, α is reported to be $10\times10^{-6}\,^\circ C^{-1}$ to $20\times10^{-6}\,^\circ C^{-1}$ [40], and for concrete, it varies from about 6 to $14\times10^{-6}\,^\circ C^{-1}$, with an average value of about $10\times10^{-6}\,^\circ C^{-1}$ [32]. α is reported to be $7.4\times10^{-6}\,^\circ C^{-1}$ for Elgin sand mortar and

$9.9\times10^{-6}{}^{\circ}\mathrm{C}^{-1}$ for Ottawa sand mortar [41]. Callan reported that the limestone-sand mortars have coefficients of $7.2'\ 10^{-6}{}^{\circ}\mathrm{C}^{-1}$ to $9'\ 10^{-6}{}^{\circ}\mathrm{C}^{-1}$, while most natural siliceous-sand mortars have CTEs near $10.8'\ 10^{-6}{}^{\circ}\mathrm{C}^{-1}$ [42]. In the same study, he identified that the durability of the concrete may be considerably low where the difference between the CTEs of coarse aggregate and cement paste is large, and the maximum stress in that case occurs at the aggregate-matrix interfacial boundary. Therefore, the difference between CTEs of coarse aggregate and matrix in which they are embedded should not exceed about $5.4\times10^{-6}{}^{\circ}\mathrm{C}^{-1}$ [42].

Here, a high-porosity ($\phi_o^a = 0.1$), low-permeability ($k^a = 1.7\times10^{-21}\mathrm{m}^2$), fine-pore-structured ($m = 0.5$) aggregate with a low thermal expansion of $4\times10^{-6}{}^{\circ}\mathrm{C}^{-1}$ and a diameter of 0.052 m (2 inches) is considered. The resulting plots for pore water pressure, bulk strain, and tangential stresses are shown in Figure 30, Figure 31, and Figure 32, respectively, and are compared to the results obtained in Subsection 4.1.1.1, where a high-porosity, low-permeability, fine-pore-structured aggregate with $\alpha^a = 10\times10^{-6}{}^{\circ}\mathrm{C}^{-1}$ was used. As shown in Figure 30, change in CTE of the aggregate does not change the peak pore liquid pressure. However, substantial change is observed in the bulk strain and stress distribution. In the present case, as illustrated in Figure 31, the matrix contracts more than the aggregate at the equilibrium because CTE of the aggregate is less than that of the matrix ($\alpha^p = 10\times10^{-6}{}^{\circ}\mathrm{C}^{-1}$). As a result, the peak tensile stress according to this model occurs in the matrix, as shown in Figure 32, and the damage is more likely to occur in the ITZ, since the ITZ has a tensile strength of 0.5 MPa [32]. Similarly, peak tensile tangential stress can be found in the aggregate boundary if the aggregate has a greater CTE than the matrix shell. This is shown in Figure 33, Figure 34, and Figure 35, where the CTE of the aggregate is assumed to have a value of $10\times10^{-6}{}^{\circ}\mathrm{C}^{-1}$ and the matrix CTE is assumed to be $4\times10^{-6}{}^{\circ}\mathrm{C}^{-1}$. As anticipated, higher CTE of the aggregate than the matrix does not influence the peak pore pressure. However, as the aggregate contracts more than the matrix, as shown in Figure 34, the peak tensile tangential stress is developed at the aggregate outmost boundary (see Figure 35), which is in accord with the findings of Callan [42]. Therefore, higher CTE of the aggregate than the matrix can make the aggregate more susceptible to D-cracking than if there is a lower coefficient differential between the aggregate and the matrix. The corresponding results are plotted in Figure 36.

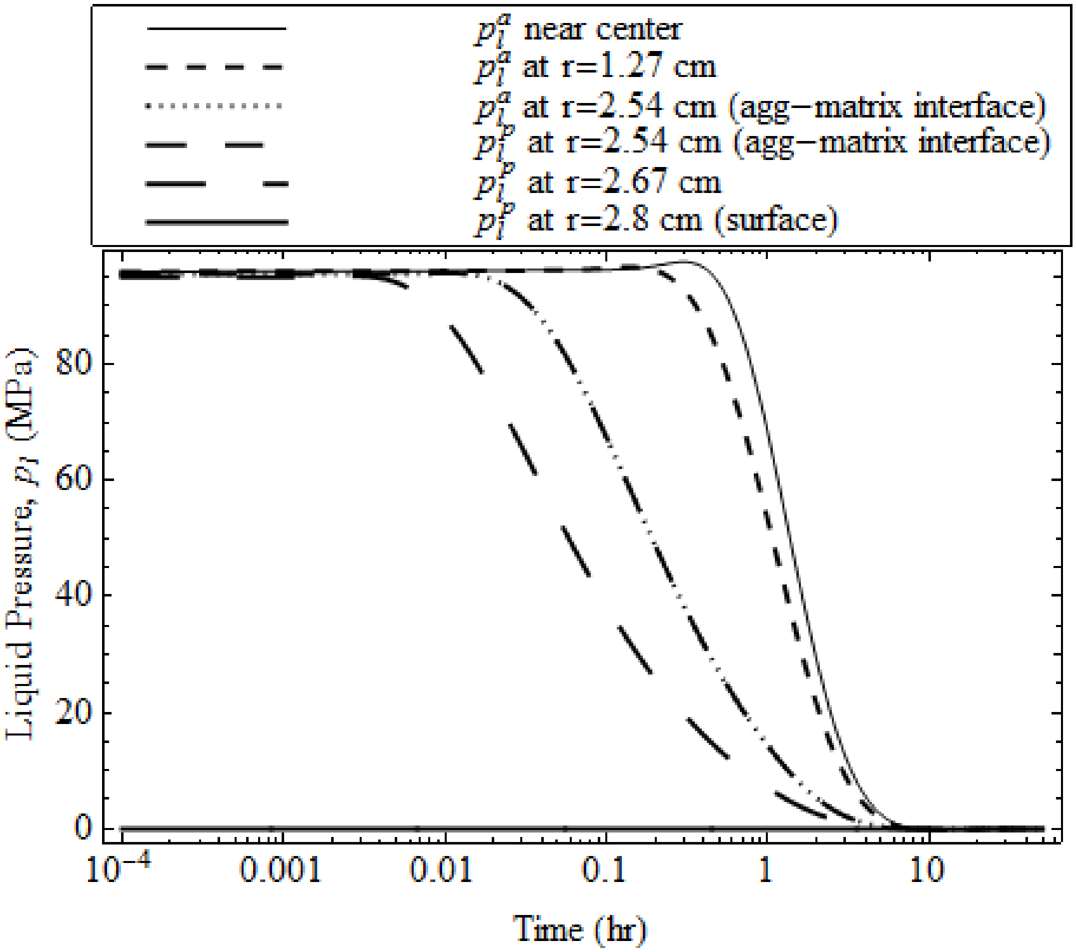

Figure 30. Difference in the CTEs of the aggregate and the matrix does not affect the pressure gradient (see Figure 8).

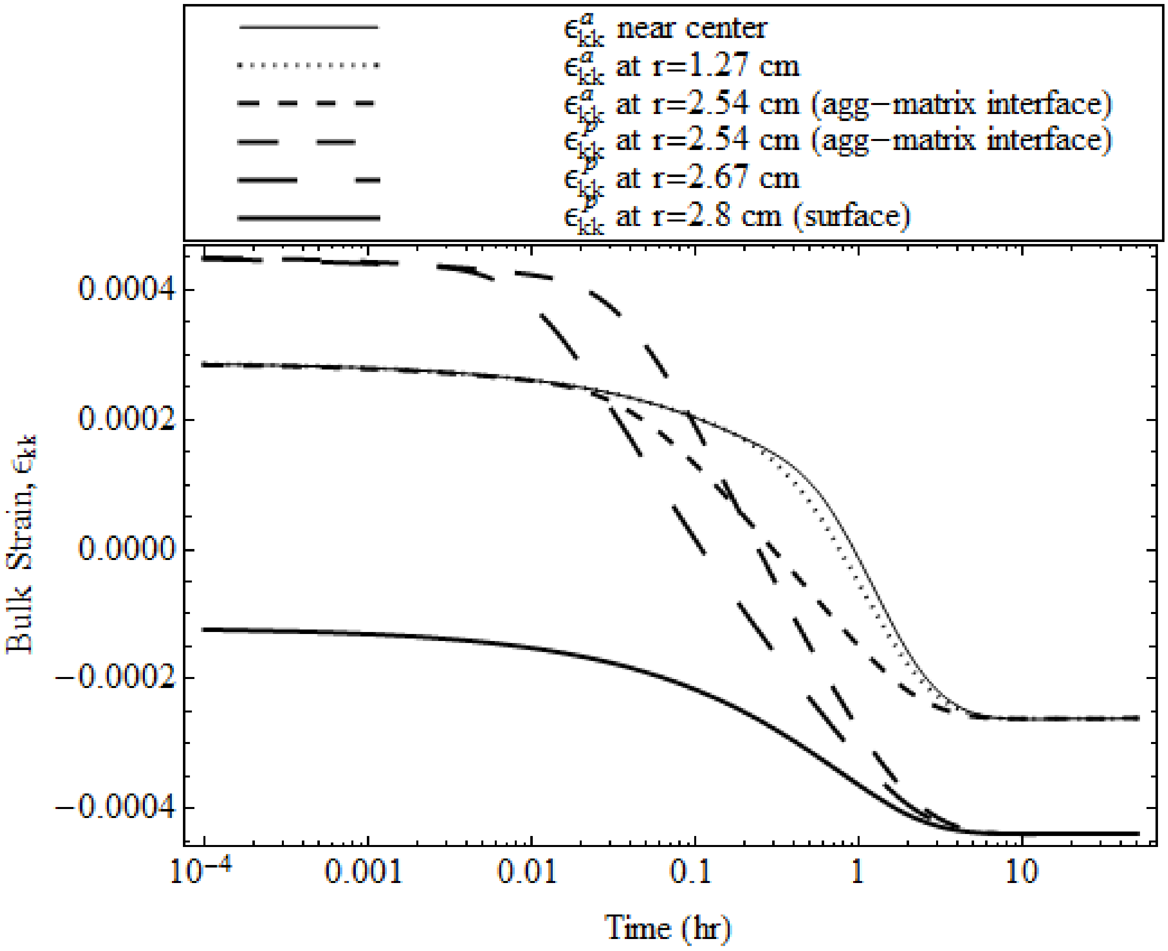

Figure 31. Matrix contracts more at the equilibrium than the aggregate due to the lower CTE of aggregate than that of matrix (see Figure 9).

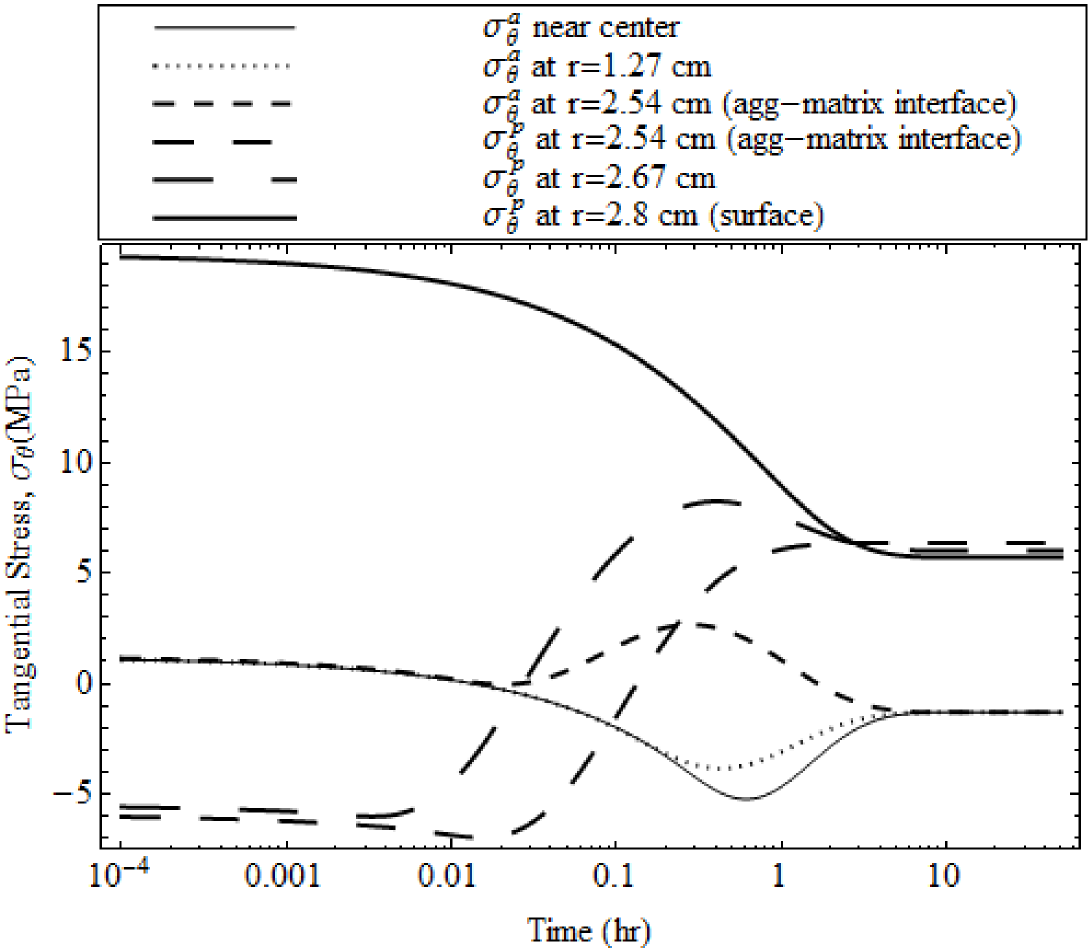

Figure 32. The equilibrium peak tensile stress occurs at the ITZ due to the reduction in the CTE of aggregate, which agrees with the literature [42].

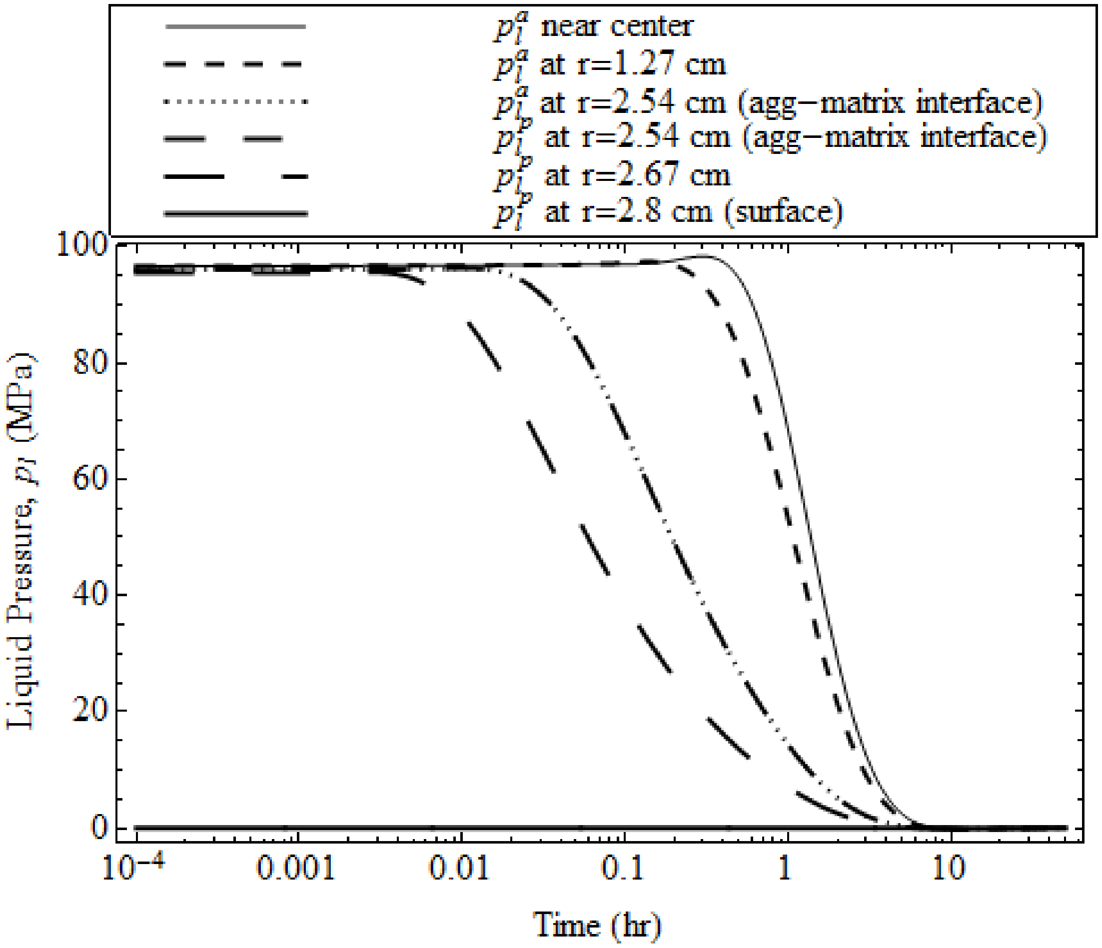

Figure 33. As seen earlier, greater CTE of aggregate than matrix does not change the initial peak pore pressure (see Figure 8 and Figure 30).

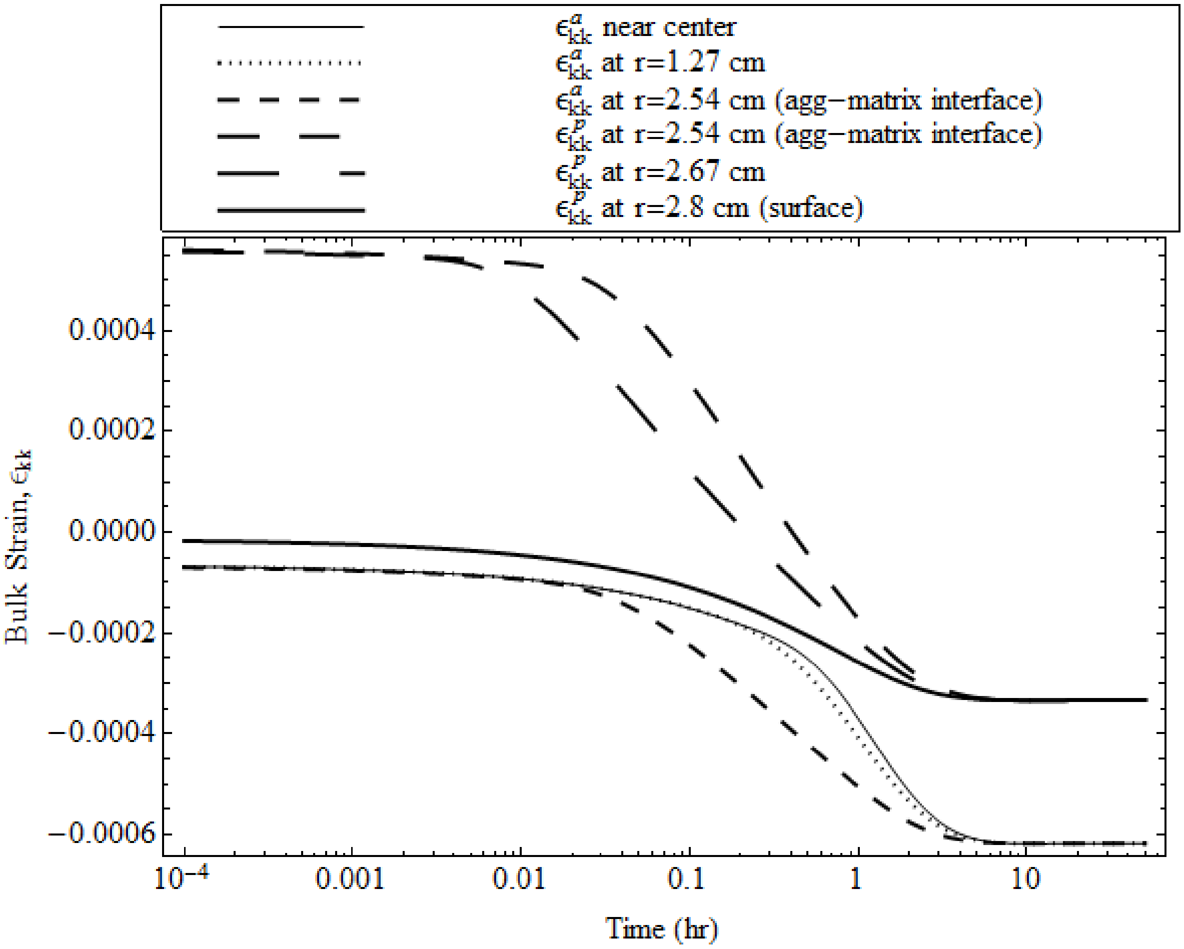

Figure 34. The aggregate contracts more than the matrix at equilibrium because of its higher CTE.

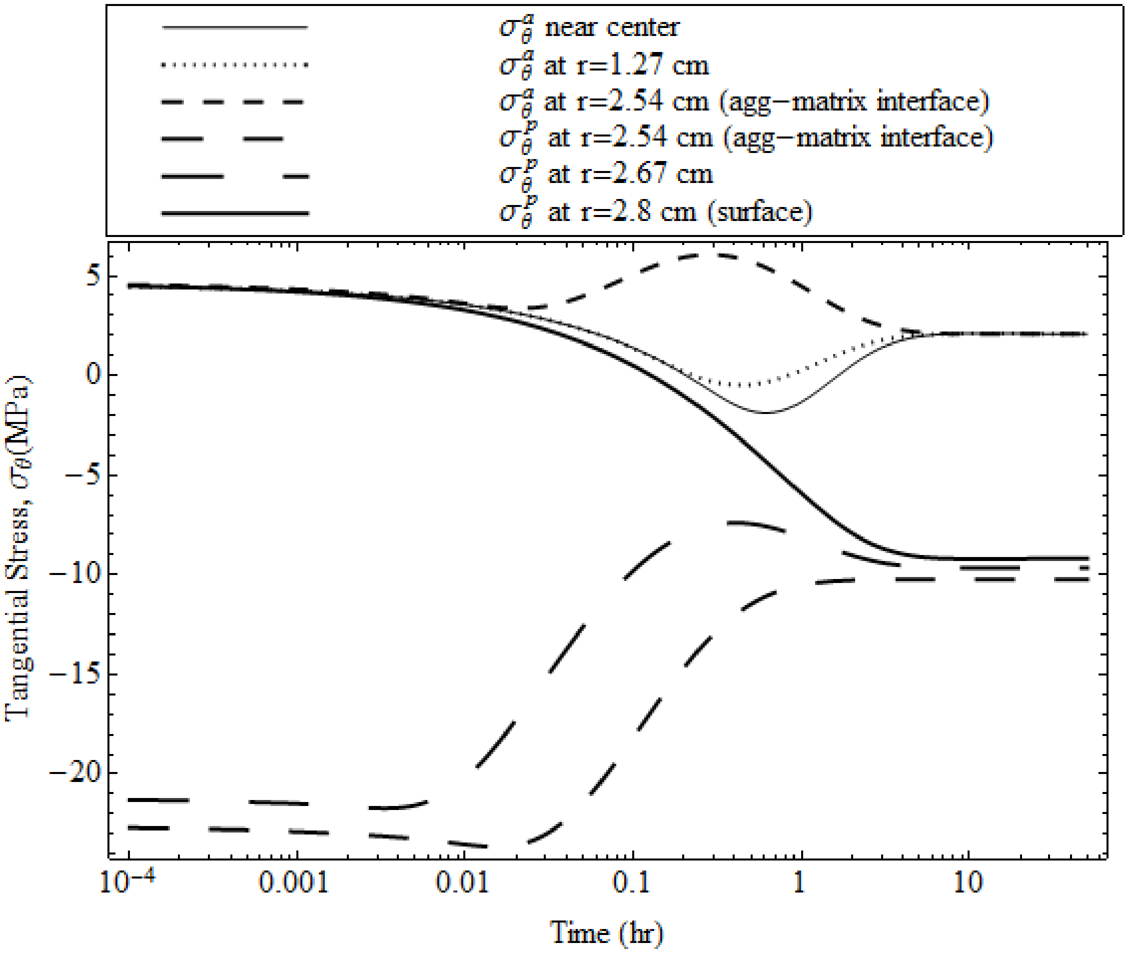

Figure 35. The aggregate contracts more than the matrix and develops delayed peak tensile tangential stress in the aggregate boundary, making it vulnerable to D-cracking.

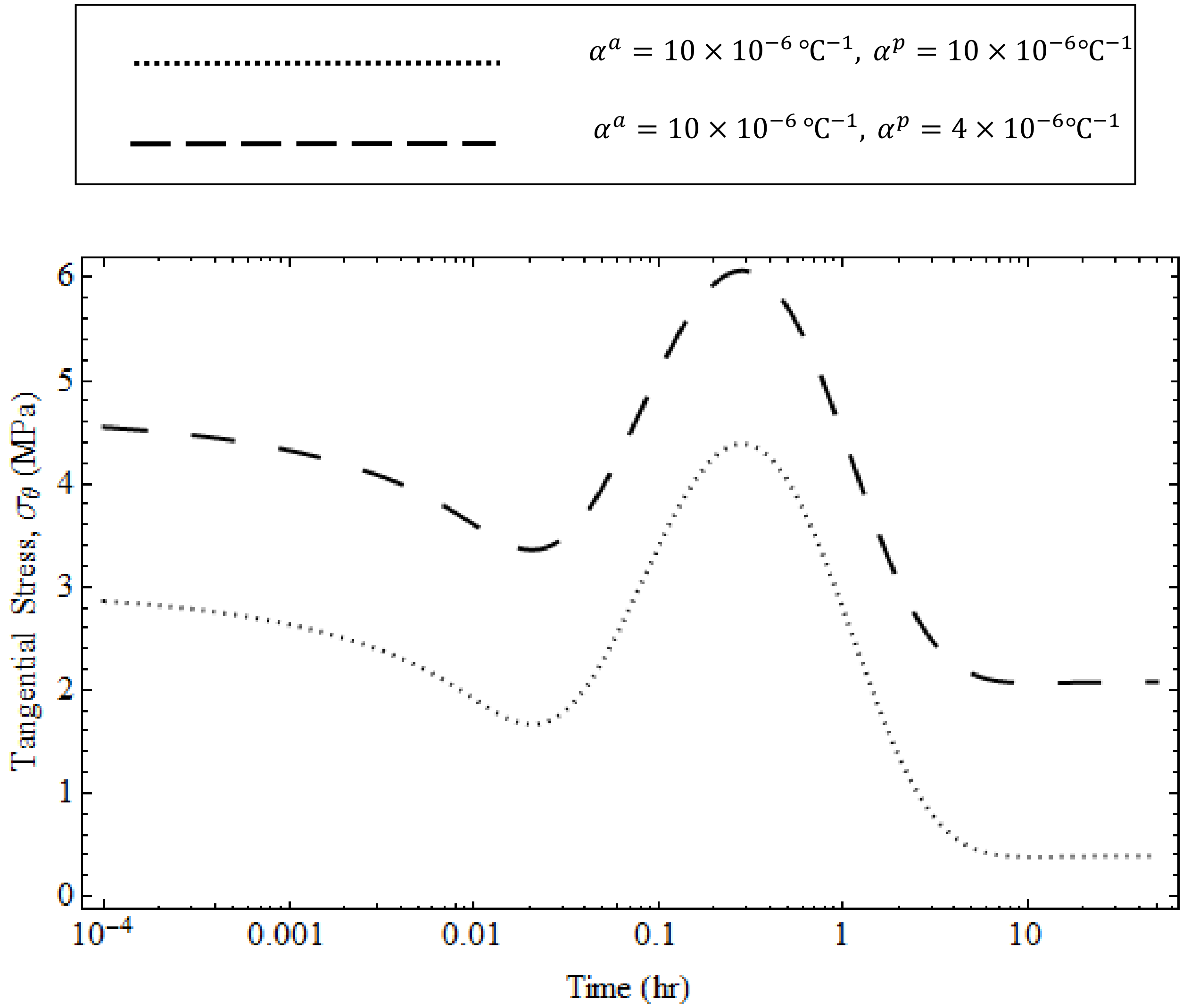

Figure 36. Difference in the CTEs of the aggregate makes concrete more susceptible to D-cracking where aggregate CTE is higher than that of paste. However, peak tensile stress can occur in the ITZ if the matrix CTE is higher than the aggregate. Either way, durability of the concrete is much lower if the difference in the CTEs of the aggregate and the matrix is substantially high.

4.2 Effect of the Matrix Properties

The properties of the matrix, its permeability, porosity, pore structure, air content, CTE, and other physical and poromechanical properties, are also involved in the problem of concrete durability under freezing temperatures. In addition, the matrix can significantly influence the degree of water ingress depending upon the permeability and thickness of the paste or mortar cover that separates the aggregate from the wet surface of the concrete. In this section, the influence of matrix properties on the concrete behavior under freezing temperatures is examined in detail. Two simulations are performed in this section:

- High-porosity, low-permeability, fine-pore-structured aggregate covered with cement paste matrix.
- High-porosity, low-permeability, fine-pore-structured aggregate covered with sand mortar matrix.

4.2.1 Aggregate Covered with Cement Matrix

In this section, a concrete mixture is considered where a high-porosity ($\phi_o^a = 0.1$), low-permeability ($k^a = 1.7\times10^{-21}\,\mathrm{m}^2$), fine-pore-structured ($m^a = 0.5$), 0.052 m (2 inch) aggregate with low CTE of $4\times10^{-6}\,°\mathrm{C}^{-1}$ is covered with cement paste matrix. Elastic Young's modulus, $E^a = 37\times10^3\,\mathrm{MPa}$, is used for the coarse aggregate [43]. K^a is determined using the relation $K^a = E^a / 3(1- 2n^a)$, where n^a is the Poisson's ratio of the aggregate. K_s^a is then calculated using (57) and is found to be 30 × 10^3 MPa. The bulk modulus of the skeleton, K_s, for both concrete and cement paste may vary from $37\times10^3\,\mathrm{MPa}$ to $63\times10^3\,\mathrm{MPa}$, depending on the water-to-cement mass ratio (w/c) and age [34]. Thus, an average of $K_s^p = 45\times10^3\,\mathrm{MPa}$ is used for the cement paste matrix. Studies showed that capillary porosity of the cement paste may range from 0.22 to 0.33 for a w/c of 0.47 and can be as high as 0.51 for a w/c of 0.71, depending on the degree of hydration [44]. Permeability of a hardened cement paste is reported to have an average value of about $6\times10^{-20}\,\mathrm{m}^2$ [33]. Therefore, a high-porosity ($\phi_o^p = 0.5$), low-permeability ($k^p = 1\times10^{-21}\,\mathrm{m}^2$), cement paste with fine pore structure ($m^p = 0.5$) is assumed. CTE for the cement paste matrix is assumed to be $10\times10^{-6}\,°\mathrm{C}^{-1}$ [38].

Pore liquid pressure, bulk strain, and tangential stress are plotted in Figure 37, Figure 38, and Figure 39, respectively. It is seen in Figure 37 that pore pressure gradient is observed at the very beginning because of the difference in the bulk modulus of the aggregate and the cement paste matrix. Also, increase in matrix porosity, ϕ_o^p, from 0.2 to 0.5 induces high expansion in the paste, as shown in Figure 38. As the porosity of the paste is considered high, huge cryo-swelling caused by the density difference between liquid water and ice crystals overcomes the contraction of the solid skeleton and already-frozen ice crystals. The aggregate, on the other hand, undergoes less expansion, which creates destructive tensile stress in the aggregate and at the outermost fiber of the paste matrix (Figure 39). This is further exacerbated by the delayed harmful tensile stress in the aggregate boundary caused by the Mandel-Cryer effect [20]. With successive freeze-thaw cycles, substantial damage in this case may result in the aggregate outmost fiber. Comparison with the results obtained in Subsection 4.1.3 (Figure 32) shows that high porosity, low permeability, and fine pore structure of the cement paste matrix creates high tensile tangential stress at the aggregate boundary (see Figure 40) and has high potential to cause D-cracking.

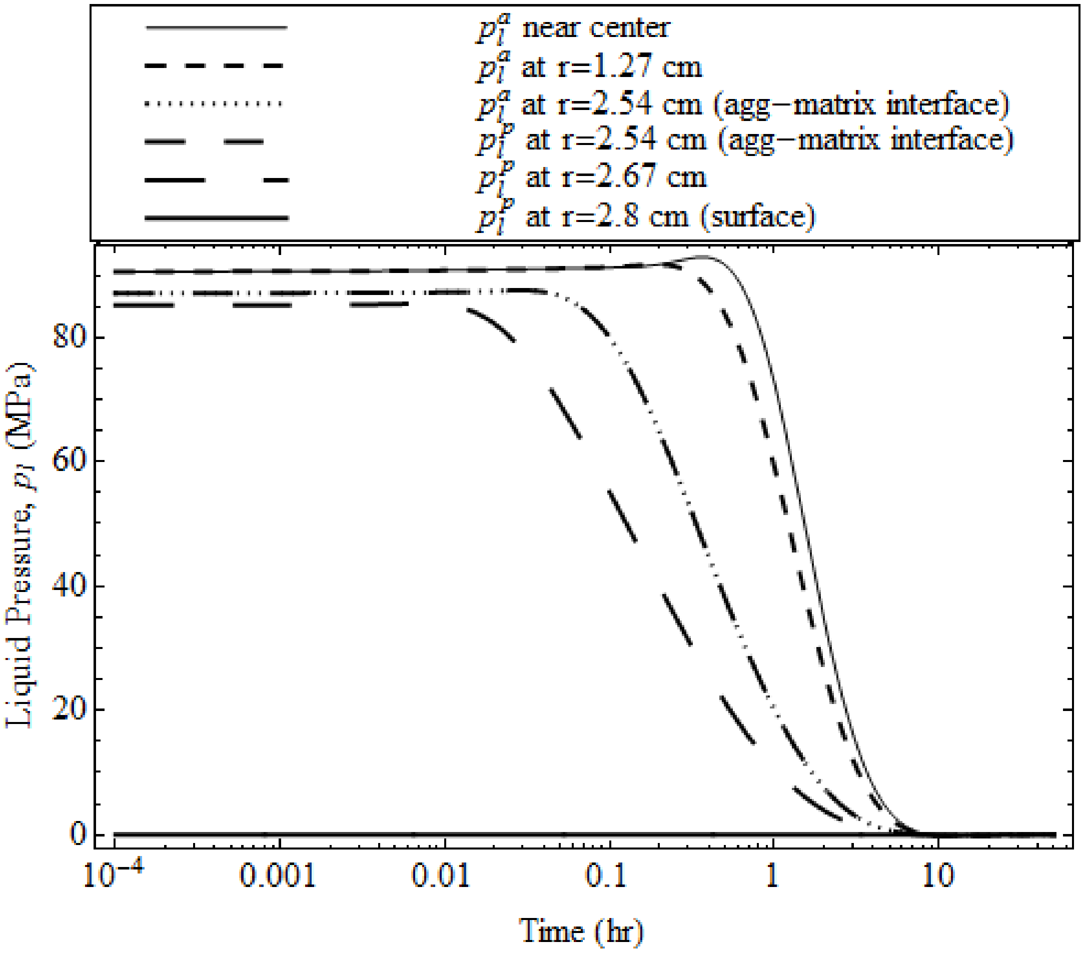

Figure 37. Pore pressure gradient in the concrete sphere, where a low-permeability, high-porosity, fine-pore-structured aggregate is covered with high-porosity, low-permeability cement paste matrix.

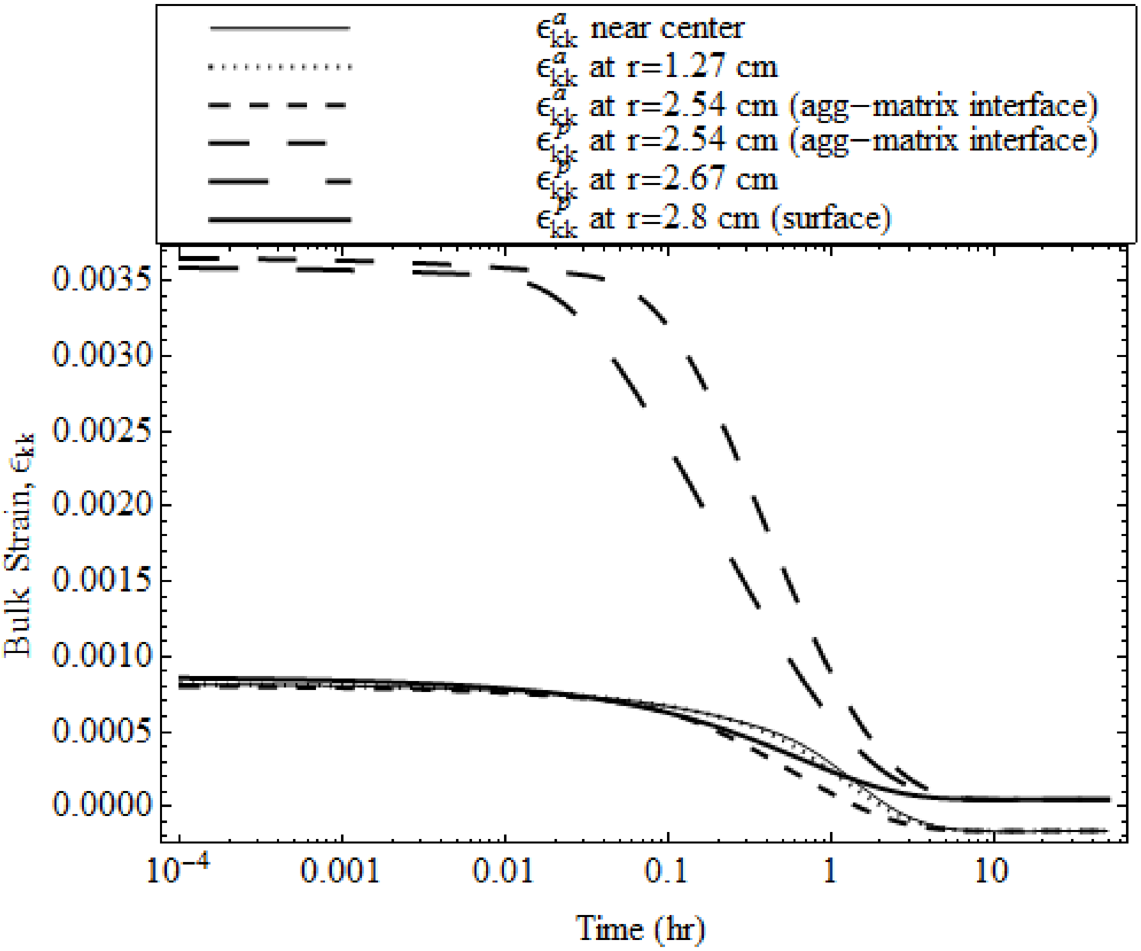

Figure 38. Strain differential in the concrete sphere, where a low-permeability, high-porosity, fine-pore-structured aggregate is covered with high-porosity, low-permeability cement paste matrix.

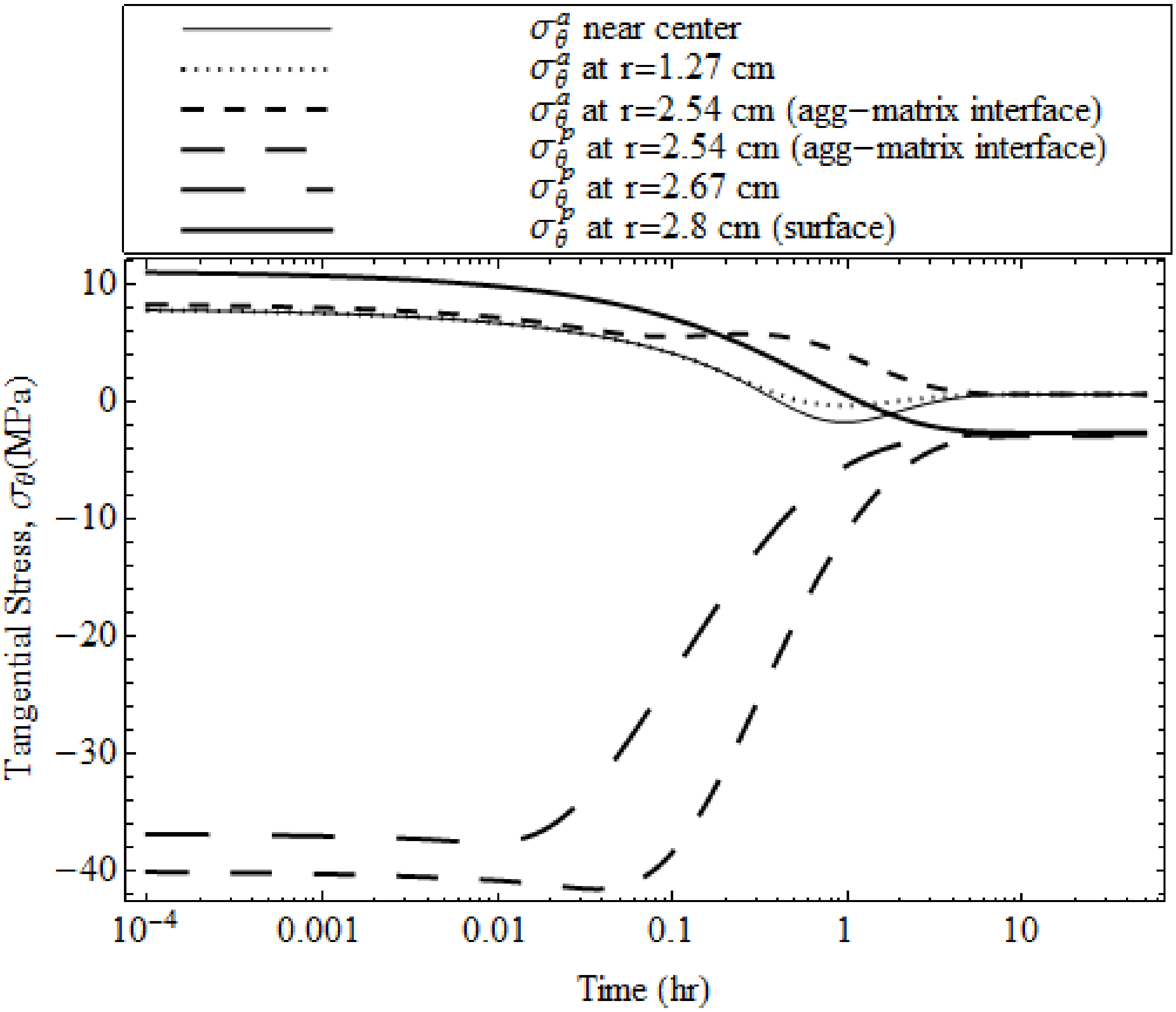

Figure 39. Although peak tensile stress is generated in the cement paste matrix, it dissipates within an hour, reducing the damage susceptibility. However, delayed tensile tangential stress developed in the aggregate boundary has the potential to create D-cracking.

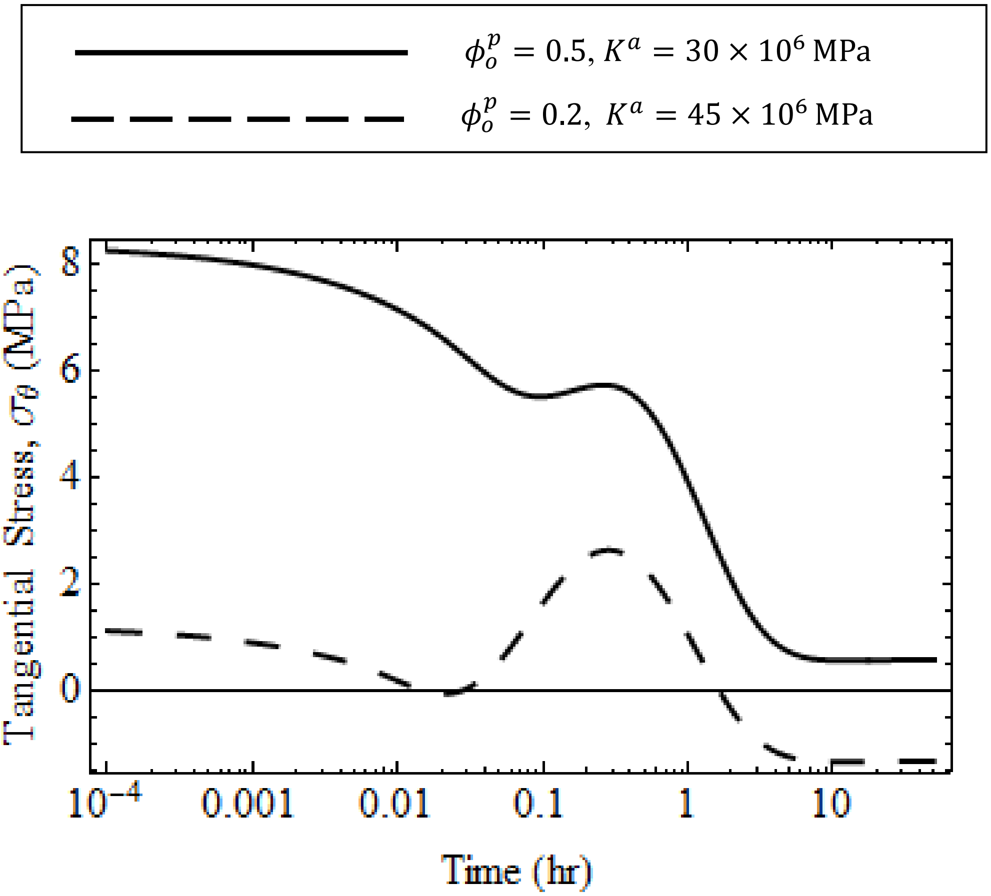

Figure 40. Increase in the porosity of the cement paste matrix causes huge expansion in the cement paste matrix compared to the aggregate and creates high tension in the aggregate boundary.

4.2.2 Aggregate Covered with Mortar Matrix

A high-porosity ($\phi_o^a = 0.1$), low-permeability ($k^a = 1.7\times10^{-21}\,\text{m}^2$), fine-pore-structured ($m^a = 0.5$), 0.052 m (2 inch) aggregate with a low CTE of 4×10^{-6}°C^{-1} is considered to be covered with a sand mortar matrix. For mortar with a w/c of 0.55, a^p can vary from 0.31 to 0.37, depending on the air content [45]. Wong reported values for mortar porosity varying from 0.11 for 60% sand by volume to 0.26 for 10% sand with a w/c of 0.5 [46]. Corresponding permeability has been measured to range between $8.3\times10^{-17}\,\text{m}^2$ to $5\times10^{-16}\,\text{m}^2$ [46]. E^p is assumed to have a value of $16'\ 10^3$MPa [45]. Assuming Poisson's ratio of mortar, n^p, as being 0.2, K^p is then determined using the relation $K^p = E^p / 3(1-\ 2n^p)$. Using (0), K_s^p is calculated to be 13.9×10^3 MPa, for which $f_o^p = 0.2$ is assumed. α^p is assumed to be 10×10^{-6}°C^{-1} for mortar [41].

Figure 41 shows the pore pressure gradient generated in the aggregate covered with a mortar shell. Since a very low bulk modulus is used for mortar, comparatively low pore pressure occurs in the matrix. Also, high swelling is observed in the mortar interior (Figure 42), which results in high tangential stress in the aggregate outmost fiber, as shown in Figure 43. Therefore, decrease in the bulk modulus of the matrix increases the initial expansion of the matrix surrounding the aggregate and induces high tensile tangential stress at the aggregate boundary. It is interesting to note that even though there is a high difference in the CTEs of the aggregate and the matrix, the equilibrium strain is the same for both of the constituent materials. Here, because of the high modulus, the equilibrium strain is dictated by the aggregate.

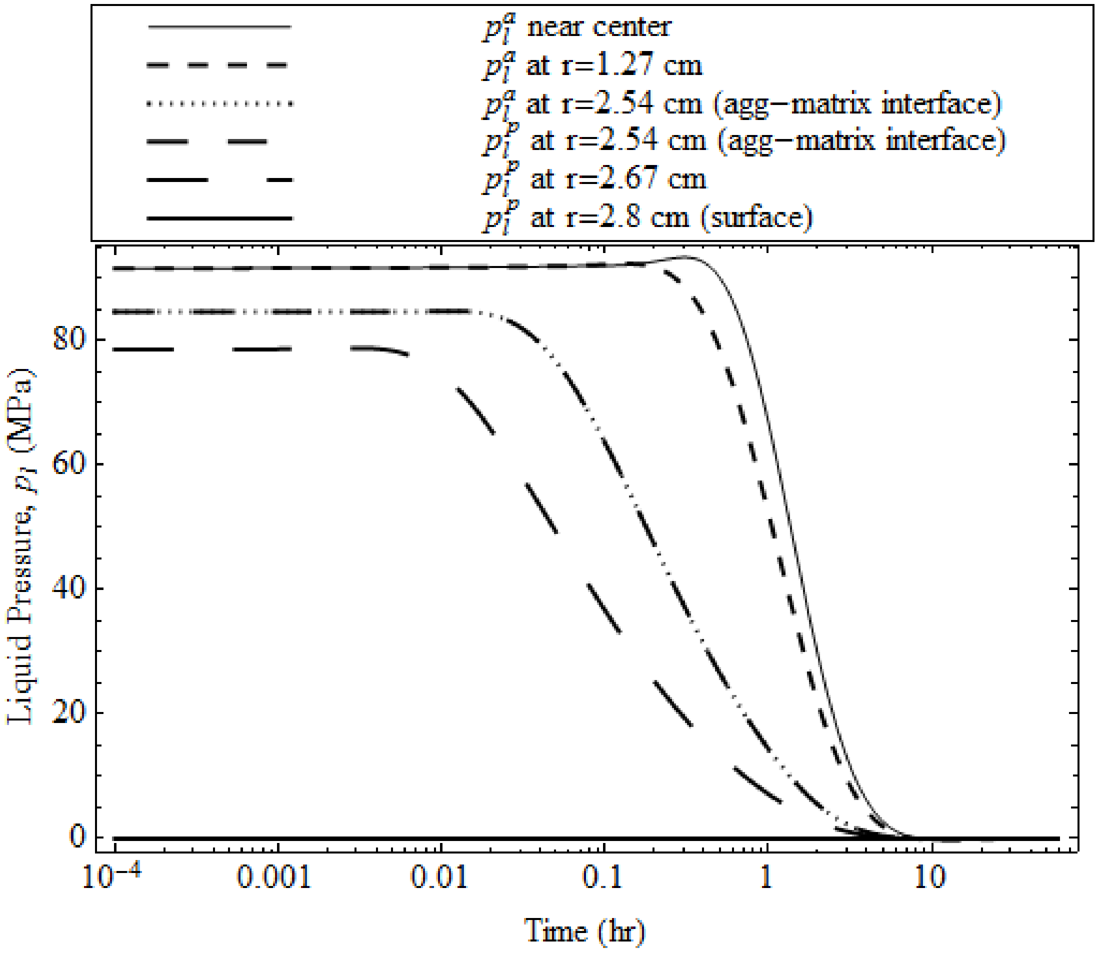

Figure 41. Pressure gradient in the concrete sphere containing high-porosity, low-permeability aggregate core and mortar shell.

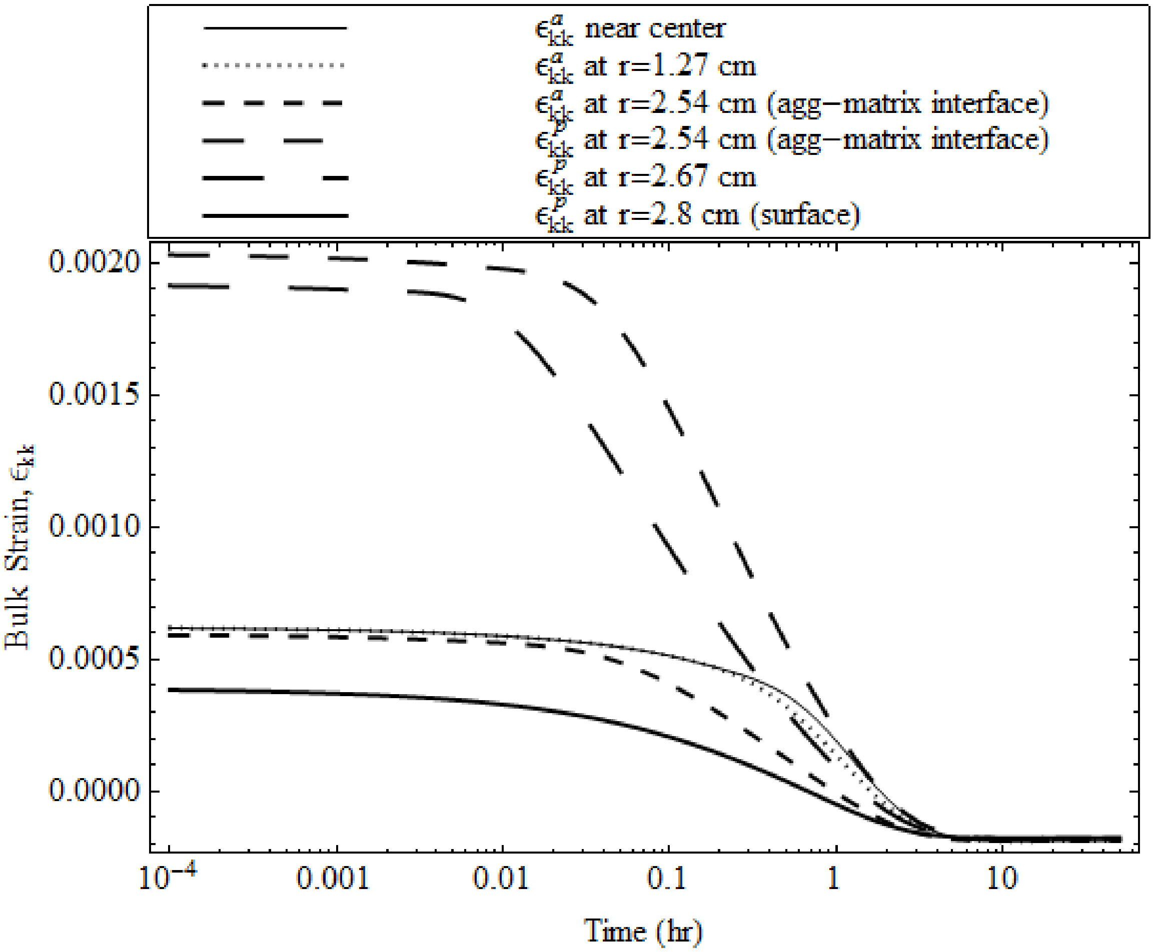

Figure 42. Strain differential in concrete sphere with a high-porosity, low-permeability aggregate covered with mortar matrix.

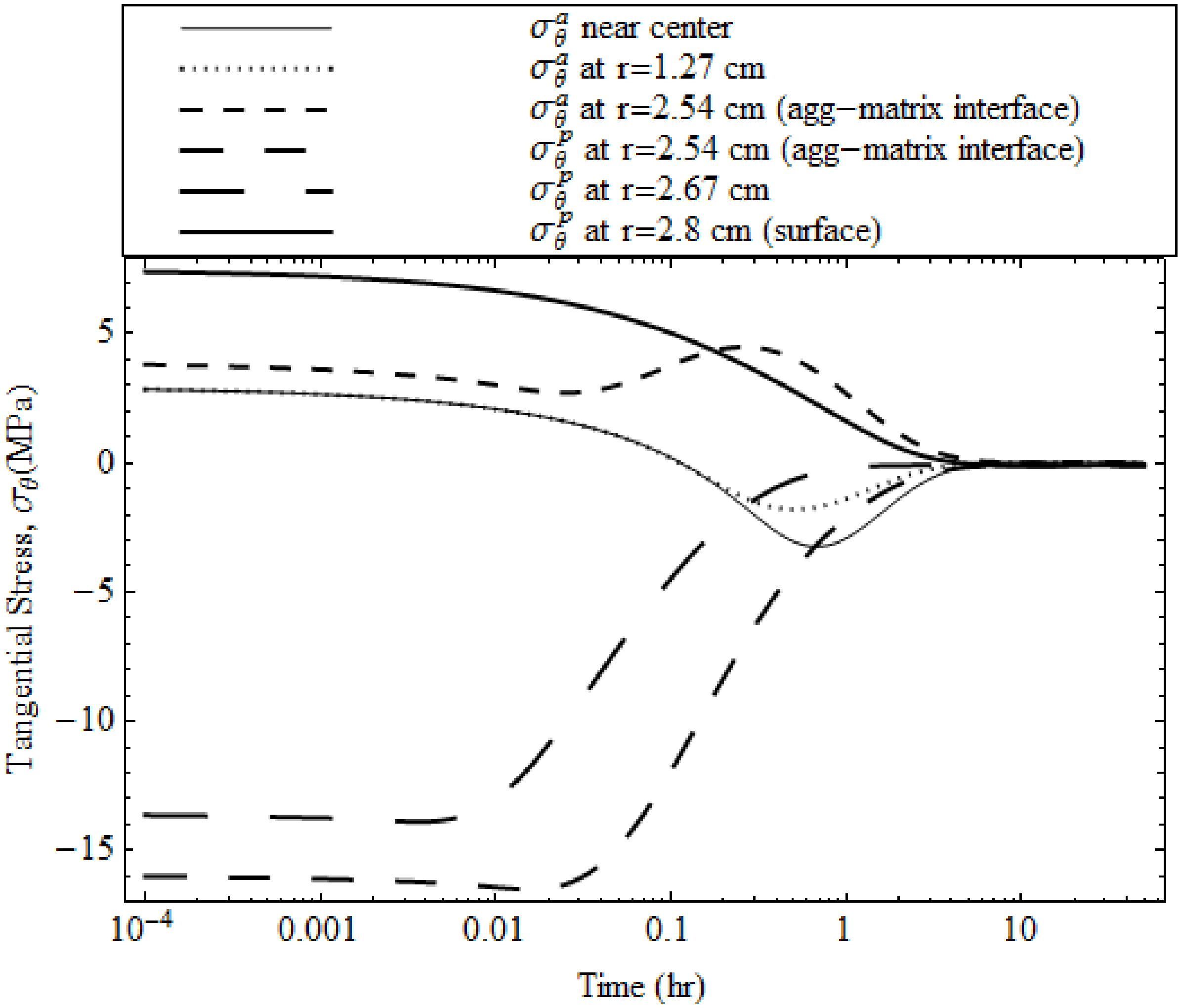

Figure 43. Tangential stress generated in the concrete sphere of a low-permeability aggregate covered with a mortar shell of low bulk modulus and low porosity.

4.3 Effect of Air Entrainment

It has already been established by the proposed model that instantaneous cooling may cause severe damage to the concrete. Previous studies show that air-entrained void can act as an expansion reservoir and cryo-pump and prevent this damage successfully [6], [13]. This section describes how the proposed model can predict the effect of air entrainment on the cryo-deformation of the concrete sphere. This is done according to the guidelines proposed by Coussy and Monteiro [6], [7]. Air voids, when properly distributed in a saturated freezing porous solid, can accommodate the expelled liquid water from the freezing sites, and the liquid water freezes instantly upon entering the air void. Thus, the crystal pressure in the air void is in equilibrium with the atmospheric pressure, and the liquid pressure in the matrix assumes a negative value of

$-\frac{r1}{r\mathrm{c}}\mathrm{S}_{\mathrm{m}}\ \mathrm{DT}$, owing to the solid-liquid thermodynamic equilibrium condition (0). Substitution of $p_l^p = -\frac{r1}{r\mathrm{c}}\mathrm{S}_{\mathrm{m}}\ \mathrm{DT}$ and $p_c^p = 0$ in (0) gives the linear free strain in the matrix:

$$e_f^p = - b_l^p \frac{r1}{r\mathrm{c}} \frac{\mathrm{S}_{\mathrm{m}}\ \mathrm{DT}}{3K^p} - a^p \mathrm{D}T\ . \tag{0}$$

Formulation of (0) assumes the thermodynamic equilibrium in the matrix containing the air voids. Basically, it means that the air voids are so closely spaced that the liquid flows almost instantly to these expansion reservoirs and freezes there, so that no crystal pressure is developed in the matrix pore walls when the temperature is dropped below the freezing point. On the other hand, since there is no entrained air void in the aggregates, positive pore liquid pressure is developed initially, and this pressure has to be determined using the continuity equation, (0), as explained in Section 2.2.

To model the effect of air entrainment, similar material properties as those used in Subsection 4.2.2 are considered, where a high-porosity, low-permeability, fine-pore-structured aggregate is assumed to be embedded in a low-porosity, low-permeability sand mortar matrix. The temperature is lowered to -100 ºC at a cooling rate of 10 ºC/hour, as shown in Figure 44. The volume average bulk strain is then plotted and compared to that for the same material without air voids (Subsection 4.2.2). The resulting plots are shown in Figure 45. It is seen that the volume average bulk strain for the non-air-entrained concrete sphere shows an initial dilation and starts to shrink until t = 0.5 hours, when it jumps up and shows a hump before it starts contracting again at around t = 2 hours. Similar results are shown by Tognon [47] for concrete specimens undergoing cryogenic deformations. It is also seen that after t = 7 hours, at high temperatures (> 70 ºC), the concrete sphere starts to dilate, probably because a majority of the pore volume at that temperature is invaded by ice crystals developing huge crystallization pressure. However, for the air-entrained concrete, no dilation is observed at all, and a substantially high shrinkage is seen with time. A recent study by Liu et al. [48] found identical results for a concrete specimen containing 3% air voids exposed to surface water without any salt. The high shrinkage in the air-entrained concrete can be attributed to the thermal contraction and the liquid depressurization induced by the air voids, which act as expansion reservoirs and cryo-pumps [6].

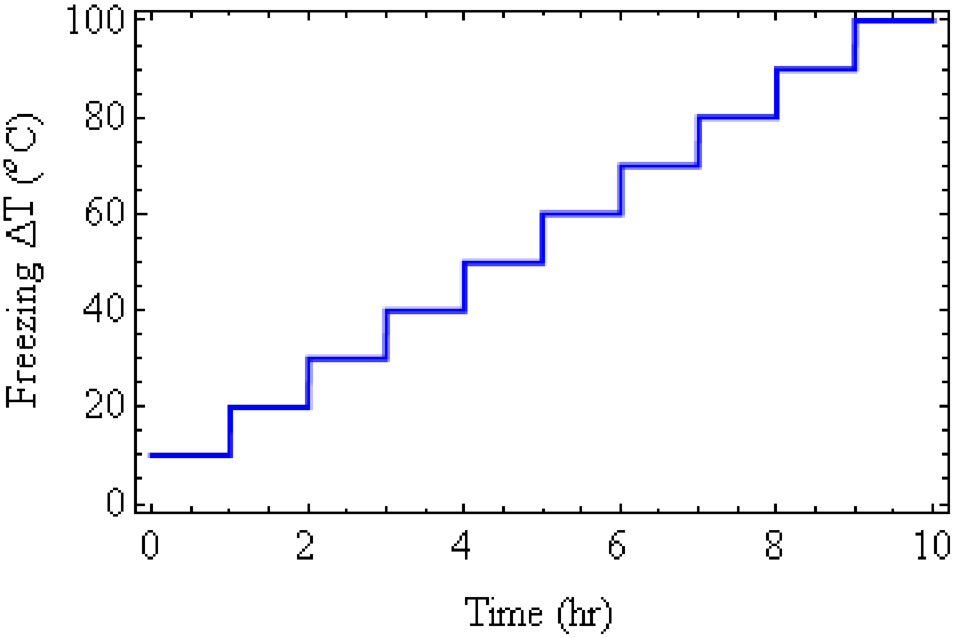

Figure 44. Temperature is lowered to -100 ºC at a rate of 10 ºC/hour.

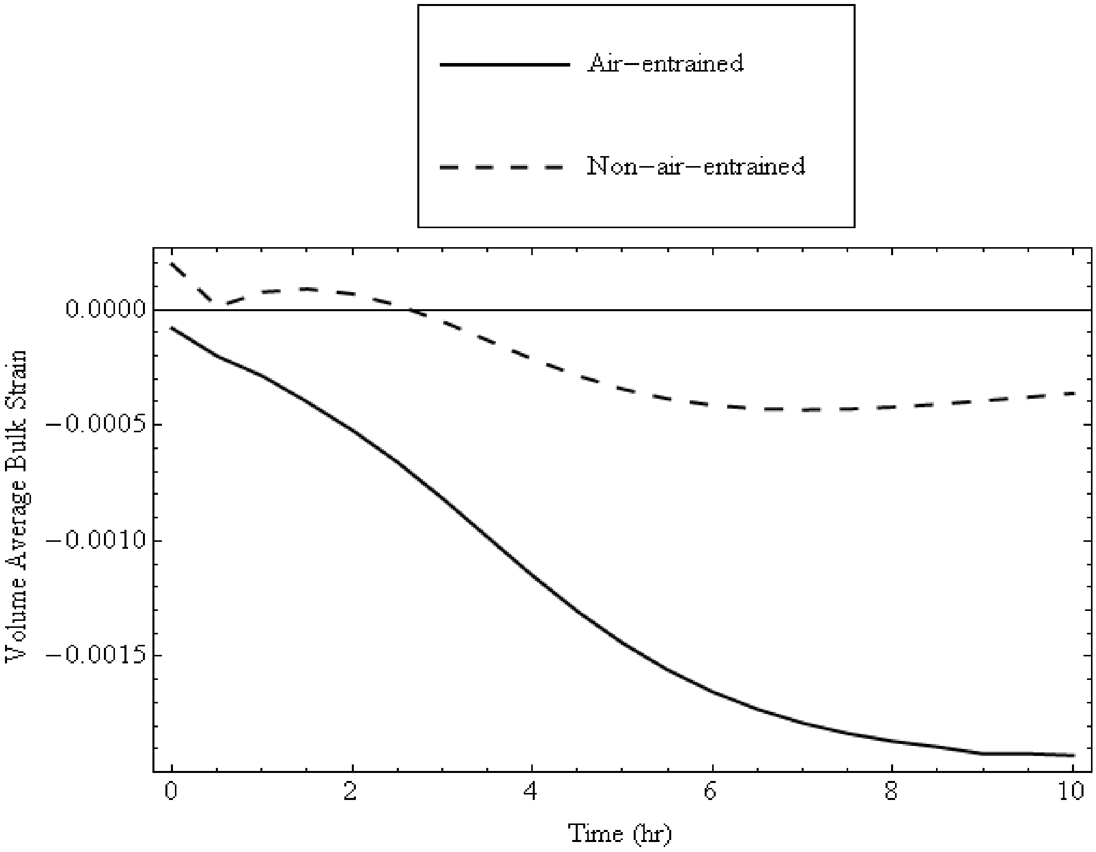

Figure 45. Air-entrained concrete suffers much higher shrinkage than the non-air-entrained concrete, which agrees with the literature [47], [48].

4.4 Effect of Cooling Rate

Studies have shown that the freezing rate has a major influence on the severity of concrete freeze-thaw deterioration [10]. In order to predict the effect of cooling rate on the concrete freeze-thaw durability, two cooling rates of 36 °C/hour and 10 °C/hour are used. In both cases, the temperature is reduced to -100 °C. Similar material properties as those used in Subsection 4.2.2 are assumed. The resulting plots are shown in Figure 46. It is found that Steeper hump is generated for a higher cooling rate, implying that the higher the cooling rate, the less time the pore liquid has to dissipate to the boundary and the higher the dilation. Therefore, rapid cooling is expected to cause more damage than the slow freezing of the material, which is in accord with the findings of Pigeon et al. [49], where declined freeze-thaw durability was found for rapid freezing and thawing laboratory tests. However, a decrease in the freeze-thaw durability in the field with an increase in the cooling rate has also been reported [10], requiring further study on this issue.

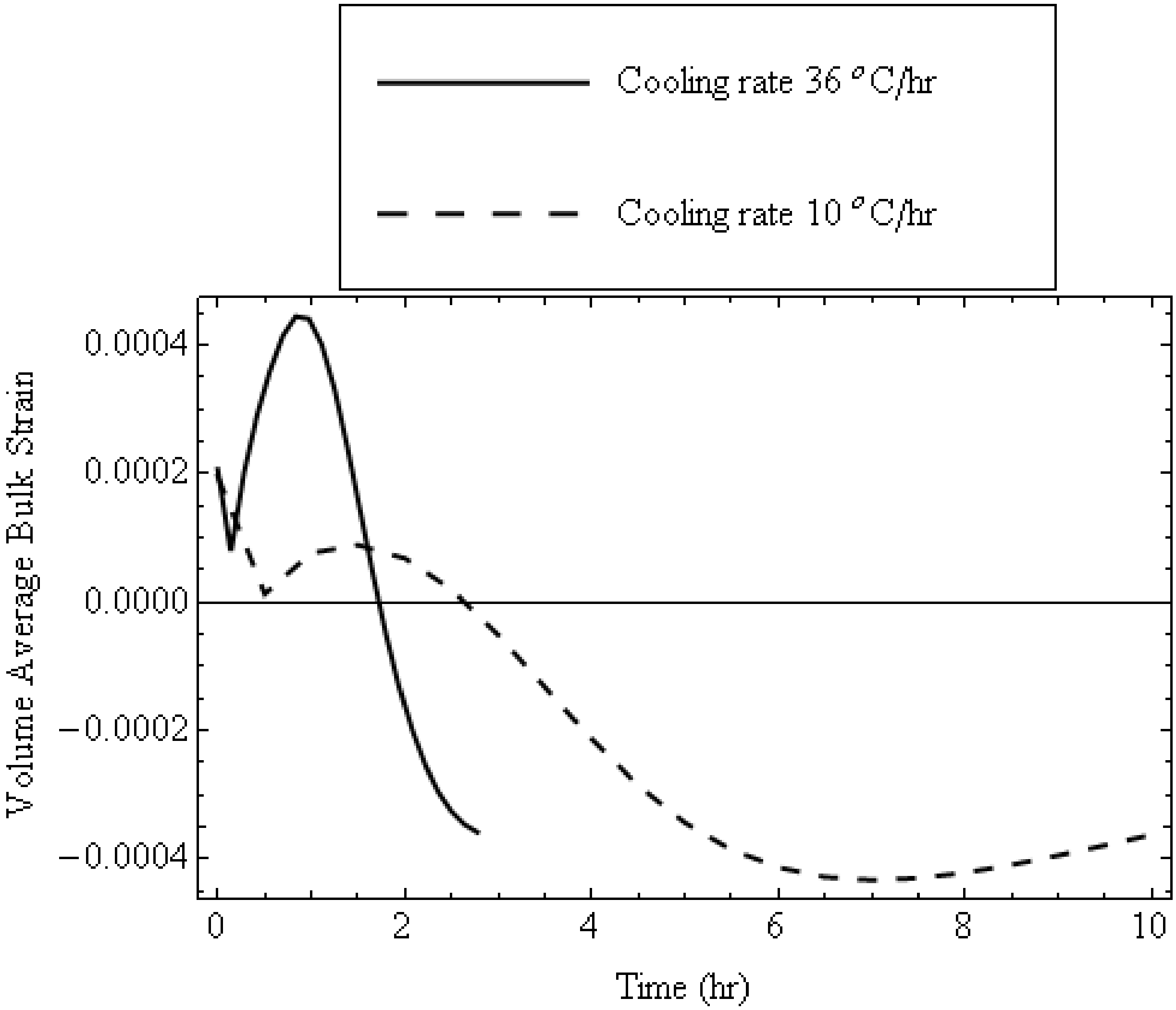

Figure 46. Effect of cooling rate on the bulk strain of concrete cooled to -100 ºC. The higher the cooling rate, the higher the swelling.

5 EXPERIMENTS

The purpose of this section is to evaluate the proposed model using acoustic emission (AE) technology. Several researchers have used AE technology to detect cracking and deterioration of concrete subjected to various stimuli [50–52]. When cracking occurs, rapid release of energy produces elastic waves that travel in all directions. Appropriate sensors can detect these waves, and damage caused can be further analyzed by quantifying the energy as the absolute area under the wave form. In this section, two concrete beams are tested for freeze-thaw cycles according to the American Society for Testing and Materials (ASTM) C666 [53], and the resulting damage is monitored by quantifying AE energy.

5.1 Materials and Experimental Quantification

Two concrete beams of 7.62 cm × 10.16 cm × 40.64 cm (3 inch × 4 inch × 16 inch) are exposed to more than 300 cycles of freeze-thaw in an environmental simulation chamber. Each cycle is 4 hours long with temperatures varying from 4.4 °C to -17.8 °C, as shown in Figure 47. A steel bar is placed at the center of the specimen to reach the target temperature quickly. A thermocouple is attached to the center of the specimen to monitor the temperature at the center. Shimada et al. [50] found that the surface water affects the AE measurement of mortar, and it is not directly related to the frost damage of mortar. Thus, the specimens are surrounded by water on all sides but not the top surface during both the freezing and thawing period. The temperature at the center of the specimen is measured by a thermocouple. Both the specimens are made of the same material with the same proportions listed in **Error! Reference source not found.**. Half of the limestone aggregate is 0.953 cm (3/8 inch) – 1.27 cm (1/2 inch), and the other half is 1.27 cm (1/2 inch) – 1.91 cm (3/4 inch). The absorption capacity (AC) of the oven-dried coarse aggregate is measured to be 3.318%.

The AE system used for this research is a Vallen model AMSY6 [54]. Each specimen is attached to a 75 KHz piezoelectric sensor to record acoustic emission activity generated by crack formation. The sensor is attached to the top surface of the specimen with a vacuum grease coupling agent. Additionally, an elastic band is used to apply the minimum pressure necessary for a good contact with the specimen surface and to hold it firmly in place. Each sensor is connected to a 34 dB preamplifier. The output from the preamplifier is then fed to the AE signal processor to extract feature data. A threshold value of 55 dB was used in a previous study for mortars subjected to freeze-thaw cycles [50]. However, micro-cracks that initiate in the ITZ can have a value between 40-60 dB [51], so in order to select an optimum threshold value that will filter out the environmental noise without excluding the micro-cracks, a sensor is placed in the chamber to monitor the noise, and a single freeze-thaw cycle is run. A threshold value of 50 dB is determined to be the suitable value for this experimental setup.

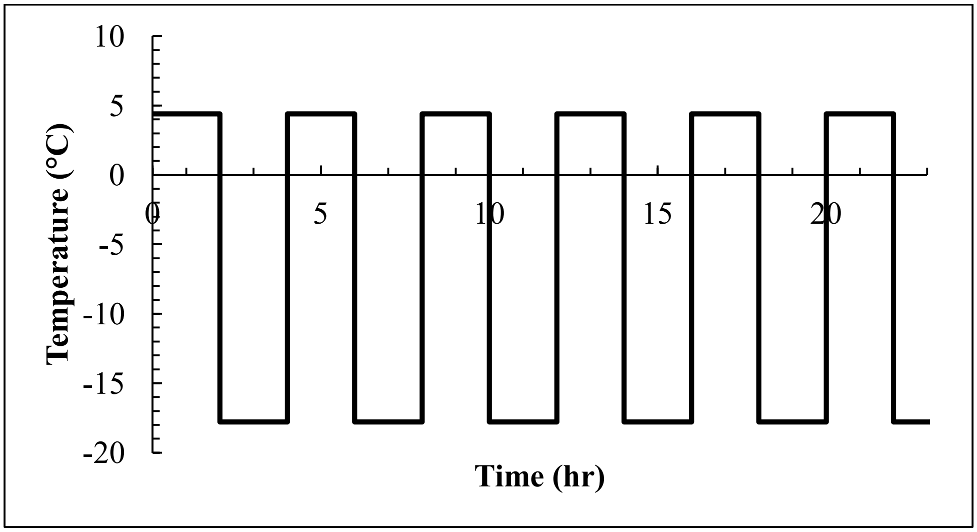

Figure 47. Temperature history for the applied freeze-thaw cycles.

Table 1. Mixture proportion and material properties.

Material	Bulk-Specific Gravity	Absorption Capacity (%)	Weights (kg per m^3 of concrete)
Cement	3.15	N/A	356.8
Water	1	N/A	172.9
Limestone	2.61	3.318	864.4
Sand	2.59	0.65	886.7
Air	6%		

5.2 Measuring Needed Inputs

In order to verify the model, material properties obtained for the above concrete mixture are used. Volume fraction of the coarse aggregate is found to be about 35%. The capillary porosity of the mortar matrix, bulk modulus of the matrix, K^p , is calculated from the w/c using the following equation [23]:

$$\phi_o^p = \frac{\frac{w}{c} - 0.36\theta}{\frac{w}{c} + 0.32} \qquad (0)$$

where θ is the degree of hydration that can vary from 0 for fresh concrete to 1 for complete hydration. Assuming 100% of the hydration is completed prior to testing, we get $\theta = 1$. For a w/c of 0.5 used in the mixture proportion, ϕ_o^p is calculated to be around 0.17. Bulk modulus for mortar matrix, K_s^p , is calculated from the elastic modulus, E^p , and Poisson's ratio, ν^p . E^p and ν^p are assumed to be $16'\ 10^3$ MPa and 0.2, respectively. K^p is then determined using the relation $K^p = E^p / 3(1-\ 2n^p)$. Using (0), K_s^p is calculated to be 13.9×10^3 MPa. The bulk-specific gravity of the saturated surface dry limestone is 2.61, and the AC of the oven-dry sample is 3.318% (**Error! Reference source not found.**). Porosity of aggregate is calculated in terms of AC using the following formula, and assuming specific gravity of water equals 1:

$$f_o^a = \frac{\text{\% Mass of water in pore}}{100} = \frac{AC}{100} = \frac{W_{SSD} -\ W_{OD}}{W_{OD}} = 0.033$$

A permeability of 1×10^{-21} m^2 is adopted for both the aggregate and matrix. Approximate values of α of 6×10^{-6}°C^{-1} [23] and 8×10^{-6}°C^{-1} [41] are used for the coarse aggregate and mortar matrix, respectively. Bulk modulus of aggregate is assumed as 40×10^3 MPa. Also, a single-step cooling to -25 ºC is used.

6 RESULTS

Yang et al. [51] correlated the AE signal energy distribution to different damage mechanisms. They classified AE signals into four typical types and correlated them to different damage sources and mechanisms:

- Type I signal has a short duration (< 200 μs) and low to medium amplitude (40–60 dB) with a peak frequency at approximately 350 kHz.
- Type II signal is similar to a Type I signal; however, it has a medium to long duration (400–600 μs).
- Type III signal has a peak frequency of 100 kHz and a long duration (> 2000 μs).
- Type IV signal has a high amplitude (> 70 dB) and long duration with a peak frequency at approximately 100 kHz.

Type I and Type II signals are associated with the paste cracking (microcrack initiation and microcrack propagation, respectively), Type III with de-bonding, and Type IV with physical failure of aggregates [51]. Therefore, AE data are analyzed in Section 6.1 to quantify damage and to determine possible damage sources caused during the freeze-thaw testing. In Section 6.2, these results are then verified using the proposed model.

6.1 Measured Damage

In order to ensure that all noise is excluded, AE data are filtered in two steps. All data with amplitude lower than 60 dB are excluded first. Although AE signals of this type (Type I and Type II) can be attributed to microcrack initiation and propagation occurred in the matrix, our primary concern is to detect D-cracking (Type IV signals) caused by the destructive aggregates. This is done using the VisualAE software. After that, Mathematica is used to further filter the data. Since both the specimens are tested together, and it is unlikely for both of them to have cracks form at the exact same time, simultaneous AE events detected by the two sensors are eliminated and assumed to be caused by the noise emitted from the environment. Filtered AE data are then analyzed to measure damage caused by the freeze-thaw cycles. Figure 48 shows AE events for the first six cycles detected by Sensor 1. A high number of AE events with high amplitudes (> 70 dB) tend to occur at the beginning of the freezing cycles, followed by very few events during the rest of the freezing period. This indicates that the Type V signals, which are associated with the physical deterioration of aggregates, are more likely to occur during freezing.

This is confirmed at the end of the experiment when concrete pieces come apart from the specimen with broken aggregate parts. The peak amplitude is measured to be 99.9 dB. Also, a substantial amount of AE events with low amplitudes (< 70 dB) is observed during both the freezing and thawing periods. These signals might have been produced by the microcrack initiation (Type I) or propagation (Type II) through the matrix.

Figure 49 provides the cumulative AE energy for both sensors. This energy is calculated in Joule (J) as true energy by integrating the square of the recorded signal voltage over time. According to Figure 49, both the curves exhibit gradually decreasing slopes, which shows that the damage evolution rate decreases with increasing cycle. However, at around t = 2.5 days, t = 6 days, and t = 11 days, the lines exhibit steep slope, revealing that very high AE energy is released, which also shows that extensive damage occurs at that time. As a result, much higher energy is released over the first 20 days, which is about twice that released during the next 30 days.

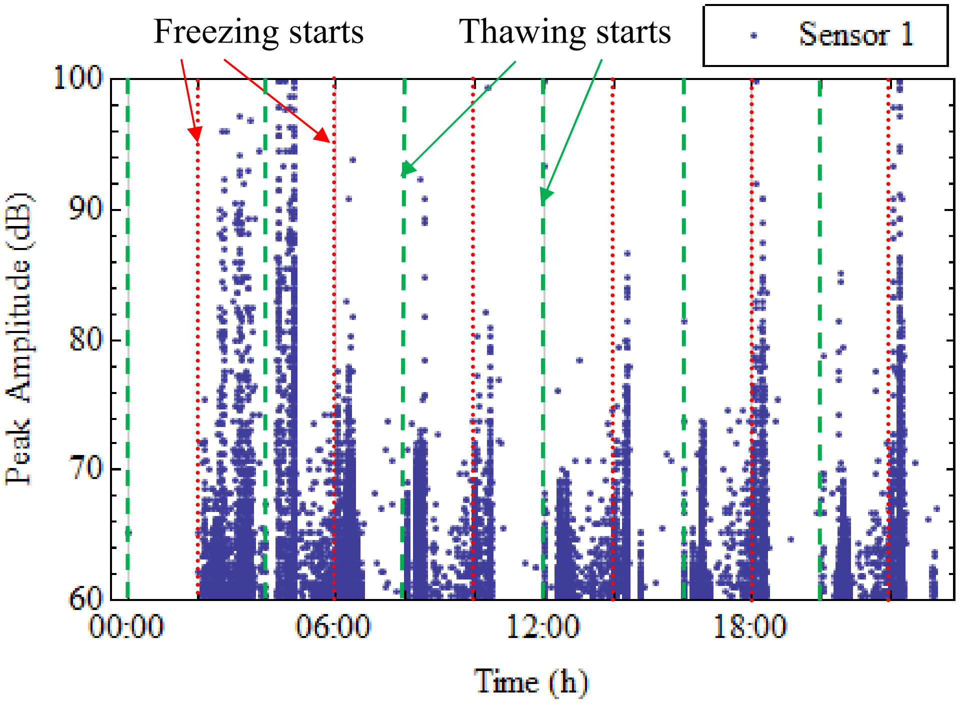

Figure 48. AE signal occurrence with freeze-thaw cycles.

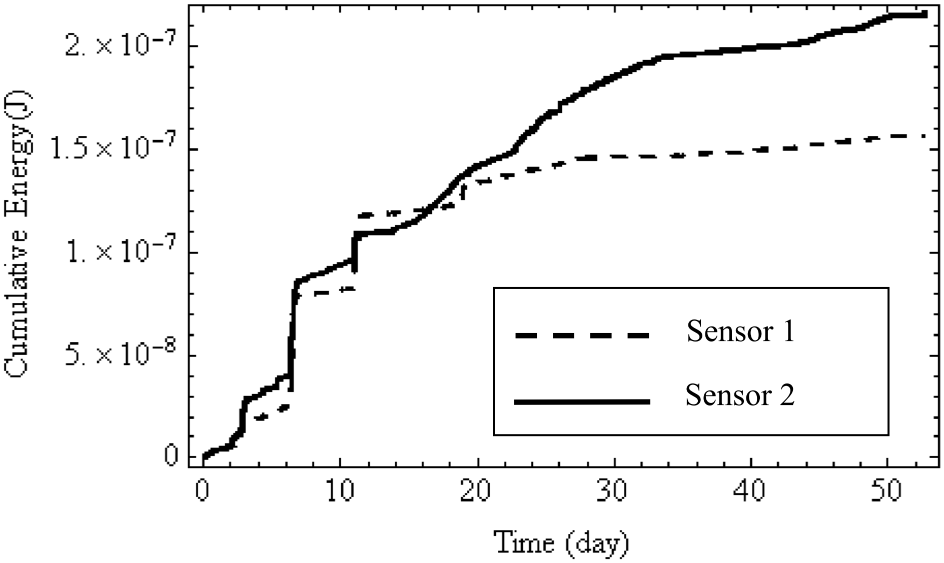

Figure 49. Cumulative AE energy generated by damage in concrete associated with the freeze-thaw cycles. Sensor 1 and 2 represent two different specimens in the same environment.

6.2 Predicted Damage

Material properties measured in Section 5.2 are fitted in the proposed model. Since the specimens contain 6% air void, they are modeled as air-entrained concrete, and resulting plots are provided in Figure 51, Figure 52, and Figure 52. As shown in Figure 50, high pore liquid pressure of around 85 MPa is initially obtained at the center of the aggregate. This high pore pressure eventually depressurizes in time to a stable value of about -29 MPa governed by the solid-liquid thermodynamic equilibrium. Bulk strain distribution is shown in Figure 51. Since the matrix is treated as air entrained, and the air bubbles act as expansion reservoirs and cryo-pumps, a uniform contraction of about -0.001 occurs in the paste caused by the thermal contraction and depressurization of the pore water. The aggregate, on the other hand, contracts less than the mortar matrix due to the presence of ice crystals. Due to this strain gradient, as shown in Figure 52, the mortar matrix exhibits tensile tangential stress with a peak value of about 3.7 MPa at the ITZ. It is this tensile stress that creates cracks at the ITZ. Such cracks may alter the stress path, and cracks can propagate through the aggregate with successive freeze-thaw cycles, which supports the experimental results obtained in the previous section (Section 6.1). The proposed poroelastic model may over-predict the stress in the matrix, which in real life acts as a viscoelastic material and exhibits stress relaxation. This high stress implies that even air-entrained concrete may suffer D-cracking if unwanted materials are used. An appropriate combination of material geometry and constitutive properties may prevent this damage.

High tensile stress in the matrix can be reduced by increasing the bulk modulus of the matrix and using high-porosity, high-permeability (lightweight) aggregates. This is shown in Figure 53, Figure 54, and Figure 55, where the bulk modulus of the matrix is considered to be 45×10^3 MPa instead of 13.9×10^3 MPa. Also, an aggregate with high porosity (ϕ_o^a= 0.2) and high permeability ($k^a = 10^{-15}$) is used in this case. It is seen that due to high permeability, pore pressure in the aggregate reaches the equilibrium much faster than in the low permeability aggregate. Moreover, use of a high-porosity aggregate and stiff matrix reduces the strain differential (Figure 54), which also reduces the tangential stress (Figure 55) significantly. The peak stress (about 0.15 MPa) in this case is generated in the aggregate, which makes the concrete less susceptible to damage since the aggregate has a very high tensile strength (about 10 MPa [32]) compared to the ITZ (about 0.5 MPa [32]). Therefore, a high-porosity, high-permeability aggregate along with stiff matrix can help improve the air-entrained concrete durability.

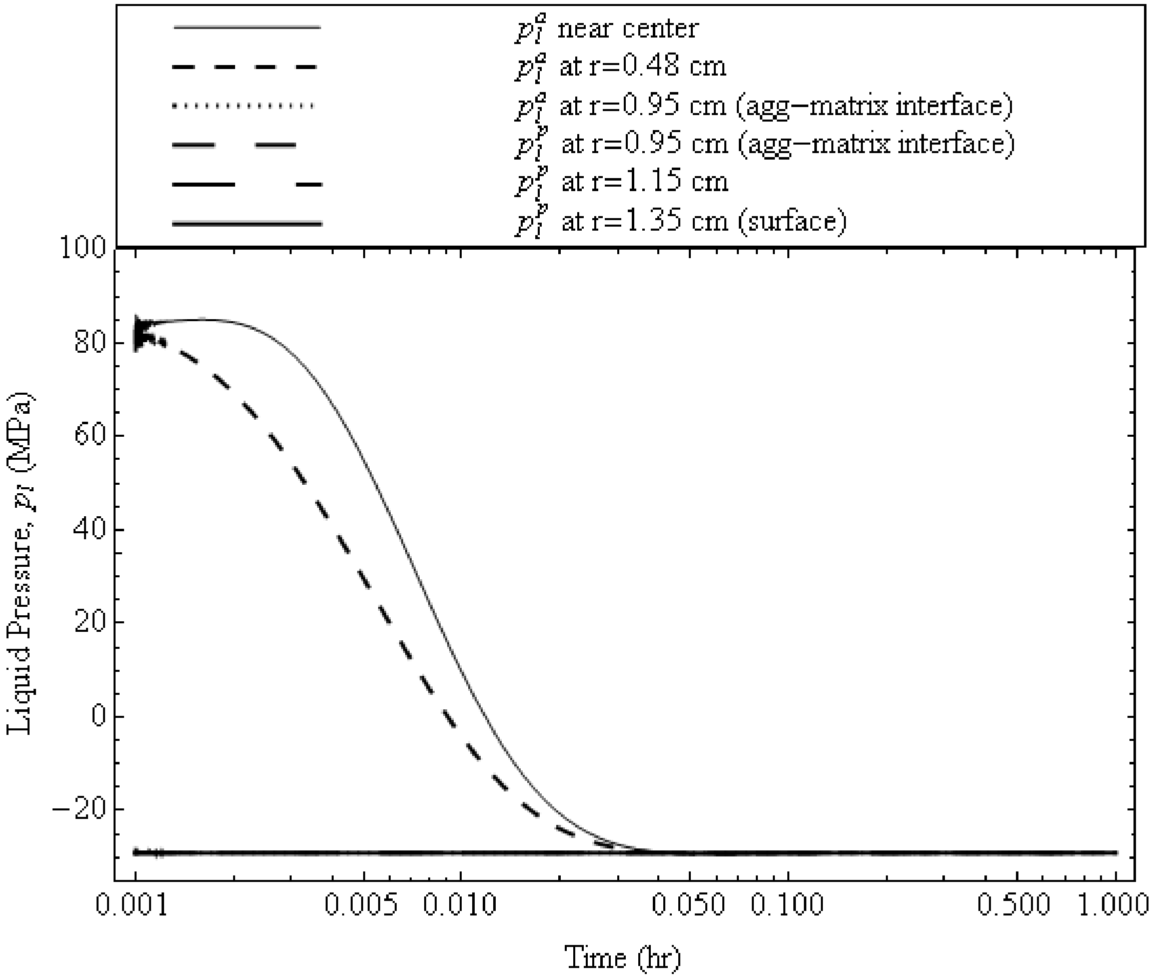

Figure 50. Predicted pore pressure distribution for the specimen used for AE measurement. A uniform suction of about -29 MPa is generated in the sphere required by the solid-liquid thermodynamic equilibrium.

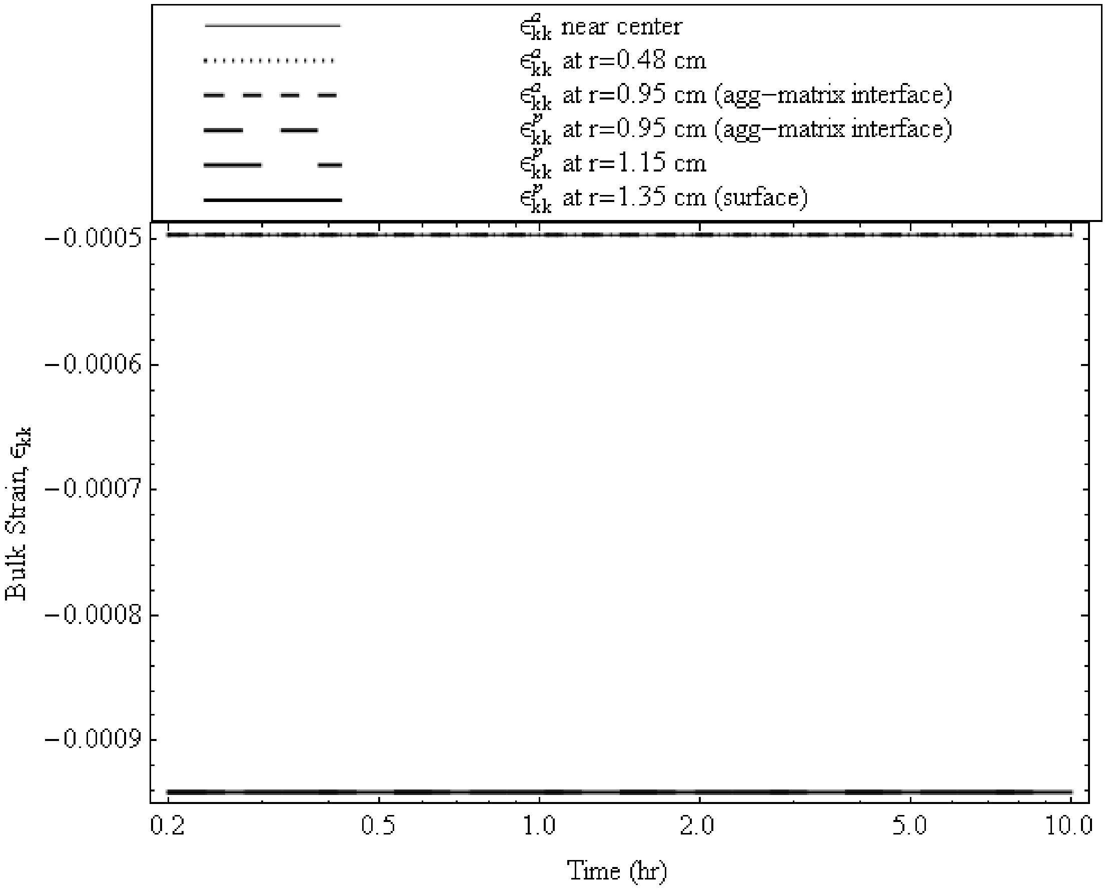

Figure 51. Predicted strain differential. The matrix exhibits uniform contraction caused by the thermal deformation and the pore water depressurization. The aggregate contracts less than the matrix because of the presence of the ice crystals.

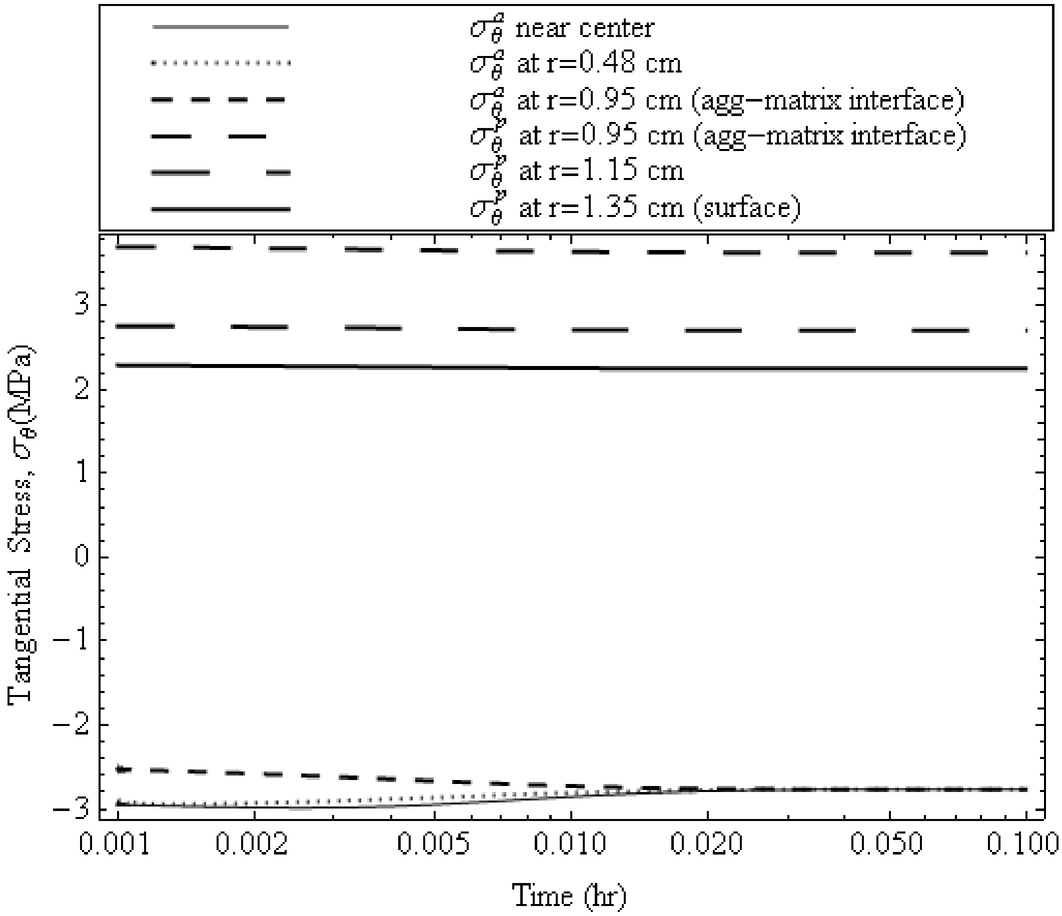

Figure 52. Predicted stress distribution. Peak stress occurs at the ITZ due to the sudden strain differential at the aggregate-matrix interface.

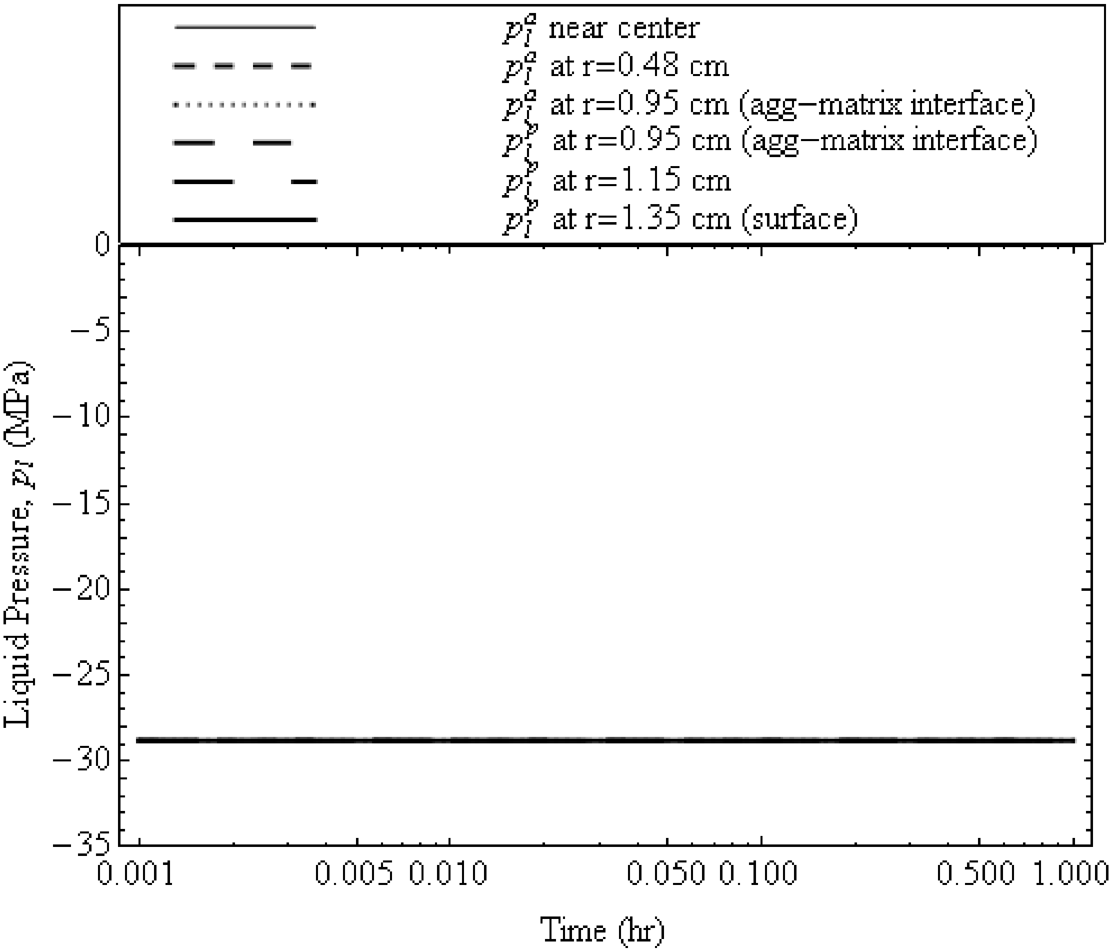

Figure 53. Pore pressure in the high-porosity, high-permeability aggregate quickly reaches equilibrium.

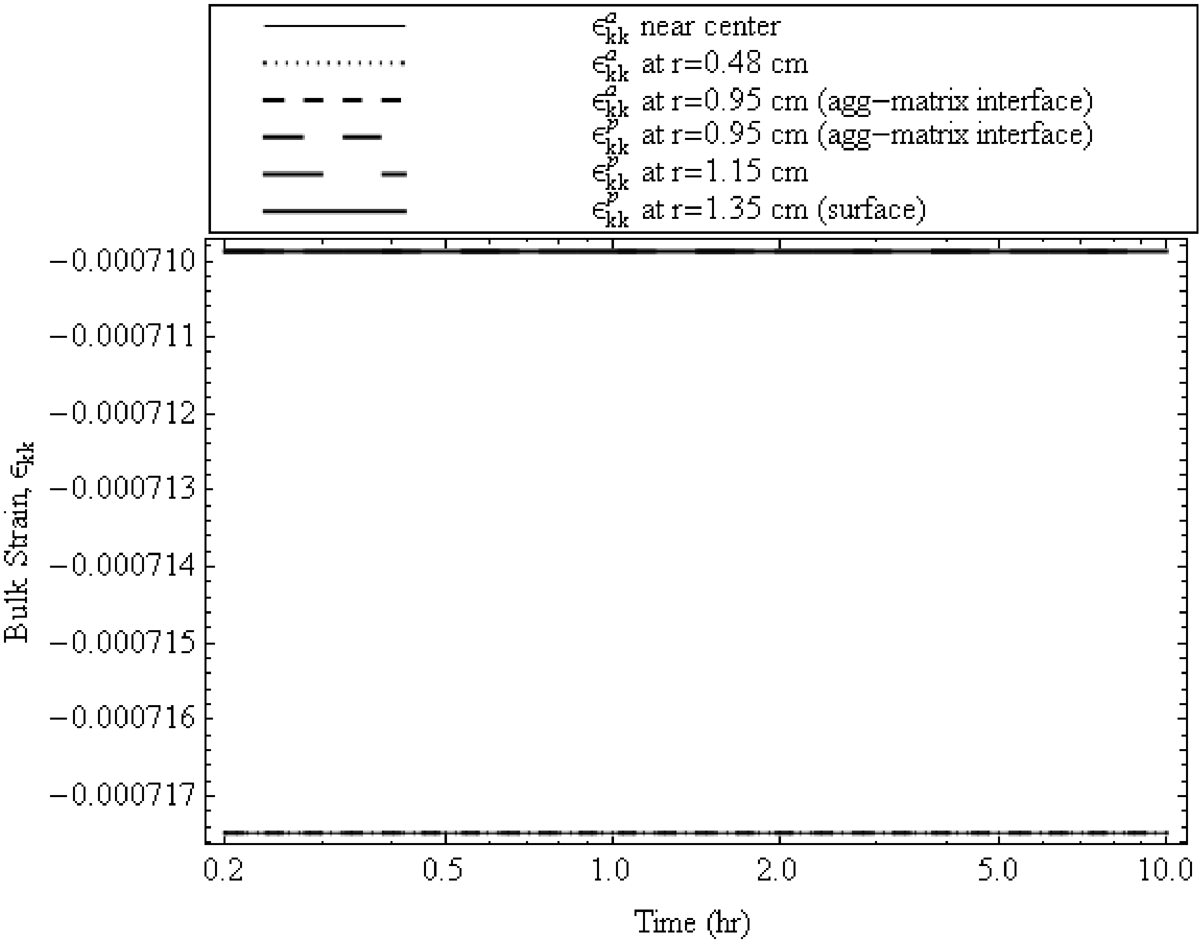

Figure 54. High-porosity, high-permeability aggregate with stiff matrix reduces the strain differential substantially.

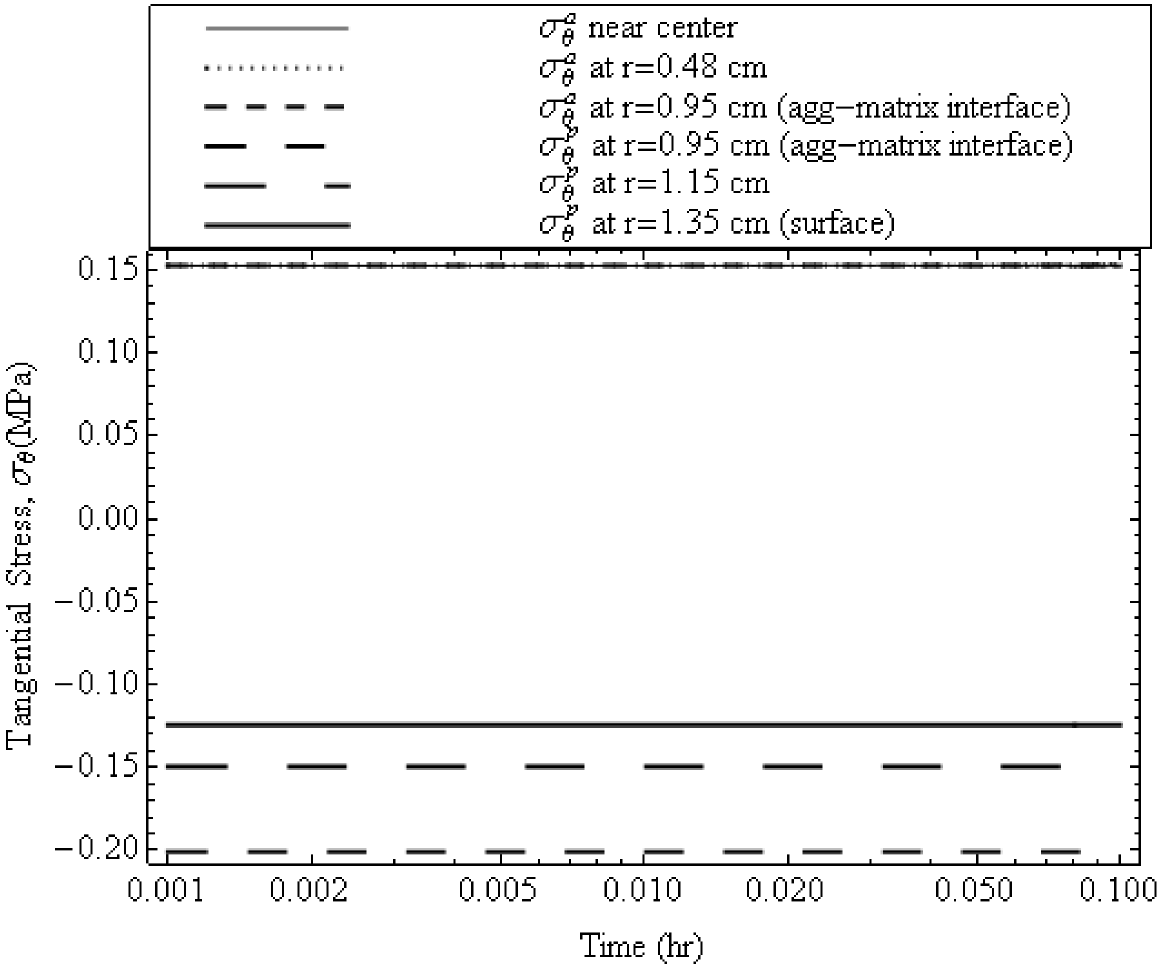

Figure 55. A very low tensile tangential stress is developed in the aggregate, which indicates that a high-porosity, high-permeability aggregate embedded in a stiff matrix is much more durable than a low-porosity, low-permeability aggregate with a relatively less stiff matrix.

7 CONCLUSIONS AND RECOMMENDATIONS

A poroelastic model was developed that can predict stress and strain distributions (and thus ostensibly damage likelihood) in concrete under freezing conditions caused by aggregates with undesirable combinations of geometry and constitutive properties. The model was evaluated through the AE analysis under freeze-thaw cyclic loading. The most important findings of this research are summarized below:

- Experimental results show that cracking with high amplitude (> 70 dB) occurs near the beginning of freezing cycles, which is associated with the physical deterioration of the aggregate, whereas AE signals with low amplitude (< 70 dB) characterizing microcracking (microcrack initiation and propagation) in the mortar matrix were observed throughout the test. This supports the modeling results, which show that high tensile tangential stress develops at the ITZ and may alter the stress path, and as a result, cracks may propagate through the aggregate with the successive freeze-thaw cycles.
- Experimental results also support the fact that air-entrained concrete may undergo D-cracking if deleterious materials are used. It was found that low-porosity, low-permeability aggregates embedded in a relatively less stiff matrix may create high tangential tensile stress in the ITZ.
- It was predicted that high-porosity, high-permeability (e.g. lightweight) aggregates and stiff matrix are beneficial for improving the freeze-thaw resistance of the air-entrained concrete.
- High-porosity, low-permeability aggregates with fine pore structure are the most vulnerable to D-cracking in non-air-entrained concrete. The destructive tensile stress according to this model is generated at the aggregate boundary by the Mandel-Cryer effect. This Mandel-Cryer effect is induced by the strain differential caused by the expansive aggregate center.
- It was found that the low-porosity, high-permeability aggregates relax the pore liquid pressure rapidly and are least susceptible to D-cracking for the non-air-entrained concrete.

- Although high-permeability aggregates were found to be sound against D-cracking, a large particle diameter makes them susceptible to cracking at the matrix outmost boundary.
- Reduction in aggregate size was found to be effective in quickly relaxing the tensile tangential stress, which eventually helps mitigate D-cracking of concrete under freezing temperatures.
- Although permeability and aggregate size greatly affect the pore pressure relaxation time, they do not have an effect on the magnitude of the peak pore pressure in the concrete under a step change in temperature.
- Difference between CTEs of coarse aggregate and matrix in which they are embedded should not be too high since it may cause tensile stress at the aggregate boundary or ITZ. Higher CTE of the high-porosity, low-permeability aggregate may exacerbate D-cracking by substantially increasing the delayed tensile tangential stress at the aggregate boundary induced by the Mandel-Cryer effect.
- A high-porosity, low-permeability matrix with fine pore structure may deteriorate concrete resistance to D-cracking and increase the strain differential and the resulting tangential stress at the aggregate-matrix boundary. An analogous response can be found if the bulk modulus of the matrix is reduced. Therefore, low w/c and addition of pozzolans help increase the bulk modulus, reduce the porosity of the porous body, and improve durability.
- Increase in cooling rate decreases concrete durability under freezing temperatures through the reduction in time available to relax pore pressure buildup and the related tangential stresses in the aggregate and matrix.

Some limitations of the model developed in this work include:

- This model is a poroelastic model and may over-predict the stress since it does not account for the viscoelastic stress relaxation.
- This model does not include the dependence of saturation on pore pressure, which otherwise would have made the solution of pore pressure highly complicated.
- Presence of dissolved species in the pore fluid is neglected. Thus, the model does not predict the effect of road salts on D-cracking.

- There may be entrapped air pockets inside the concrete in the field, which causes ice crystallization even at a temperature right below the melting point. High crystallization pressure will occur in such cases, generating huge expansion. It was beyond the scope of this project to include such phenomenon.
- Degradation of material properties with damage and time are neglected to avoid complications in the solutions.
- No interaction between aggregate particle stress/strain fields are considered.

On the basis of the limitations summarized above, some recommendations are provided here for future research:

- Over-prediction of the results can be effectively handled by incorporating viscoelasticity that accounts for stress relaxation.
- The geometric model can be further improved by treating ITZ separately from matrix shell as a different band of material. This is still possible within the framework of the proposed model.
- This model should be further developed to include pore pressure dependence of saturation. Finite element modeling in that case may prove beneficial.
- Time dependence of permeability, density, viscosity, and CTE can be included.
- Degradation of material properties, such as bulk modulus and permeability, due to damage growth can be included in this model using the concept of damage mechanics.
- The modeling approach presented herein can be utilized to predict damage caused by the expansion of the alkali-silica hydrate gel during ASR reaction and degradation. This can be done in two ways: the gel can be treated as a separate ring of material in between the matrix shell and the aggregate core, or it can be treated as an integrated part of the expansive aggregate core that develops tensile tangential stress in the matrix.
- Damage due to expansion of aggregates rarely occurs after one loading cycle, where loading cycle refers to a single freeze event or single imbibition of water by ASR gel. For the freeze-thaw case, many freeze-thaw cycles are generally necessary to develop visible damage. Likewise, current research at TTI [55] has indicated that more severe damage occurs when ASR-affected concrete is subjected to moisture cycling rather

than a sustained source of moisture. Therefore, this model can be further developed by incorporating an appropriate fatigue-based damage model for both D-cracking and ASR problems.

In conclusion, the proposed model uses material properties that are directly used in the concrete mixture design procedure and successfully predicts pore pressure, stresses, and strains generated within the structure that may occur in the field. It is expected that incorporation of this theory into the mixture design process will help with selecting appropriate materials, which in turn will improve the durability of concrete infrastructure.

REFERENCES

[1] "States Reap Substantial Savings while Building More Durable Concrete Bridges and Pavements," *Focus*. [Online]. Available: http://www.fhwa.dot.gov/publications/focus/97mar/index.cfm. [Accessed: 2011].

[2] M. A. Biot, "Theory of Propagation of Elastic Waves in a Fluid-Saturated Porous Solid. I. Low-Frequency Range," *Journal of the Acoustical Society of America*, vol. 28, no. 2, pp. 168-178, 1956.

[3] O. Coussy, *Poromechanics*. West Sussex, England: John Wily & Sons, Ltd, 2004.

[4] B. Zuber and J. Marchand, "Predicting the Volume Instability of Hydrated Cement Systems upon Freezing Using Poro-Mechanics and Local Phase Equilibria," *Materials and Structures*, vol. 37, no. 4, pp. 257-270, May 2004.

[5] O. Coussy, "Poromechanics of Freezing Materials," *Journal of the Mechanics and Physics of Solids*, vol. 53, no. 8, pp. 1689-1718, Aug. 2005.

[6] O. Coussy and P. Monteiro, "Unsaturated Poroelasticity for Crystallization in Pores," *Computers and Geotechnics*, vol. 34, no. 4, pp. 279-290, Jul. 2007.

[7] O. Coussy and P. Monteiro, "Poroelastic Model for Concrete Exposed to Freezing Temperatures," *Cement and Concrete Research*, vol. 38, no. 1, pp. 40-48, Jan. 2008.

[8] F. Bangert, D. Kuhl, and G. Meschke, "Chemo-Hygro-Mechanical Modelling and Numerical Simulation of Concrete Deterioration Caused by Alkali-Silica Reaction," *International Journal for Numerical and Analytical Methods in Geomechanics*, vol. 28, no. 7-8, pp. 689-714, 2004.

[9] J. O'Doherty, "D-Cracking of Concrete Pavements," Materials and Technology Division of the Michigan Department of Transportation, 1987.

[10] A. Koubaa, M. B. Snyder, and K. R. Peterson, "Mitigating Concrete Aggregate Problems in Minnesota," Minnesota Department of Transportation Research Services, St. Paul, 2004.

[11] Amir N. Hanna, "Aggregate Tests for Portland Cement Concrete Pavements□: Review and Recommendations," *Research Results Digest*, no. 281, 2003.

[12] T. C. Powers, "The Air Requirement of Frost Resistant Concrete," in *Proceedings of Highway Research Board*, 1949, pp. 184-221.

[13] T. C. Powers and R. A. Helmuth, "Theory of Volume Changes in Hardened Portland-Cement Paste during Freezing," in *Proceedings of Highway Research Board*, 1953, pp. 285-297.

[14] G. W. Scherer and J. J. Valenza, “Mechanisms of Frost Damage,” *Materials Science of Concrete*, vol. 7, pp. 209-246, 2005.

[15] J. J. Beaudoin and C. MacInnis, “The Mechanism of Frost Damage in Hardened Cement Paste,” *Cement and Concrete Research*, vol. 4, pp. 139-147, 1974.

[16] V. Pentalla, “Freezing-Induced Strains and Pressures in Wet Porous Materials and Especially in Concrete Mortar,” *Advanced Cement Based Materials*, vol. 7, no. 1, pp. 8-19, 1998.

[17] S. Timoshenko and J. N. Goodier, *Theory of Elasticity*. New York: McGraw-Hill, 1951, pp. 416-420.

[18] “Wolfram Mathematica 8.” Wolfram Research, Inc., 100 Trade Center Drive, Champaign, IL, 61820-7237, USA.

[19] O. Coussy and P. J. M. Monteiro, “Errata to ‘Poroelastic Model for Concrete Exposed to Freezing Temperatures’ [Cement and Concrete Research 38 (2008) 40–48],” *Cement and Concrete Research*, vol. 39, no. 4, pp. 371-372, Apr. 2009.

[20] H. F. Wang, *Theory of Linear Poroelasticity with Applications to Geomechanics and Hydrogeology*. Princeton, NJ: Princeton University Press, 2000, pp. 38, 195,196.

[21] H. Stehfest, “Numerical Inversion of Lapalce Transforms,” *Communications of the ACM*, vol. 13, pp. 47-49 and 624, 1970.

[22] A. Mallet, “Numerical Inversion of Laplace Transform.” Wolfram Research, Inc., 2000.

[23] S. Mindess, J. F. Young, and D. Darwin, *Concrete*. New Jersey: Pearson Education, Inc, 2003, pp. 4, 233, 460.

[24] W. Vichit-Vadakan and G. W. Scherer, “Measuring Permeability of Rigid Materials by a Beam-Bending Method: III, Cement Paste,” *Journal of the American Ceramic Society*, vol. 85, no. 6, pp. 1537-1544, Jun. 2002.

[25] Z. C. Grasley and C. Leung, “Quasi-Static Axial Damping of Poroviscoelastic Cylinders,” *Journal of Engineering Mechanics*, vol. 137, no. 8, pp. 561-570, 2011.

[26] M. Chaplin, “Water Structure and Science,” 2011. [Online]. Available: http://www.lsbu.ac.uk/water/anmlies.html. [Accessed: Mar-2012].

[27] G. Verbeck and R. Landgren, “Influence of Physical Characteristics of Aggregates on Frost Resistance of Concrete,” 1960, vol. 60, pp. 1063-1079.

[28] S. R. Thompson, M. P. J. Olsen, and B. J. Dempsey, “D-cracking in Portland Cement Concrete Pavements,” State of Illinois Department of Transportation, Urbana, 1980.

[29] D. Stark and P. Klieger, "Effect of Maximum Size of Coarse Aggregate on D-Cracking in Concrete Pavements," *Highway Research Record No. 441*, pp. 33-43, 1973.

[30] D. Stark, "Characteristics and Utilization of Coarse Aggregates Associated with D-Cracking," *Society*, 1976.

[31] D. J. Janssen and M. B. Snyder, *Resistance of Concrete to Freezing and Thawing*. Washington, DC: SHRP-C-391, National Research Council, 1994.

[32] M. Alexander and S. Mindess, *Aggregates in Concrete*. New York: Taylor & Francis, 2005, pp. 256, 284-287.

[33] P. K. Mehta and P. J. M. Monteiro, *Concrete: Microstructure, Properties, and Materials*. McGraw-Hill Companies, 2005, pp. 127, 128.

[34] Z. C. Grasley, G. W. Scherer, D. A. Lange, and J. J. Valenza, "Dynamic Pressurization Method for Measuring Permeability and Modulus: II. Cementitious Materials," *Materials and Structures*, vol. 40, no. 7, pp. 711-721, Nov. 2006.

[35] T. C. Powers, "Structure and Physical Properties of Hardened Portland Cement Paste," *Journal of the American Ceramic Society*, vol. 41, no. 1, pp. 1-6, 1958.

[36] M. Kaneuji, "Correlation between Pore Size Distribution and Freeze Thaw Durability of Coarse Aggregate in Concrete: Interim Report," West Lafayette, Indiana, 1978.

[37] J. L. Clarke, *Structural Lightweight Aggregate Concrete*. Glasgow, NZ: Blackie Academic & Professional, an imprint of Chapman & Hall, 1993, p. 19.

[38] A. M. Neville and J. J. Brooks, *Concrete Technology*, 2nd ed. Essex, England: Pearson Education Limited, 2010.

[39] N. M. Vanderhorst and D. J. Janssen, "The Freezing and Thawing Environment: What is Severe?" in *Proceedings of Paul Klieger Symposium, ACI SP 122*, 1990, pp. 181-200.

[40] Z. C. Grasley and D. A. Lange, "Thermal Dilation and Internal Relative Humidity of Hardened Cement Paste," *Materials and Structures*, vol. 40, no. 3, pp. 311-317, Aug. 2006.

[41] C. R. Cruz and M. Gilien, "Thermal Expansion of Portland Cement Paste, Mortar and Concrete at High Temperatures," *Fire and Materials*, vol. 4, no. 2, pp. 66-70, 1980.

[42] E. J. Callan, "Thermal Expansion of Aggregates and Concrete Durability," *Journal of the American Concrete Institute Proceedings*, vol. 48, no. 2, pp. 485-504, 1952.

[43] J. K. Su, S. W. Cho, C. C. Yang, and R. Huang, "Effect of Sand Ratio on the Elastic Modulus of Self-Compacting Concrete," *Journal of Marine Science and Technology*, vol. 10, no. 1, pp. 8-13, 2002.

[44] B. J. Christensen, T. O. Mason, and H. M. Jennings, "Comparison of Measured and Calculated Permeabilities for Hardened Cement Pastes," *Cement and Concrete Composites*, vol. 26, no. 9, pp. 1325-1334, 1996.

[45] Z. Sun, "Mechanism of Frost Damage to Concrete," Princeton University, 2010.

[46] H. S. Wong, R. W. Zimmerman, and N. R. Buenfeld, "Estimating the Permeability of Cement Pastes and Mortars Using Image Analysis and Effective Medium Theory," *Cement and Concrete Research*, vol. 42, no. 2, pp. 476-483, Dec. 2011.

[47] G. Tognon, "Behaviour of Mortars and Concrete in the Temperature Range from +20 ^{o}C to -196 ^{o}C," in *Fifth International Symposium on the Chemistry of Cement*, 1968, pp. 229-249.

[48] Z. Liu, W. Hansen, C. Borgnakke, and Y. Kang, "Cryogenic Suction-A Major Salt Scaling Mechanism in Highway Concrete," in *Tenth International Conference on Concrete Pavements*, 2012.

[49] M. Pigeon, J. Prevost, and J. Simard, "Freeze-Thaw Durability Versus Freezing Rate," *ACI Materials Journal*, pp. 684-692, 1985.

[50] H. Shimada, K. Sakai, and G. G. Litvan, "Acoustic Emission of Mortar Subjected to Freezing and Thawing," *Durability of Concrete*, vol. 1 & 2, pp. 263-278, 1991.

[51] Z. Yang, J. Weiss, and J. Olek, "Using Acoustic Emission for the Detection of Damage Caused by Tensile Loading and Its Impact on the Freeze-Thaw Resistance of Concrete," in *International Conference on Construction Materials*, 2005, no. 765.

[52] S. Puri and J. Weiss, "Assessment of Localized Damage in Concrete under Compression Using Acoustic Emission," *Journal of Materials in Civil Engineering*, vol. 18, no. 3, pp. 325-333, 2006.

[53] ASTM C 666-97, "Standard Test Method for Resistance of Concrete to Rapid Freezing and Thawing," ASTM Committee C-9, 1997.

[54] "Vallen AMSY6." Vallen Systeme GmbH Schaeftlarner Weg 26 82057, Icking, Germany.

[55] "Cracking under Pressure: How Moisture and Heat Affect ASR and DEF Structures," *TTI Researcher*, 2010.

APPENDIX

The Mathematica code containing the elastic and poroelastic formulation along with the material constants and coefficients is given here.

Load Modules

The following commands set the present directory as the work directory, and load the required files.

```
thisDir = ToFileName[
   ("FileName" /. NotebookInformation[EvaluationNotebook[]]) [[1]]];
SetDirectory[thisDir];
<< NumericalInversion.m;
<< NLapInv.m;
Needs["PlotLegends`"];
```

Elastic Behavior (Time Domain)

An elastic model was first developed based on the classical elastic theory proposed by Timoshenko and Goodier [16]. This section deals with the determination of the integration constants, and stress strain responses of the elastic concrete sphere.

Integration Constants

Integration constants for the elastic response of the concrete sphere containing the coarse aggregate core surrounded by the mortar or cement matrix shell are determined in this section. Coefficients βa, βp, τa, τp, χa, χp, Xx, Uu, Vv, Ww, and Zz are used to simplify the equations.

The following equations set the radial deformation of the aggregate equal to that of the matrix at the aggregate-matrix interface.

```
            /1 + νa  Ri                       \
uraggint =  |------- -- εfaggave + Clagg * Ri | //.  {(1 + νa) / (1 - νa) → 3 βa};
            \1 - νa  3                        /

                                 C2paste
urpasteint = C1paste * Ri + -------;
                                   Ri²

BC1 = uraggint == urpasteint;
```

The equations below set the radial stress of the aggregate equal to that of the matrix at the aggregate-matrix interface.

```
             /   1 - 2 νa                               \
σraggint = | - -------- 2 Ka εfaggave + 3 Ka Clagg | //.  {(1 - 2 * νa) / (1 - νa) → τa};
             \    1 - νa                                /

               /                       1 - 2 νp   C2paste\
σrpasteint = |3 Kp C1paste - 6 Kp -------- -------| /.
               \                        1 + νp      Ri³  /
    {(1 - 2 * νp) / (1 - νp) → τp, (1 - 2 * νp) / (1 + νp) → χp} ;

BC2 = σraggint == σrpasteint;
```

The radial stress of the matrix is set equal to the applied stress at the outer surface of the sphere in the subsection below.

$$\sigma\mathtt{rpasteout} = \left(-\frac{1-2\,\nu\mathtt{p}}{1-\nu\mathtt{p}}\,2\,\frac{\mathtt{Kp}}{\mathtt{Ro}^3}\left(\mathtt{Ro}^3-\mathtt{Ri}^3\right)*\epsilon\mathtt{fpasteave}+ \right.$$
$$\left. 3\,\mathtt{Kp}\,\mathtt{C1paste}-6\,\frac{1-2*\nu\mathtt{p}}{1+\nu\mathtt{p}}\,\frac{\mathtt{Kp}}{\mathtt{Ro}^3}\,\mathtt{C2paste}\right)\ /.$$
$$\{(1-2*\nu\mathtt{p})\ /\ (1-\nu\mathtt{p})\rightarrow\tau\mathtt{p},\ \ (1-2*\nu\mathtt{p})\ /\ (1+\nu\mathtt{p})\rightarrow\chi\mathtt{p}\};$$

```
BC3 = σrpasteout == σapplied;
```

The above three boundary conditions are solved here to get the three unknown integration constants.

```
IntConst = Solve[{BC1, BC2, BC3}, {C1agg, C1paste, C2paste}];
C1AGG = FullSimplify[C1agg /. IntConst];
C1PASTE = FullSimplify[C1paste /. IntConst];
C2PASTE = FullSimplify[C2paste /. IntConst];
```

Development of Free Strain during Freezing

The above developed elastic model is then extended to include poromechanical constitutive properties based on the theory developed by Biot [13] and discussed by Coussy [9], [14], and Coussy and Monteiro [12], [15]. This is done in this section.

Free Strain and the Continuity Equation

The Gibbs_Thomson Equation relating the crystal and liquid pressure to the freezing temperature (ΔT) and melting entropy (Ξ_m) is given by

$$\left(1-\frac{\rho c}{\rho l}\right)(\mathrm{pl}-\mathrm{patm})+\mathrm{pc}-\mathrm{pl} == \Xi\mathrm{m}\,\Delta\mathrm{T}$$

Under the stress-free condition the volumetric free strain is given by:

$$\epsilon\mathrm{f} = \frac{\mathrm{b\,p}-3\,\alpha\,\mathrm{Kp}\,\Delta\mathrm{T}}{\mathrm{Kp}}$$

In the case of freezing water-infiltrated porous material subjected to a temperature below 0°C; the pore pressure is no longer uniform since the porous space is partly occupied by ice crystals at pressure p_c and partly occupied by the water remaining in liquid form at pressure p_l:

$$\epsilon\mathrm{f} = \frac{\mathrm{bc\,pc}\ +\mathrm{bl\,pl}\ -3\,\alpha\,\mathrm{Kp}\,\Delta\mathrm{T}}{\mathrm{Kp}}$$

Replacing p_c from the above equation using the Gibbs-Thomson Law gives the expression of one dimensional free strains as a function of S_j, p_l, and ΔT:

$$\epsilon\mathtt{falinear} = \mathtt{FullSimplify}\left[\frac{1}{3}\left(\frac{\mathtt{bca\,pca}}{\mathtt{Ka}}+\frac{\mathtt{bla\,pla[r,\ t]}}{\mathtt{Ka}}-3\,\alpha\mathtt{a}\ \Delta\mathtt{T[r,\ t]}\right)\ //. \right.$$
$$\left. \mathtt{pca} \mathbin{-\!\!>} \Xi\mathtt{m}\,\Delta\mathtt{T[r,\ t]}+\mathtt{pla[r,\ t]}-\left(1-\frac{\rho\mathtt{c}}{\rho\mathtt{l}}\right)\mathtt{pla[r,\ t]}\ \right];$$

$$\texttt{efplinear} = \texttt{FullSimplify}\left[\frac{1}{3}\left(\frac{\texttt{bcp pcp}}{\texttt{Kp}} + \frac{\texttt{blp plp[r, t]}}{\texttt{Kp}} - 3\,\alpha\texttt{p}\,\Delta\texttt{T[r, t]}\right) \texttt{//.}\right.$$

$$\left.\texttt{pcp} \to \Xi\texttt{m}\,\Delta\texttt{T[r, t]} + \texttt{plp[r, t]} - \left(1 - \frac{\rho\texttt{c}}{\rho\texttt{l}}\right)\texttt{plp[r, t]}\right];$$

Bulk strains of aggregate and matrix are given by:

$$\texttt{ekkagg} = \texttt{Xx}\,\epsilon\texttt{faave[t]} + 3\,\beta\texttt{a}\,\epsilon\texttt{falinear} + \texttt{Ww}\,\epsilon\texttt{fpave[t]} + \frac{\sigma\texttt{app [t] Ro}^3\,(1 + 2\,\chi\texttt{p})}{\texttt{Zz}};$$

$$\texttt{ekkpaste} = \texttt{Uu}\,\epsilon\texttt{faave[t]} + \texttt{Vv}\,\epsilon\texttt{fpave[t]} + 3\,\beta\texttt{p}\,\epsilon\texttt{fplinear} + \frac{\sigma\texttt{app[t] Ro}^3\,(\texttt{Ka} + 2\,\texttt{Kp}\,\chi\texttt{p})}{\texttt{Kp Zz}};$$

where

$$\epsilon\text{faggavrage[t]} = \frac{3}{\text{Ri}^3}\int_0^{\text{Ri}} \epsilon\text{falinear}\, r^2\, dr$$

$$\epsilon\text{fpasteaverage[t]} = \frac{3}{\text{Ro}^3 - \text{Ri}^3}\int_{\text{Ri}}^{\text{Ro}} \epsilon\text{fplinear}\, r^2\, dr$$

The total mass of water (m_w) currently contained in the porous material per unit of initial volume $d\Omega_o$ in both liquid and solid form is:

$\text{mw} = \rho\text{l}\,\phi\text{o} + \rho\text{l}\,(\mathcal{V}\Delta\rho + \mathcal{V}\phi)$

where, $\mathcal{V}_{\Delta\rho}$ is the pore volume change due to the change in saturation (S_j) under the condition $S_c + S_l = 1$, and due to the mass density difference between the two constituent species, j.

$$\mathcal{V}\Delta\rho\texttt{a} = \left(\frac{\rho\texttt{c}}{\rho\texttt{l}} - 1\right)\phi\texttt{oa Sca};$$

$$\mathcal{V}\Delta\rho\texttt{p} = \left(\frac{\rho\texttt{c}}{\rho\texttt{l}} - 1\right)\phi\texttt{op Scp};$$

$\mathcal{V}_\phi$ is the pore volume change due to the thermomechanical loading in unsaturated condition. For the aggregate, $\mathcal{V}_\phi$can be given as:

$$\mathcal{V}\phi\texttt{al} = \texttt{FullSimplify}\left[\texttt{Factor}\left[\texttt{ba ekkagg} + \frac{\texttt{pla[r, t]}}{\texttt{Mla}} + \right.\right.$$

$$\frac{\texttt{pca}}{\texttt{Mca}} + 3\,\Delta\texttt{T[r, t]}\,(\texttt{aca} + \texttt{ala} + \texttt{Sla}\,\alpha\texttt{l}\,\phi\texttt{oa} + \texttt{Sca}\,\alpha\texttt{c}\,\phi\texttt{oa})\ \texttt{//.}$$

$$\left\{\texttt{pca -> }\Xi\texttt{m}\,\Delta\texttt{T[r, t]} + \texttt{pla[r, t]} - \left(1 - \frac{\rho\texttt{c}}{\rho\texttt{l}}\right)\texttt{pla[r, t]},\right.$$

$$\left.\left.\left.\texttt{aca -> }\alpha\texttt{a}\,(\texttt{bca} - \phi\texttt{oa Sca}),\ \texttt{ala -> }\alpha\texttt{a}\,(\texttt{bla} - \phi\texttt{oa Sla})\right\}\right]\right]\ \texttt{//.}$$

$$\{\texttt{Zz}\,(\texttt{Mla}\,(\texttt{Ka} + \texttt{ba bca Mca}\,\beta\texttt{a})\,\rho\texttt{c} + \texttt{Mca}\,(\texttt{Ka} + \texttt{ba bla Mla}\,\beta\texttt{a})\,\rho\texttt{l}) \to \texttt{Aa}\};$$

The above expression is simplified as:

$$\texttt{part}\Delta\texttt{Tagg} = \frac{1}{\texttt{Ka Mca Mla Zz}\,\rho\texttt{l}}\texttt{Mla}\,\rho\texttt{l Zz}$$

$$(\texttt{bca Mca}\,(3\,\texttt{Ka}\,\alpha\texttt{a} + \texttt{ba}\,\beta\texttt{a}\,\Xi\texttt{m}) + \texttt{Ka}\,(\Xi\texttt{m} + 3\,\texttt{Mca}\,(\texttt{bla}\,\alpha\texttt{a} - \texttt{ba}\,\alpha\texttt{a}\,\beta\texttt{a})))\,\Delta\texttt{T[r, t]};$$

$$\mathrm{part\Delta Ttimes Satagg} = \frac{1}{\mathrm{Ka\ Mca\ Mla\ Zz}\ \rho\mathrm{l}}\ \mathrm{Mla}\ \rho\mathrm{l\ Zz\ (Ka\ (3\ Mca\ ((-Sca}\ \alpha\mathrm{a - Sla}\ \alpha\mathrm{a + Sca}\ \alpha\mathrm{c + Sla}\ \alpha\mathrm{l)}\ \phi\mathrm{oa)))}\ \Delta\mathrm{T[r,\ t];}$$

$$\mathrm{partremainingagg} = \frac{1}{\mathrm{Ka\ Mca\ Mla\ Zz}\ \rho\mathrm{l}}\Big(\mathrm{Aa\ pla[r,\ t]} + \mathrm{Mla}\ \rho\mathrm{l}\ \Big(\mathrm{ba\ Ka\ Mca}\ \Big(\mathrm{Xx\ Zz}\ \epsilon\mathrm{faave[t] + Ww\ Zz}\ \epsilon\mathrm{fpave[t] + Ro^3\ (1 + 2}\ \chi\mathrm{p)}\ \sigma\mathrm{app[t]}\Big)\Big)\Big);$$

$$\mathrm{simpl}\mathcal{V}\phi\mathrm{a = part\Delta Tagg + part\Delta Ttimes Satagg + partremainingagg;}$$

The above simplification can be checked by:

$$\mathrm{checksimagg = FullSimplify[simpl}\mathcal{V}\phi\mathrm{a} - \mathcal{V}\phi\mathrm{a1]}$$

0

Therefore, the simplified $\mathcal{V}_\phi$ for the aggregate can be written as:

$$\mathcal{V}\phi\mathrm{a = simpl}\mathcal{V}\phi\mathrm{a\ //.\ \{part\Delta Tagg \to Bb}\ \Delta\mathrm{T[r,\ t],\ part\Delta Ttimes Satagg\ {-}{>}\ \Delta Ttimes Satagg\};}$$

For the matrix shell, $\mathcal{V}_\phi$ can be written as:

$$\mathcal{V}\phi\mathrm{p1 = FullSimplify}\Big[\mathrm{Factor}\Big[\mathrm{bp}\ \epsilon\mathrm{kkpaste} + \frac{\mathrm{plp[r,\ t]}}{\mathrm{Mlp}} + \frac{\mathrm{pcp}}{\mathrm{Mcp}} + 3\ \Delta\mathrm{T[r,\ t]\ (acp + alp + Slp}\ \alpha\mathrm{l}\ \phi\mathrm{op + Scp}\ \alpha\mathrm{c}\ \phi\mathrm{op\ )\ //.}$$
$$\Big\{\mathrm{pcp\ {-}{>}\ \Xi m}\ \Delta\mathrm{T[r,\ t] + plp[r,\ t]} - \left(1 - \frac{\rho\mathrm{c}}{\rho\mathrm{l}}\right)\mathrm{plp[r,\ t]\ ,}$$
$$\mathrm{acp\ {-}{>}}\ \alpha\mathrm{p\ (bcp} - \phi\mathrm{op\ Scp),\ alp\ {-}{>}}\ \alpha\mathrm{p\ (blp} - \phi\mathrm{op\ Slp)}\Big\}\Big]\ \Big]\ \mathrm{//.}$$
$$\mathrm{\{Zz\ (Mlp\ (Kp + bcp\ bp\ Mcp}\ \beta\mathrm{p)}\ \rho\mathrm{c + Mcp\ (Kp + blp\ bp\ Mlp}\ \beta\mathrm{p)}\ \rho\mathrm{l)} \to \mathrm{Cc\};}$$

This can be further simplified as:

$$\mathrm{part\Delta Tpas} = \frac{1}{\mathrm{Kp\ Mcp\ Mlp\ Zz}\ \rho\mathrm{l}}\ \mathrm{(Mlp}\ \rho\mathrm{l\ (Zz\ (bcp\ Mcp\ (3\ Kp}\ \alpha\mathrm{p + bp}\ \beta\mathrm{p\ \Xi m) + Kp\ (\Xi m + 3\ Mcp\ (}\alpha\mathrm{p\ (blp - bp}\ \beta\mathrm{p))))}\ \Delta\mathrm{T[r,\ t]));}$$

$$\mathrm{part\Delta Ttimes Satpas} = \frac{1}{\mathrm{Kp\ Mcp\ Mlp\ Zz}\ \rho\mathrm{l}}\ \mathrm{(Mlp}\ \rho\mathrm{l\ (Zz\ (Kp\ (3\ Mcp\ ((Scp}\ \alpha\mathrm{c + Slp}\ \alpha\mathrm{l)}\ \phi\mathrm{op} + \alpha\mathrm{p\ (-\ (Scp + Slp)}\ \phi\mathrm{op))))}\ \Delta\mathrm{T[r,\ t]));}$$

$$\mathrm{partremainingpas} = \frac{1}{\mathrm{Kp\ Mcp\ Mlp\ Zz}\ \rho\mathrm{l}}\Big(\mathrm{Cc\ plp[r,\ t]} + \mathrm{Mlp}\ \rho\mathrm{l}\ \Big(\mathrm{bp\ Mcp}\ \Big(\mathrm{Kp\ Uu\ Zz}\ \epsilon\mathrm{faave[t] + Kp\ Vv\ Zz}\ \epsilon\mathrm{fpave[t] + Ro^3\ (Ka + 2\ Kp}\ \chi\mathrm{p)}\ \sigma\mathrm{app[t]}\Big)\Big)\Big);$$

$$\mathrm{simpl}\mathcal{V}\phi\mathrm{p = part\Delta Tpas + part\Delta Ttimes Satpas + partremainingpas;}$$

The above simplification can be checked by:

$$\mathrm{checksimpas = FullSimplify[simpl}\mathcal{V}\phi\mathrm{p} - \mathcal{V}\phi\mathrm{p1]}$$

0

Therefore, the simplified $\mathcal{V}_\phi$ for the matrix shell can be written as:

$$\mathcal{V}\phi\mathrm{p = simpl}\mathcal{V}\phi\mathrm{p\ //.\ \{part\Delta Tpas \to Dd}\ \Delta\mathrm{T[r,\ t],\ part\Delta Ttimes Satpas\ {-}{>}\ \Delta Ttimes Satpas\};}$$

where $\frac{1}{Mj} = \frac{(bj-\phi o Sj)}{Ks} + \frac{\phi o Sj}{Kj}$ with K_s and K_j being the bulk modulus of the porous body and different (crystal and liquid) phases of water, respectively. We got the above equation by replacing p_c from the Gibbs-Thomson equation, and $a_j = \alpha(b_j - \phi_o S_j)$. Here, a_j is the coefficient related to the thermal volumetric dilation of the pore volume occupied by the species j.

The liquid continuity equation together with Darcy's law gives $\frac{1}{\rho l} \frac{\partial}{\partial t} (mw) = \frac{1}{\rho l} \frac{\partial}{\partial t} (\rho l\, \phi o + \rho l\, (\mathcal{V}\Delta\rho + \mathcal{V}\phi)) = \frac{k}{\eta l} \frac{1}{r^2} \frac{\partial}{\partial r} \left(r^2 \frac{\partial pl(r,t)}{\partial r}\right)$. Since ϕo and ρl are constant, the above equation can be written as: $\frac{\partial}{\partial t} (\mathcal{V}\Delta\rho + \mathcal{V}\phi) = \frac{k}{\eta l} \frac{1}{r^2} \frac{\partial}{\partial r} \left(r^2 \frac{\partial pl(r,t)}{\partial r}\right)$

```
aggstorage = FullSimplify[Factor[ 𝒱Δρa + 𝒱ϕa]];
pastestorage = FullSimplify[Factor[𝒱Δρp + 𝒱ϕp]];
```

Laplace transformation of storage variation in aggregates eliminates the time derivative from the above equations, and is given as $\mathcal{L}\left(\frac{d\mathcal{V}\phi(t)}{dt}\right) = s\overline{\mathcal{V}\phi}(s) - \mathcal{V}\phi(t = 0)$. Initially, the total mass (mw) is equal to ρl ϕo, and $\mathcal{V}\Delta\rho + \mathcal{V}\phi = 0$, the initial value of $(\mathcal{V}\Delta\rho + \mathcal{V}\phi)$ must be zero. Therefore:

```
aggstorageinitial = 0;
LPaggstorage = s aggstorage - aggstorageinitial //. {pla[r, t] → pla[r, s],
    ΔT[r, t] -> ΔT, εfaave[t] -> εfaave, εfpave[t] -> εfpave, σapp[t] -> σapp};
```

The above equation is simplified as:

```
                                  1
partpla = FullSimplify[―――――――――――――――――― Aa s pla[r, s]];
                        Ka Mca Mla Zz ρl
partfa = FullSimplify[
   (s (Ka Mca Mla (Zz (ΔTtimesSatagg ρl + (Bb ΔT + ba Xx εfaave + ba Ww εfpave) ρl +
                   Sca (ρc - ρl) ϕoa) + ba Ro³ ρl σapp (1 + 2 χp)))) / (Ka Mca Mla Zz ρl)];
```

The above simplification can be checked by:

```
LPaggstor = partpla + partfa;
Checkaggstor = FullSimplify[LPaggstorage - LPaggstor]
0
```

The simplified expression for storage variation in the aggregate in the Laplace transformed domain is:

```
LPaggst = LPaggstor //. {partfa -> fa[s], partpla → Cpla pla[r, s]}
fa[s] + Cpla pla[r, s]
```

Similarly, Laplace transformation of the storage variation in the matrix is given as:

```
pastestorageinitial = 0;
LPpastestorage =
  (s pastestorage - pastestorageinitial) //. {plp[r, t] → plp[r, s],
    ΔT[r, t] -> ΔT, εfaave[t] -> εfaave, εfpave[t] -> εfpave, σapp[t] -> σapp};
```

The above equation is simplified as:

$$\mathtt{partplp = FullSimplify}\left[\frac{1}{\mathtt{Kp\ Mcp\ Mlp\ Zz}\ \rho\mathtt{l}}\ (\mathtt{Cc\ s\ plp[r,\ s]})\right];$$

$$\begin{aligned}&\mathtt{partfp = FullSimplify}\Big[\\ &\quad\Big(\mathtt{s}\ \Big(\mathtt{Mcp\ Mlp}\ \Big(\mathtt{Kp\ Zz}\ (\Delta\mathtt{TtimesSatpas}\ \rho\mathtt{l} + (\mathtt{Dd}\ \Delta\mathtt{T} + \mathtt{bp\ Uu\ efaave} + \mathtt{bp\ Vv\ efpave})\ \rho\mathtt{l}\ +\\ &\qquad\qquad\qquad \mathtt{Scp}\ (\rho\mathtt{c} - \rho\mathtt{l})\ \phi\mathtt{op})\ +\\ &\qquad\qquad \mathtt{bp\ Ro}^3\ \rho\mathtt{l}\ \sigma\mathtt{app}\ (\mathtt{Ka} + 2\ \mathtt{Kp}\ \chi\mathtt{p})\Big)\Big)\Big) \Big/ (\mathtt{Kp\ Mcp\ Mlp\ Zz}\ \rho\mathtt{l})\Big];\end{aligned}$$

The above simplification can be checked by:

```
LPpastestor = partplp + partfp;
```

```
Checkaggstor = FullSimplify[LPpastestorage - LPpastestor];
```

The simplified expression for storage variation in the matrix in the Laplace transformed domain is:

```
LPpastest = LPpastestor //. {partplp → Cplp plp[r, s], partfp → fp[s]}
fp[s] + Cplp plp[r, s]
```

Solution to Continuity Equations

Continuity equations for the pore liquid pressure in the aggregate core and the matrix shell in the Laplace transformed domain are given by:

$$\text{fa[s]} + \text{Cpla pla[r, s]} == \frac{\text{ka}}{\eta\text{l}}\,\frac{1}{\text{r}^2}\,\text{D}\left[\text{r}^2\,\text{D}\,[\text{pla[r, s], r], r}\right]$$

$$= > \frac{1}{\text{r}^2}\,\text{D}\left[\text{r}^2\,\text{D}\,[\text{pla[r, s], r], r}\right] - \frac{\eta\text{l}}{\text{ka}}\,\text{Cpla pla[r, s]} = \frac{\eta\text{l}}{\text{ka}}\,\text{fa[s]}$$

$$= > \frac{1}{\text{r}^2}\,\text{D}\left[\text{r}^2\,\text{D}\,[\text{pla[r, s], r], r}\right] - \mathcal{T}\text{a pla[r, s]} = \text{FA}$$

$$\text{fp[s]} + \text{Cplp plp[r, s]} == \frac{\text{kp}}{\eta\text{l}}\,\frac{1}{\text{r}^2}\,\text{D}\left[\text{r}^2\,\text{D}\,[\text{plp[r, s], r], r}\right]$$

$$= > \frac{1}{\text{r}^2}\,\text{D}\left[\text{r}^2\,\text{D}\,[\text{plp[r, s], r], r}\right] - \frac{\eta\text{l}}{\text{kp}}\,\text{Cplp plp[r, s]} = \frac{\eta\text{l}}{\text{kp}}\,\text{fp[s]}$$

$$= > \frac{1}{\text{r}^2}\,\text{D}\left[\text{r}^2\,\text{D}\,[\text{plp[r, s], r], r}\right] - \mathcal{T}\text{p plp[r, s]} = \text{FP}$$

These above two equations are solved in terms of the coefficients FA$\left(= \frac{\eta\text{l}}{\text{ka}}\,\text{fa[s]}\right)$and

FP$\left(= \frac{\eta\text{l}}{\text{kp}}\,\text{fp[s]}\right)$with the help of the boundary conditions. Volume average of the pore liquid pressure in the aggregate and matrix are then calculated. These two equations and the expressions for the FA and FP are then solved together to get the expressions for ϵfaave, ϵfpave, FA, and FP. After that, FA and FP are substituted in the solution to the pore pressure. However, the pore pressure results obtained have one more unknown, Qint, the pore liquid flux at the aggregate – matrix interface. This is then calculated using the last boundary condition where the pore pressure at the interface in aggregate is equal to that in paste. Finally, the interfacial pore pressure is substituted in the expression obtained for the liquid pore pressure in aggregate and paste. This pore pressure term is then substituted in the, stress strain terms in the Laplaced transformed domain. The solution thus obtained in the Laplace transformed domain is then numerically inverted to the time domain using the Stehfest Algorithm [20].

Together with the boundary conditions, solution to the continuity equations are given by the following commands

```
solagg =
  FullSimplify[DSolve[{(1/r^2) * D[r^2 D[pla[r, s], r], r] - 𝒯a pla[r, s] == FA,
     ka (Derivative[1, 0][pla][Ri, s]) == Qint,
     Derivative[1, 0][pla][0, s] == 0}, pla[r, s], {r, s}]];
PLA = Factor[pla[r, s] //. solagg];
solpaste = FullSimplify[
   DSolve[{(1 / r^2) * D[r^2 * D[plp[r, s], r], r] - 𝒯p plp[r, s] == FP,
     kp Derivative[1, 0][plp][Ri, s] == Qint,
     plp[Ro, s] == Papp}, plp[r, s], {r, s}]];
PLP = plp[r, s] //. solpaste;
```

where $\mathcal{T}a = \frac{\eta l}{ka}$ Cpla, $\mathcal{T}p = \frac{\eta l}{kp}$ Cplp, FA[s] = $\frac{\eta l}{ka}$fa[s], and FP[s]=$\frac{\eta l}{kp}$ fp[s]

Free strain for the aggregate core is then determined as:

```
єfal = FullSimplify[(1/3) (bca pca/Ka + bla pla[r, s]/Ka - 3 αa ΔT[r, s]) //.
     pca -> Ξm ΔT[r, s] + pla[r, s] - (1 - ρc/ρl) pla[r, s]] //.
   { Sla[r, t] → Sla, pla[r, s] → PLA, ΔT[r, s] -> ΔT};
```

whereas, the matrix shell is given by:

```
єfpl = FullSimplify[(1/3) (bcp pcp/Kp + blp plp[r, s]/Kp - 3 αp ΔT[r, s]) //.
     pcp → Ξm ΔT[r, s] + plp[r, s] - (1 - ρc/ρl) plp[r, s]] //.
   {Slp[r, t] → Slp, plp[r, s] → PLP, ΔT[r, s] -> ΔT};
```

Thereafter, volume average strain for the aggregate is calculated as:

```
єfaggave = FullSimplify[3/Ri^3 Integrate [{(єfal ) * r^2}, {r, 0, Ri}]];
```

The above expression is then simplified as:

```
partqint = FullSimplify[
    (bca (3 Qint - 0 ka Ri) ρc + (bla (3 Qint - 0 ka Ri) + ka Ri 𝒯a 0 (-3 Ka αa + bca Ξm))
        ρl) / (3 ka Ka Ri 𝒯a ρl)];
partconst = FullSimplify[
    (bca (3 × 0 - 0 ka Ri) ρc + (bla (3 × 0 - 0 ka Ri) + ka Ri 𝒯a ΔT (-3 Ka αa + bca Ξm))
        ρl) / (3 ka Ka Ri 𝒯a ρl)];
partfas = FullSimplify[
    (bca (3 × 0 - FA ka Ri) ρc + (bla (3 × 0 - FA ka Ri) + ka Ri 𝒯a 0 (-3 Ka αa + bca Ξm))
        ρl) / (3 ka Ka Ri 𝒯a ρl)];
```

Therefore, the simplified volume average strain for the aggregate core is:

```
efaggaverage = partqint + partconst + partfas;
EQ1 = εfaave == FullSimplify[
    efaggaverage //. {partqint → h1 Qint, partconst → h3, partfas → h2 FA }]
εfaave == FA h2 + h3 + h1 Qint
```

The above simplification can be checked by:

```
Checkefa = FullSimplify[efaggave - efaggaverage]
{{0}}
```

The volume average strain for the matrix shell is given by:

$$\mathtt{efpasteave} = \mathtt{FullSimplify}\left[\frac{3}{\mathrm{Ro}^3-\mathrm{Ri}^3}\ \mathtt{Integrate}\left[(\epsilon\mathrm{fpl}) * r^2,\ \{r,\ \mathrm{Ri},\ \mathrm{Ro}\}\right]\right];$$

This is further simplified as:

$$\mathtt{partfps} = \mathtt{FullSimplify}\Bigg[\frac{1}{3\,\mathrm{Kp}\,(\mathrm{Ri}^3-\mathrm{Ro}^3)\,\mathcal{T}\mathrm{p}^2\,\rho\mathrm{l}}\Bigg(\frac{3\times 0\,\mathrm{Ri}^2\,\mathcal{T}\mathrm{p}\,(\mathrm{bcp}\,\rho\mathrm{c}+\mathrm{blp}\,\rho\mathrm{l})}{\mathrm{kp}} - 3\,\mathrm{Ro}\left(-1+\mathrm{Ro}\sqrt{\mathcal{T}\mathrm{p}}\right)$$
$$(\mathrm{FP}+0\,\mathcal{T}\mathrm{p})\,(\mathrm{bcp}\,\rho\mathrm{c}+\mathrm{blp}\,\rho\mathrm{l}) + \left(6\,e^{\mathrm{Ri}\sqrt{\mathcal{T}\mathrm{p}}}\,\mathrm{Ro}\sqrt{\mathcal{T}\mathrm{p}}\left(-e^{\mathrm{Ro}\sqrt{\mathcal{T}\mathrm{p}}}\,0\,\mathrm{Ri}^2\,\mathcal{T}\mathrm{p}+\right.\right.$$
$$\left.\left.e^{\mathrm{Ri}\sqrt{\mathcal{T}\mathrm{p}}}\,\mathrm{kp}\,\mathrm{Ro}\left(-1+\mathrm{Ri}\sqrt{\mathcal{T}\mathrm{p}}\right)(\mathrm{FP}+0\,\mathcal{T}\mathrm{p})\right)(\mathrm{bcp}\,\rho\mathrm{c}+\mathrm{blp}\,\rho\mathrm{l})\right)\Big/$$
$$\left(e^{2\,\mathrm{Ri}\sqrt{\mathcal{T}\mathrm{p}}}\,\mathrm{kp}\left(-1+\mathrm{Ri}\sqrt{\mathcal{T}\mathrm{p}}\right)+e^{2\,\mathrm{Ro}\sqrt{\mathcal{T}\mathrm{p}}}\,\mathrm{kp}\left(1+\mathrm{Ri}\sqrt{\mathcal{T}\mathrm{p}}\right)\right) -$$
$$\mathrm{Ri}^3\,\mathcal{T}\mathrm{p}\,(\mathrm{bcp}\,\mathrm{FP}\,\rho\mathrm{c}+\mathrm{blp}\,\mathrm{FP}\,\rho\mathrm{l}+3\,\mathrm{Kp}\,\mathcal{T}\mathrm{p}\,\alpha\mathrm{p}\,0\,\rho\mathrm{l}-\mathrm{bcp}\,\mathcal{T}\mathrm{p}\,0\,\Xi\mathrm{m}\,\rho\mathrm{l}) +$$
$$\mathrm{Ro}^3\,\mathcal{T}\mathrm{p}\,(\mathrm{bcp}\,\mathrm{FP}\,\rho\mathrm{c}+\mathrm{blp}\,\mathrm{FP}\,\rho\mathrm{l}+3\,\mathrm{Kp}\,\mathcal{T}\mathrm{p}\,\alpha\mathrm{p}\,0\,\rho\mathrm{l}-\mathrm{bcp}\,\mathcal{T}\mathrm{p}\,0\,\Xi\mathrm{m}\,\rho\mathrm{l})\Bigg)\Bigg];$$

$$\text{partqintp} = \text{FullSimplify}\Bigg[\frac{1}{3\ \text{Kp}\left(\text{Ri}^3-\text{Ro}^3\right)\mathcal{T}\text{p}^2\ \rho\text{l}} \Bigg(\frac{3\ \text{Qint}\ \text{Ri}^2\ \mathcal{T}\text{p}\ (\text{bcp}\ \rho\text{c}+\text{blp}\ \rho\text{l})}{\text{kp}} - 3\ \text{Ro}\left(-1+\text{Ro}\sqrt{\mathcal{T}\text{p}}\right)(0)\ (\text{bcp}\ \rho\text{c}+\text{blp}\ \rho\text{l}) + \Big(6\ e^{\text{Ri}\sqrt{\mathcal{T}\text{p}}}\ \text{Ro}\sqrt{\mathcal{T}\text{p}}\left(-e^{\text{Ro}\sqrt{\mathcal{T}\text{p}}}\ \text{Qint}\ \text{Ri}^2\ \mathcal{T}\text{p}+e^{\text{Ri}\sqrt{\mathcal{T}\text{p}}}\ \text{kp}\ \text{Ro}\left(-1+\text{Ri}\sqrt{\mathcal{T}\text{p}}\right)(0)\right)(\text{bcp}\ \rho\text{c}+\text{blp}\ \rho\text{l})\Big)\Big/\left(e^{2\,\text{Ri}\sqrt{\mathcal{T}\text{p}}}\ \text{kp}\left(-1+\text{Ri}\sqrt{\mathcal{T}\text{p}}\right)+e^{2\,\text{Ro}\sqrt{\mathcal{T}\text{p}}}\ \text{kp}\left(1+\text{Ri}\sqrt{\mathcal{T}\text{p}}\right)\right) - \text{Ri}^3\ \mathcal{T}\text{p}\ (0)+\text{Ro}^3\ \mathcal{T}\text{p}\ (0)\Bigg)\Bigg];$$

$$\text{partconstp} = \text{FullSimplify}\Bigg[\frac{1}{3\ \text{Kp}\left(\text{Ri}^3-\text{Ro}^3\right)\mathcal{T}\text{p}^2\ \rho\text{l}} \Bigg(\frac{3\times 0\ \text{Ri}^2\ \mathcal{T}\text{p}\ (\text{bcp}\ \rho\text{c}+\text{blp}\ \rho\text{l})}{\text{kp}} - 3\ \text{Ro}\left(-1+\text{Ro}\sqrt{\mathcal{T}\text{p}}\right)(0)\ (\text{bcp}\ \rho\text{c}+\text{blp}\ \rho\text{l}) + \Big(6\ e^{\text{Ri}\sqrt{\mathcal{T}\text{p}}}\ \text{Ro}\sqrt{\mathcal{T}\text{p}}\left(-e^{\text{Ro}\sqrt{\mathcal{T}\text{p}}}\ 0\ \text{Ri}^2\ \mathcal{T}\text{p}+e^{\text{Ri}\sqrt{\mathcal{T}\text{p}}}\ \text{kp}\ \text{Ro}\left(-1+\text{Ri}\sqrt{\mathcal{T}\text{p}}\right)(0)\right)(\text{bcp}\ \rho\text{c}+\text{blp}\ \rho\text{l})\Big)\Big/\left(e^{2\,\text{Ri}\sqrt{\mathcal{T}\text{p}}}\ \text{kp}\left(-1+\text{Ri}\sqrt{\mathcal{T}\text{p}}\right)+e^{2\,\text{Ro}\sqrt{\mathcal{T}\text{p}}}\ \text{kp}\left(1+\text{Ri}\sqrt{\mathcal{T}\text{p}}\right)\right) - \text{Ri}^3\ \mathcal{T}\text{p}\ (0+3\ \text{Kp}\ \mathcal{T}\text{p}\ \alpha\text{p}\ \Delta\text{T}\ \rho\text{l}-\text{bcp}\ \mathcal{T}\text{p}\ \Delta\text{T}\ \Xi\text{m}\ \rho\text{l}) + \text{Ro}^3\ \mathcal{T}\text{p}\ (0+3\ \text{Kp}\ \mathcal{T}\text{p}\ \alpha\text{p}\ \Delta\text{T}\ \rho\text{l}-\text{bcp}\ \mathcal{T}\text{p}\ \Delta\text{T}\ \Xi\text{m}\ \rho\text{l})\Bigg)\Bigg];$$

$$\text{partpapp} = \text{FullSimplify}\Bigg[\frac{1}{3\ \text{Kp}\left(\text{Ri}^3-\text{Ro}^3\right)\mathcal{T}\text{p}^2\ \rho\text{l}} \Bigg(\frac{3\times 0\ \text{Ri}^2\ \mathcal{T}\text{p}\ (\text{bcp}\ \rho\text{c}+\text{blp}\ \rho\text{l})}{\text{kp}} - 3\ \text{Ro}\left(-1+\text{Ro}\sqrt{\mathcal{T}\text{p}}\right)(0+\text{Papp}\ \mathcal{T}\text{p})\ (\text{bcp}\ \rho\text{c}+\text{blp}\ \rho\text{l}) + \Big(6\ e^{\text{Ri}\sqrt{\mathcal{T}\text{p}}}\ \text{Ro}\sqrt{\mathcal{T}\text{p}}\left(-e^{\text{Ro}\sqrt{\mathcal{T}\text{p}}}\ 0\ \text{Ri}^2\ \mathcal{T}\text{p}+e^{\text{Ri}\sqrt{\mathcal{T}\text{p}}}\ \text{kp}\ \text{Ro}\left(-1+\text{Ri}\sqrt{\mathcal{T}\text{p}}\right)(0+\text{Papp}\ \mathcal{T}\text{p})\right)(\text{bcp}\ \rho\text{c}+\text{blp}\ \rho\text{l})\Big)\Big/\left(e^{2\,\text{Ri}\sqrt{\mathcal{T}\text{p}}}\ \text{kp}\left(-1+\text{Ri}\sqrt{\mathcal{T}\text{p}}\right)+e^{2\,\text{Ro}\sqrt{\mathcal{T}\text{p}}}\ \text{kp}\left(1+\text{Ri}\sqrt{\mathcal{T}\text{p}}\right)\right) - \text{Ri}^3\ \mathcal{T}\text{p}\ (0)+\text{Ro}^3\ \mathcal{T}\text{p}\ (0)\Bigg)\Bigg];$$

Therefore, the simplified volume average strain for the aggregate core is:

```
efpasteaverage = partfps + partqintp + partconstp + partpapp;
EQ2 = εfpave == efpasteaverage //.
   {partconstp → h4, partfps → h5 FP , partqintp → h6 Qint, partpapp → h7 Papp}
εfpave == h4 + FP h5 + h7 Papp + h6 Qint
```

The above simplification can be checked by:

```
Checkεfp = FullSimplify[εfpasteave - εfpasteaverage]
{0}
```

Expressions for FA and FP are given as:

```
EQ3 = FA == FullSimplify[ηl/ka partfa];

EQ4 = FP == FullSimplify[ηl/kp partfp];
```

EQ1, EQ2, EQ3 and EQ4 are then solved for FA, FP, εfaave, and εfpave:

```
SOL = Solve[{EQ1, EQ2, EQ3, EQ4}, {FA, FP, εfaave, εfpave}];
fas = FullSimplify[FA //. SOL];
fps = FullSimplify[FP //. SOL];
εfaggaver = FullSimplify[εfaave //. SOL];
εfpasteaver = FullSimplify[εfpave //. SOL];
```

FA and FP are then substituted in the expressions for the pore liquid pressure in the aggregate and matrix:

```
Plagg = PLA //. {FA → fas, ΔT[r, s] -> ΔT};
PLAGG = Plagg //.
    ηl (Kp Zz (kp - bp h5 s Vv ηl) (Sca ρc ϕoa + ρl (Bb ΔT + ΔTtimesSatagg - Sca ϕoa)) +
          ba (h4 kp Kp Ww Zz ρl + h7 kp Kp Papp Ww Zz ρl + h6 kp Kp Qint Ww Zz ρl +
              h3 kp Kp Xx Zz ρl + h1 kp Kp Qint Xx Zz ρl + bp h3 h5 Kp s Uu Ww Zz ηl ρl +
              bp h1 h5 Kp Qint s Uu Ww Zz ηl ρl - bp h3 h5 Kp s Vv Xx Zz ηl ρl -
              bp h1 h5 Kp Qint s Vv Xx Zz ηl ρl + Dd h5 Kp s Ww Zz ΔT ηl ρl +
              h5 Kp s Ww Zz ΔTtimesSatpas ηl ρl + kp Kp Ro^3 ρl σapp -
              bp h5 Kp Ro^3 s Vv ηl ρl σapp + bp h5 Ka Ro^3 s Ww ηl ρl σapp +
              h5 Kp s Scp Ww Zz ηl ρc ϕop - h5 Kp s Scp Ww Zz ηl ρl ϕop +
              2 Kp Ro^3 (kp + bp h5 s (-Vv + Ww) ηl) ρl σapp χp)) / (Kp Zz
          (ka (kp - bp h5 s Vv ηl) + ba h2 s ηl (-kp Xx + bp h5 s (-Uu Ww + Vv Xx) ηl))
          ρl) → gl;
Plpas = PLP //. {FP → fps, ΔT[r, s] -> ΔT};
```

```
PLPAS = Plpas //.
   η1 (Kp Zz (ka - ba h2 s Xx η1) (Scp ρc ϕop + ρl (Dd ΔT + ΔTtimesSatpas - Scp ϕop)) +
         bp (h3 ka Kp Uu Zz ρl + h1 ka Kp Qint Uu Zz ρl + h4 ka Kp Vv Zz ρl + h7 ka Kp
              Papp Vv Zz ρl + h6 ka Kp Qint Vv Zz ρl + ba h2 h4 Kp s Uu Ww Zz η1 ρl +
            ba h2 h7 Kp Papp s Uu Ww Zz η1 ρl + ba h2 h6 Kp Qint s Uu Ww Zz η1 ρl -
            ba h2 h4 Kp s Vv Xx Zz η1 ρl - ba h2 h7 Kp Papp s Vv Xx Zz η1 ρl -
            ba h2 h6 Kp Qint s Vv Xx Zz η1 ρl + Bb h2 Kp s Uu Zz ΔT η1 ρl +
            h2 Kp s Uu Zz ΔTtimesSatagg η1 ρl + ka Ka Ro³ ρl σapp +
            ba h2 Kp Ro³ s Uu η1 ρl σapp - ba h2 Ka Ro³ s Xx η1 ρl σapp +
            h2 Kp s Sca Uu Zz η1 ρc ϕoa - h2 Kp s Sca Uu Zz η1 ρl ϕoa +
            2 Kp Ro³ (ka + ba h2 s (Uu - Xx) η1) ρl σapp χp)) / (Kp Zz
         (ka (kp - bp h5 s Vv η1) + ba h2 s η1 (-kp Xx + bp h5 s (-Uu Ww + Vv Xx) η1))
         ρl) → g2;
```

Plagg and Plpas still have one more unknown Qint (pore liquid flux at the aggregate-matrix interface). So, Qint is determined to get the final expressions for pla and plp.

```
Paggint = Plagg //. r → Ri;
```

```
Ppasteint = Plpas //. r → Ri;
```

```
Qinterface = Solve[Paggint == Ppasteint, Qint];
```

```
QINT = Qint /. Qinterface;
```

```
efaaver = efaggaver //. Qint → QINT;
```

```
efpaver = efpasteaver //. Qint → QINT;
```

Pore Pressure

Pore liquid pressure in the aggregate:

```
Plp  =  Plpas //. Qint → QINT;
```

Pore liquid pressure in the matrix:

```
Pla = Plagg //. Qint → QINT;
```

Pore crystal pressure in the aggregate:

```
                ρc
pca = Ξm ΔT + —— Pla;
                ρl
```

Pore crystal pressure in the aggregate:

```
                ρc
pcp = Ξm ΔT + —— Plp;
                ρl
```

Linear Free Strain

Free strain in the aggregate:

$$\mathrm{\epsilon fagg} = \frac{(\mathrm{bca}\,\rho\mathrm{c} + \mathrm{bla}\,\rho\mathrm{l})\ \mathrm{PLAGG} + (-3\ \mathrm{Ka}\,\alpha\mathrm{a} + \mathrm{bca}\,\Xi\mathrm{m})\ \rho\mathrm{l}\,\Delta\mathrm{T}}{3\ \mathrm{Ka}\,\rho\mathrm{l}}\ /\!/.$$

$$\{\mathrm{Sla}[\mathrm{r},\ \mathrm{t}] \to \mathrm{Sla},\ \mathrm{Slp}[\mathrm{r},\ \mathrm{t}] \to \mathrm{Slp}\};$$

Free strain in the matrix:

$$\mathrm{efpaste} = \frac{(\mathrm{bcp}\,\rho\mathrm{c} + \mathrm{blp}\,\rho\mathrm{l})\ \mathrm{PLPAS} + (-3\ \mathrm{Kp}\,\alpha\mathrm{p} + \mathrm{bcp}\,\Xi\mathrm{m})\ \rho\mathrm{l}\,\Delta\mathrm{T}}{3\ \mathrm{Kp}\,\rho\mathrm{l}}\ /\!/.$$

$$\{\mathrm{Sla}[\mathrm{r},\ \mathrm{t}] \to \mathrm{Sla},\ \mathrm{Slp}[\mathrm{r},\ \mathrm{t}] \to \mathrm{Slp}\};$$

Poroelastic Behavior (Laplace Transformed Domain)

This section contains all the expressions of the poro-elastic response of the concrete sphere subjected to freeze-thaw cycles in the Laplace transformed domain.

Integration Constants

$$\begin{aligned}\mathrm{C1AGG} = {} & \Big(-\mathrm{Papp}\,\mathrm{Ro}^3\ (1 + 2\,\chi\mathrm{p}) + 2\ \big(\mathrm{Ka}\ \mathrm{efaaver}\ \tau\mathrm{a}\ (\mathrm{Ro}^3 + 2\ \mathrm{Ri}^3\,\chi\mathrm{p}) + {} \\ & \quad \mathrm{Kp}\ (\mathrm{Ri}^3 - \mathrm{Ro}^3)\ (3\ \beta\mathrm{a}\ \mathrm{efaaver}\ \chi\mathrm{p} - \mathrm{efpaver}\ (\tau\mathrm{p} + 2\ \tau\mathrm{p}\,\chi\mathrm{p}))\big)\Big)\ / \\ & \big(3\ \mathrm{Ka}\,\mathrm{Ro}^3 + 6\ \big((\mathrm{Ka} - \mathrm{Kp})\ \mathrm{Ri}^3 + \mathrm{Kp}\,\mathrm{Ro}^3\big)\ \chi\mathrm{p}\big);\end{aligned}$$

$$\begin{aligned}\mathrm{C1PASTE} = {} & \big(-\mathrm{Ka}\ \mathrm{Papp}\,\mathrm{Ro}^3 + 2\ \mathrm{Ka}\,\mathrm{Kp}\ (-\mathrm{Ri}^3 + \mathrm{Ro}^3)\ \mathrm{efpaver}\ \tau\mathrm{p} + 2\ \mathrm{Kp} \\ & \quad \big(-\mathrm{Papp}\,\mathrm{Ro}^3 + \mathrm{Ka}\,\mathrm{Ri}^3\ \mathrm{efaaver}\ (3\ \beta\mathrm{a} + 2\ \tau\mathrm{a}) + 2\ \mathrm{Kp}\ (-\mathrm{Ri}^3 + \mathrm{Ro}^3)\ \mathrm{efpaver}\ \tau\mathrm{p}\big)\ \chi\mathrm{p}\big)\ / \\ & \big(3\ \mathrm{Ka}\,\mathrm{Kp}\,\mathrm{Ro}^3 + 6\ \mathrm{Kp}\ \big((\mathrm{Ka} - \mathrm{Kp})\ \mathrm{Ri}^3 + \mathrm{Kp}\,\mathrm{Ro}^3\big)\ \chi\mathrm{p}\big);\end{aligned}$$

$$\begin{aligned}\mathrm{C2PASTE} = {} & \big(\mathrm{Ri}^3\ \big(\mathrm{Ro}^3\ (-\mathrm{Kp}\ \mathrm{Papp} + \mathrm{Ka}\ (\mathrm{Papp} + \mathrm{Kp}\ \mathrm{efaaver}\ (3\ \beta\mathrm{a} + 2\ \tau\mathrm{a}))) + {} \\ & \quad 2\ (\mathrm{Ka} - \mathrm{Kp})\ \mathrm{Kp}\ (\mathrm{Ri}^3 - \mathrm{Ro}^3)\ \mathrm{efpaver}\ \tau\mathrm{p}\big)\big)\ / \\ & \big(3\ \mathrm{Ka}\,\mathrm{Kp}\,\mathrm{Ro}^3 + 6\ \mathrm{Kp}\ \big((\mathrm{Ka} - \mathrm{Kp})\ \mathrm{Ri}^3 + \mathrm{Kp}\,\mathrm{Ro}^3\big)\ \chi\mathrm{p}\big);\end{aligned}$$

$$\mathrm{aggintegral} = \mathrm{Limit}\big[\mathrm{Integrate}\big[\mathrm{r}^2\ \mathrm{\epsilon fagg},\ \{\mathrm{r},\ \mathrm{a},\ \mathrm{r}\}\big],\ \mathrm{a} \to 0\big]\ /\!/.\ \mathrm{Qint} \to \mathrm{QINT};$$

$$\mathrm{pasteintegral} = \mathrm{Integrate}\big[\mathrm{r}^2\ \mathrm{efpaste},\ \{\mathrm{r},\ \mathrm{Ri},\ \mathrm{r}\}\big]\ /\!/.\ \mathrm{Qint} \to \mathrm{QINT};$$

Radial Stresses

Radial stress of the aggregate core:

$$\sigma\mathrm{ra} = -\frac{6\ \mathrm{Ka}\ \tau\mathrm{a}\ \mathrm{aggintegral}}{\mathrm{r}^3} + 3\ \mathrm{Ka}\ \mathrm{C1AGG};$$

Radial stress of the matrix shell:

$$\sigma\mathrm{rp} = -\frac{1}{\mathrm{r}^3}\ 6\ \mathrm{Kp}\ \tau\mathrm{p}\ \mathrm{pasteintegral} + 3\ \mathrm{Kp}\ \mathrm{C1PASTE} - 2\ \chi\mathrm{p}\ \mathrm{C2PASTE}\ 3\ \frac{\mathrm{Kp}}{\mathrm{r}^3};$$

Tangential Stresses

Tangential stress of the aggregate core:

$$\sigma\mathrm{ta} = \frac{3\ \mathrm{Ka}\ \tau\mathrm{a}\ \mathrm{aggintegral}}{\mathrm{r}^3} + 3\ \mathrm{Ka}\ \mathrm{C1AGG} - \tau\mathrm{a}\ 3\ \mathrm{Ka}\ \mathrm{\epsilon fagg}\ /\!/.\ \mathrm{Qint} \to \mathrm{QINT};$$

Tangential stress of the matrix shell:

$$\sigma\mathrm{tp} = \frac{1}{\mathrm{r}^3}\,3\,\mathrm{Kp}\,\tau\mathrm{p}\ \mathrm{pasteintegral} + 3\,\mathrm{Kp}\ \mathrm{C1PASTE} + \chi\mathrm{p}\ \mathrm{C2PASTE}\ 3\,\frac{\mathrm{Kp}}{\mathrm{r}^3} - \tau\mathrm{p}\ 3\,\mathrm{Kp}\ (\epsilon\mathrm{fpaste})\ \text{//.}\ \mathrm{Qint} \to \mathrm{QINT};$$

Radial Strains

Radial strain of the aggregate core:

$$\epsilon\mathrm{ra} = -\frac{2\times 3\,\beta\mathrm{a}\ \mathrm{aggintegral}}{\mathrm{r}^3} + 3\,\beta\mathrm{a}\ (\epsilon\mathrm{fagg}) + \mathrm{C1AGG}\ \text{//.}\ \mathrm{Qint} \to \mathrm{QINT};$$

Radial strain of the matrix shell:

$$\epsilon\mathrm{rp} = -\frac{2\times 3\,\beta\mathrm{p}\ \mathrm{pasteintegral}}{\mathrm{r}^3} + 3\,\beta\mathrm{p}\ (\epsilon\mathrm{fpaste}) + \mathrm{C1PASTE} - 2\,\frac{\mathrm{C2PASTE}}{\mathrm{r}^3}\ \text{//.}\ \mathrm{Qint} \to \mathrm{QINT};$$

Tangential Strains

Tangential strain of the aggregate core:

$$\epsilon\mathrm{ta} = \frac{3\,\beta\mathrm{a}\ \mathrm{aggintegral}}{\mathrm{r}^3} + \mathrm{C1AGG};$$

Tangential strain of the matrix shell:

$$\epsilon\mathrm{tp} = \frac{3\,\beta\mathrm{p}\ \mathrm{pasteintegral}}{\mathrm{r}^3} + \mathrm{C1PASTE} + \frac{\mathrm{C2PASTE}}{\mathrm{r}^3};$$

Bulk Strains

Bulk strain of the aggregate core:

$$\epsilon\mathrm{ka} = \epsilon\mathrm{ra} + 2\,\epsilon\mathrm{ta};$$

Bulk strain of the matrix shell:

$$\epsilon\mathrm{kp} = \epsilon\mathrm{rp} + 2\,\epsilon\mathrm{tp};$$

Average Bulk Strains

Average strains are given by :

$$\epsilon\mathrm{faggav}[\mathrm{t}] = \frac{3}{\mathrm{Ri}^3}\int_0^{\mathrm{Ri}} \epsilon\mathrm{falinear}\ \mathrm{r}^2\, d\mathrm{r};$$

$$\epsilon\mathrm{fpave}[\mathrm{t}] = \frac{3}{\mathrm{Ro}^3 - \mathrm{Ri}^3}\int_{\mathrm{Ri}}^{\mathrm{Ro}} \epsilon\mathrm{fplinear}\ \mathrm{r}^2\, d\mathrm{r};$$

Average bulk strain of the aggregate core :

$$\epsilon\mathrm{kka} = \mathrm{Xx}\ \epsilon\mathrm{faaver} + 3\,\beta\mathrm{a}\ \epsilon\mathrm{faggregate} + \mathrm{Ww}\ \epsilon\mathrm{fpaver} + \frac{\sigma\mathrm{app}\ \mathrm{Ro}^3\ (1 + 2\,\chi\mathrm{p})}{\mathrm{Zz}};$$

$$\epsilon\mathrm{kkaggave} = \epsilon\mathrm{kka}\ \text{//.}\ \epsilon\mathrm{faggregate} \text{->} \epsilon\mathrm{faaver};$$

Average bulk strain of the matrix shell :

$$\epsilon\mathrm{kkp} = \mathrm{Uu}\ \epsilon\mathrm{faaver} + \mathrm{Vv}\ \epsilon\mathrm{fpaver} + 3\ \beta\mathrm{p}\ \epsilon\mathrm{fpas} + \frac{\sigma\mathrm{app}\ \mathrm{Ro}^3\ (\mathrm{Ka} + 2\ \mathrm{Kp}\ \chi\mathrm{p})}{\mathrm{Kp}\ \mathrm{Zz}};$$

$$\epsilon\mathrm{kkpasave} = \epsilon\mathrm{kkp}\ //.\ \epsilon\mathrm{fpas} \text{ -> } \epsilon\mathrm{fpaver};$$

Average bulk strain of the matrixshell :

$$\epsilon\mathrm{kkave} = \frac{1}{\mathrm{Ro}^3}\left(\mathrm{Ri}^3\ \epsilon\mathrm{kkaggave} + \left(\mathrm{Ro}^3 - \mathrm{Ri}^3\right)\ \epsilon\mathrm{kkpasave}\right)\ //.\ \mathrm{Qint} \to \mathrm{QINT};$$

Coefficients

This section contains all the coefficients that are used to simplify the expressions.

$$\beta\mathrm{a} = \frac{(1 + \nu\mathrm{a})}{3\ (1 - \nu\mathrm{a})};$$

$$\tau\mathrm{a} = \frac{(1 - 2 * \nu\mathrm{a})}{(1 - \nu\mathrm{a})};$$

$$\chi\mathrm{a} = \frac{(1 - 2 * \nu\mathrm{a})}{(1 + \nu\mathrm{a})};$$

$$\beta\mathrm{p} = \frac{(1 + \nu\mathrm{p})}{3\ (1 - \nu\mathrm{p})};$$

$$\tau\mathrm{p} = \frac{(1 - 2 * \nu\mathrm{p})}{(1 - \nu\mathrm{p})};$$

$$\chi\mathrm{p} = \frac{(1 - 2 * \nu\mathrm{p})}{(1 + \nu\mathrm{p})};$$

$$\mathrm{Aa} = \mathrm{Zz}\ (\mathrm{Mla}\ (\mathrm{Ka} + \mathrm{ba}\ \mathrm{bca}\ \mathrm{Mca}\ \beta\mathrm{a})\ \rho\mathrm{c} + \mathrm{Mca}\ (\mathrm{Ka} + \mathrm{ba}\ \mathrm{bla}\ \mathrm{Mla}\ \beta\mathrm{a})\ \rho\mathrm{l});$$

$$\mathrm{Bb} = \frac{\mathrm{part}\Delta\mathrm{Tagg}}{\Delta\mathrm{T}[\mathrm{r},\ \mathrm{t}]};$$

$$\mathrm{Cc} = \mathrm{Zz}\ (\mathrm{Mlp}\ (\mathrm{Kp} + \mathrm{bcp}\ \mathrm{bp}\ \mathrm{Mcp}\ \beta\mathrm{p})\ \rho\mathrm{c} + \mathrm{Mcp}\ (\mathrm{Kp} + \mathrm{blp}\ \mathrm{bp}\ \mathrm{Mlp}\ \beta\mathrm{p})\ \rho\mathrm{l});$$

$$\mathrm{Dd} = \frac{\mathrm{part}\Delta\mathrm{Tpas}}{\Delta\mathrm{T}[\mathrm{r},\ \mathrm{t}]};$$

$$\mathrm{Zz} = \left(\mathrm{Ka}\ \mathrm{Ro}^3 + 2\ \left((\mathrm{Ka} - \mathrm{Kp})\ \mathrm{Ri}^3 + \mathrm{Kp}\ \mathrm{Ro}^3\right)\ \chi\mathrm{p}\right);$$

$$\mathrm{Xx} = \frac{1}{\mathrm{Zz}}\ 2\ \left(3\ \mathrm{Kp}\ \left(\mathrm{Ri}^3 - \mathrm{Ro}^3\right)\ \beta\mathrm{a}\ \chi\mathrm{p} + \mathrm{Ka}\ \tau\mathrm{a}\ \left(\mathrm{Ro}^3 + 2\ \mathrm{Ri}^3\ \chi\mathrm{p}\right)\right);$$

$$\mathrm{Ww} = -\frac{2\ \mathrm{Kp}\ \left(\mathrm{Ri}^3 - \mathrm{Ro}^3\right)\ \tau\mathrm{p}\ (1 + 2\ \chi\mathrm{p})}{\mathrm{Zz}};$$

$$\mathrm{Vv} = -\frac{2\ \left(\mathrm{Ri}^3 - \mathrm{Ro}^3\right)\ \tau\mathrm{p}\ (\mathrm{Ka} + 2\ \mathrm{Kp}\ \chi\mathrm{p})}{\mathrm{Zz}};$$

$$\mathrm{Uu} = \frac{2\,\mathrm{Ka}\,\mathrm{Ri}^3\,(3\,\beta\mathrm{a} + 2\,\tau\mathrm{a})\,\chi\mathrm{p}}{\mathrm{Zz}};$$

$$\mathrm{h1} = \frac{(\mathrm{bca}\,\rho\mathrm{c} + \mathrm{bla}\,\rho\mathrm{l})}{\mathrm{ka}\,\mathrm{Ka}\,\mathrm{Ri}\,\mathcal{T}\mathrm{a}\,\rho\mathrm{l}};$$

$$\mathrm{h2} = -\frac{(\mathrm{bca}\,\rho\mathrm{c} + \mathrm{bla}\,\rho\mathrm{l})}{3\,\mathrm{Ka}\,\mathcal{T}\mathrm{a}\,\rho\mathrm{l}};$$

$$\mathrm{h3} = -\alpha\mathrm{a}\,\Delta\mathrm{T} + \frac{\mathrm{bca}\,\Delta\mathrm{T}\,\Xi\mathrm{m}}{3\,\mathrm{Ka}};$$

$$\mathrm{h4} = -\alpha\mathrm{p}\,\Delta\mathrm{T} + \frac{\mathrm{bcp}\,\Delta\mathrm{T}\,\Xi\mathrm{m}}{3\,\mathrm{Kp}};$$

$$\mathrm{h5} = \Bigg(\Bigg(3\,\mathrm{Ro} - \mathrm{Ri}^3\,\mathcal{T}\mathrm{p} + \mathrm{Ro}^3\,\mathcal{T}\mathrm{p} + 3\,\mathrm{Ro}^2\left(-\sqrt{\mathcal{T}\mathrm{p}} + \frac{2\left(-\sqrt{\mathcal{T}\mathrm{p}} + \mathrm{Ri}\,\mathcal{T}\mathrm{p}\right)}{-1 + e^{2\,(-\mathrm{Ri}+\mathrm{Ro})\,\sqrt{\mathcal{T}\mathrm{p}}}\left(1 + \mathrm{Ri}\,\sqrt{\mathcal{T}\mathrm{p}}\right) + \mathrm{Ri}\,\sqrt{\mathcal{T}\mathrm{p}}}\right)\Bigg)\,(\mathrm{bcp}\,\rho\mathrm{c} + \mathrm{blp}\,\rho\mathrm{l})\Bigg)\Big/\left(3\,\mathrm{Kp}\left(\mathrm{Ri}^3 - \mathrm{Ro}^3\right)\mathcal{T}\mathrm{p}^2\,\rho\mathrm{l}\right);$$

$$\mathrm{h6} = \Big(\mathrm{Ri}^2\,(\mathrm{bcp}\,\rho\mathrm{c} + \mathrm{blp}\,\rho\mathrm{l})\,\Big(1 + \left(\mathrm{Ro}\,\sqrt{\mathcal{T}\mathrm{p}}\right)\Big/\Big(-\mathrm{Ri}\,\sqrt{\mathcal{T}\mathrm{p}}\,\mathrm{Cosh}\Big[(\mathrm{Ri}-\mathrm{Ro})\,\sqrt{\mathcal{T}\mathrm{p}}\Big] + \mathrm{Sinh}\Big[(\mathrm{Ri}-\mathrm{Ro})\,\sqrt{\mathcal{T}\mathrm{p}}\Big]\Big)\Big)\Big)\Big/\left(\mathrm{kp}\,\mathrm{Kp}\left(\mathrm{Ri}^3 - \mathrm{Ro}^3\right)\mathcal{T}\mathrm{p}\,\rho\mathrm{l}\right);$$

$$\mathrm{h7} = \left(\mathrm{Ro}\,(\mathrm{bcp}\,\rho\mathrm{c} + \mathrm{blp}\,\rho\mathrm{l})\left(1 + \frac{\mathrm{Ri}\,\mathrm{Ro}\,\mathcal{T}\mathrm{p}}{-1 + \mathrm{Ri}\,\sqrt{\mathcal{T}\mathrm{p}}\,\mathrm{Coth}\Big[(\mathrm{Ri}-\mathrm{Ro})\,\sqrt{\mathcal{T}\mathrm{p}}\Big]} + \frac{\mathrm{Ro}\,\sqrt{\mathcal{T}\mathrm{p}}}{-\mathrm{Ri}\,\sqrt{\mathcal{T}\mathrm{p}} + \mathrm{Tanh}\Big[(\mathrm{Ri}-\mathrm{Ro})\,\sqrt{\mathcal{T}\mathrm{p}}\Big]}\right)\right)\Big/\left(\mathrm{Kp}\left(\mathrm{Ri}^3 - \mathrm{Ro}^3\right)\mathcal{T}\mathrm{p}\,\rho\mathrm{l}\right);$$

```
g1 = ηl (Kp Zz (kp - bp h5 s Vv ηl) (Sca ρc φoa + ρl (Bb ΔT + ΔTtimesSatagg - Sca φoa)) +
        ba (h4 kp Kp Ww Zz ρl + h7 kp Kp Papp Ww Zz ρl + h6 kp Kp Qint Ww Zz ρl +
           h3 kp Kp Xx Zz ρl + h1 kp Kp Qint Xx Zz ρl + bp h3 h5 Kp s Uu Ww Zz ηl ρl +
           bp h1 h5 Kp Qint s Uu Ww Zz ηl ρl - bp h3 h5 Kp s Vv Xx Zz ηl ρl -
           bp h1 h5 Kp Qint s Vv Xx Zz ηl ρl + Dd h5 Kp s Ww Zz ΔT ηl ρl +
           h5 Kp s Ww Zz ΔTtimesSatpas ηl ρl + kp Kp Ro^3 ρl σapp -
           bp h5 Kp Ro^3 s Vv ηl ρl σapp + bp h5 Ka Ro^3 s Ww ηl ρl σapp +
           h5 Kp s Scp Ww Zz ηl ρc φop - h5 Kp s Scp Ww Zz ηl ρl φop +
           2 Kp Ro^3 (kp + bp h5 s (-Vv + Ww) ηl) ρl σapp χp)) /
      (Kp Zz (ka (kp - bp h5 s Vv ηl) + ba h2 s ηl (-kp Xx + bp h5 s (-Uu Ww + Vv Xx) ηl))
        ρl) //. Qint → QINT;
g2 = ηl (Kp Zz (ka - ba h2 s Xx ηl) (Scp ρc φop + ρl (Dd ΔT + ΔTtimesSatpas - Scp φop)) +
        bp (h3 ka Kp Uu Zz ρl + h1 ka Kp Qint Uu Zz ρl + h4 ka Kp Vv Zz ρl + h7 ka Kp
            Papp Vv Zz ρl + h6 ka Kp Qint Vv Zz ρl + ba h2 h4 Kp s Uu Ww Zz ηl ρl +
           ba h2 h7 Kp Papp s Uu Ww Zz ηl ρl + ba h2 h6 Kp Qint s Uu Ww Zz ηl ρl -
           ba h2 h4 Kp s Vv Xx Zz ηl ρl - ba h2 h7 Kp Papp s Vv Xx Zz ηl ρl -
           ba h2 h6 Kp Qint s Vv Xx Zz ηl ρl + Bb h2 Kp s Uu Zz ΔT ηl ρl +
           h2 Kp s Uu Zz ΔTtimesSatagg ηl ρl + ka Ka Ro^3 ρl σapp +
           ba h2 Kp Ro^3 s Uu ηl ρl σapp - ba h2 Ka Ro^3 s Xx ηl ρl σapp +
           h2 Kp s Sca Uu Zz ηl ρc φoa - h2 Kp s Sca Uu Zz ηl ρl φoa +
           2 Kp Ro^3 (ka + ba h2 s (Uu - Xx) ηl) ρl σapp χp)) /
      (Kp Zz (ka (kp - bp h5 s Vv ηl) + ba h2 s ηl (-kp Xx + bp h5 s (-Uu Ww + Vv Xx) ηl))
        ρl) //. Qint → QINT;
```

$$\text{Cpla} = \frac{\text{Aa s}}{\text{Ka Mca Mla Zz } \rho\text{l}};$$

$$\text{Cplp} = \frac{\text{Cc s}}{\text{Kp Mcp Mlp Zz } \rho\text{l}};$$

$$\tau\text{a} = \frac{\eta\text{l}}{\text{ka}} \text{ Cpla};$$

$$\tau\text{p} = \frac{\eta\text{l}}{\text{kp}} \text{ Cplp};$$

Inputs

This section contains all the required inputs.

Applied Temperature and Pressure

Applied pressure at the boundary of the sphere in the time domain:

```
Papptime = 0;
```

Applied pressure at the boundary in the transformed domain:

```
Papp = LaplaceTransform[Papptime, t, s];
```

Applied stress at the boundary in the transformed domain:

```
σapp = -Papp;
```

Applied temperature at the boundary in the time domain:

```
Tamp = 25;
```

```
T = Tamp HeavisideTheta[t]
```

```
25 HeavisideTheta[t]
```

```
ΔTt = T
```

```
25 HeavisideTheta[t]
```

Applied temperature at the boundary in the transformed domain:

```
ΔT = LaplaceTransform[ΔTt, t, s];
```

Geometry

Diameter of the aggregate core in inches:

```
Di = 2;
```

Radius of the aggregate core in meters:

$$\mathrm{Ri} = \frac{\mathrm{Di}}{2} * \frac{2.54}{100}$$

```
0.0254
```

Dry-rodded aggregate volume fraction in percentage according to the ACI mixture design (Table 10.8, Mindess et al. [22]) :

```
AggVolPercent = 75;
```

Outer radius of the matrix shell in meters

$$\mathrm{Ro} = \mathrm{Round}\left[\left(\frac{100\,\mathrm{Ri}^3}{\mathrm{AggVolPercent}}\right)^{\frac{1}{3}},\ 0.0001\right]$$

```
0.028
```

Material Properties

- **Density** $\left(\frac{kg}{m^3}\right)$

Density of the pore liquid:

$$\rho l = 0.9998 \times 10^3;$$

Density of the pore crystal:

$$\rho c = 0.9167 \times 10^3;$$

- **Porosity**

Porosity of the aggregate:

```
ϕoa = 0.2;
```

Porosity of the matrix:

$\phi op = 0.2;$

- **Permeability (m^2)**

Permeability of the aggregate:

$ka = 1 \times 10^{-21};$

Permeability of the matrix:

$kp = 1 \times 10^{-21};$

- **Thermal Expansion Coefficient (Degree C)**

Thermal expansion coefficient of the aggregate:

$\alpha a = 10 \times 10^{-6};$

Thermal expansion coefficient of the matrix:

$\alpha p = 10 \times 10^{-6};$

Thermal expansion coefficient of the pore liquid:

$$\alpha l = -\frac{286.3 \times 10^{-6}}{3};$$

Thermal expansion coefficient of the pore crystal

$$\alpha c = \frac{155 \times 10^{-6}}{3};$$

- **Bulk Modulus $(\mathrm{N\,m} / \mathrm{hr}^2)$**

Bulk modulus of the pore liquid:

$Kl = 1.79 \times 10^{3} * 1.30 \times 10^{13};$

Bulk modulus of the pore crystal:

$Kc = 7.81 \times 10^{3} * 1.30 \times 10^{13};$

Bulk modulus of the solid aggregate skeleton:

$Ksa = 45 \times 10^{3} * 1.30 \times 10^{13};$

Bulk modulus of the solid matrix skeleton:

$Ksp = 45 \times 10^{3} * 1.30 \times 10^{13};$

Bulk modulus of the porous aggregate:

$Ka = (1 - \phi oa)^{2} * Ksa;$

Bulk modulus of the porous matrix:

$Kp = (1 - \phi op)^{2} * Ksp;$

- **Poisson's Ratio**

Poisson's ratio of the aggregate:

$va = 0.2;$

Poisson's ratio of the matrix:

$vp = 0.2;$

- **Fluid Viscosity (N m / hr)**

  $\eta l = 1.79\times 10^{-9} * 3.6\times 10^{9};$

- **Melting Entropy $\left(\frac{\text{N m/hr}^2}{K}\right)$**

  $\mathcal{S}m = 1.2 * 1.30\times 10^{13};$

- **Capillary Modulus (MPa) (Coussy, 2005 [29])**

  Capillary modulus of the aggregate:

  $\mathcal{N}a = 35;$

  Capillary modulus of the matrix:

  $\mathcal{N}p = 35;$

- **Characteristic Cooling (Empirical: $\mathcal{T}$ in K and $\mathcal{N}$ in MPa) (Coussy, 2005 [29])**

  Characteristic cooling of the aggregate:

  $\mathcal{T}a = 0.4734\,\mathcal{N}a\;;$

  Characteristic cooling of the matrix:

  $\mathcal{T}p = 0.4734\,\mathcal{N}p\;;$

- **Pore Size Distribution (0-1) (Coussy, 2005 [29])**

  Pore size distribution of the aggregate:

  `ma = 0.5;`

  Pore size distribution of the matrix:

  `mp = 0.5;`

Degree of Saturation

Liquid saturation in aggregate in the time domain:

$$\text{Slatime} = \left(1+\left(\frac{1}{\mathcal{T}a}\,(\Delta\text{Tt})\right)^{\frac{1}{1-\text{ma}}}\right)^{-\text{ma}};$$

Liquid saturation in aggregate in the transformed domain:

```
Slatrans = LaplaceTransform[Slatime, t, s];
Sla = Slatrans;
```

Liquid saturation in matrix in the time domain:

$$\text{Slptime} = \left(1+\left(\frac{1}{\mathcal{T}p}\,(\Delta\text{Tt})\right)^{\frac{1}{1-\text{mp}}}\right)^{-\text{mp}};$$

Liquid saturation in matrix in the transformed domain:

```
Slptrans = LaplaceTransform[Slptime, t, s];
Slp = Slptrans;
```

Crystal saturation in aggregate in the time domain:

```
Scatime = 1 - Slatime;
```

Crystal saturation in aggregate in the transformed domain:

```
Scatrans = LaplaceTransform[Scatime, t, s];
Sca = Scatrans;
```

Crystal saturation in matrix in the time domain:

```
Scptime = 1 - Slptime;
```

Crystal saturation in matrix in the transformed domain:

```
Scptrans = LaplaceTransform[Scptime, t, s];
Scp = Scptrans;
```

Properites That Are Functions of S_l

- **Biot's Coefficient**

Biot's coefficient of aggregate:

$$ba = 1 - \frac{Ka}{Ksa};$$

Biot's coefficient of matrix:

$$bp = 1 - \frac{Kp}{Ksp};$$

Biot's coefficient of crystal in the aggregate pore in the time domain

```
bcatime = ba Scatime;
```

Biot's coefficient of crystal in the aggregate pore in the transformed domain

```
bcatrans = ba Scatrans;
bca = s bcatrans;
```

Biot's coefficient of liquid in the aggregate pore in the time domain

```
blatime = ba Slatime;
```

Biot's coefficient of liquidl in the aggregate pore in the transformed domain

```
blatrans = ba Slatrans;
bla = s blatrans;
```

Biot's coefficient of crystal in the matrix pore in the time domain

```
bcptime = bp Scptime;
```

Biot's coefficient of crystal in the matrix pore in the transformed domain

```
bcptrans = bp Scptrans;
bcp = s bcptrans;
```

Biot's coefficient of liquid in the matrix pore in the time domain

```
blptime = bp Slptime;
```

Biot's coefficient of liquid in the matrix pore in the transformed domain

```
blptrans = bp Slptrans;
```

```
blp = s blptrans;
```

Biot's Modulus

Biot's modulus of crystals in the aggregate pore in the time domain:

$$\text{Mcatime} = \frac{1}{\frac{\text{bcatime}-\phi\text{oa Scatime}}{\text{Ksa}} + \frac{\phi\text{oa Scatime}}{\text{Kc}}};$$

Biot's modulus of crystal in the aggregate pore in the transformed domain:

```
Mcatrans = LaplaceTransform[Mcatime, t, s];
```

```
Mca = s Mcatrans;
```

Biot's modulus of liquid in the aggregate pore in the time domain:

$$\text{Mlatime} = \frac{1}{\frac{\text{blatime}-\phi\text{oa Slatime}}{\text{Ksa}} + \frac{\phi\text{oa Slatime}}{\text{Kl}}};$$

Biot's modulus of liquid in the aggregate pore in the transformed domain:

```
Mlatrans = LaplaceTransform[Mlatime, t, s];
```

```
Mla = s Mlatrans;
```

Biot's modulus of crystals in the matrix pore in the time domain:

$$\text{Mcptime} = \frac{1}{\frac{\text{bcptime}-\phi\text{op Scptime}}{\text{Ksp}} + \frac{\phi\text{op Scptime}}{\text{Kc}}};$$

Biot's modulus of crystal in the matrix pore in the transformed domain:

```
Mcptrans = LaplaceTransform[Mcptime, t, s];
```

```
Mcp = s Mcptrans;
```

Biot's modulus of liquid in the matrix pore in the time domain:

$$\text{Mlptime} = \frac{1}{\frac{\text{blptime}-\phi\text{op Slptime}}{\text{Ksp}} + \frac{\phi\text{op Slptime}}{\text{Kl}}};$$

Biot's modulus of liquid in the matrix pore in the transformed domain:

```
Mlptrans = LaplaceTransform[Mlptime, t, s]
```

```
Mlp = s Mlptrans ;;
```

Biot's modulus of aggregate in the time domain:

$$\text{Matime} = \frac{1}{\frac{1}{\text{Mcatime}} + \frac{1}{\text{Mlatime}}};$$

Biot's modulus of aggregate in the transformed domain:

```
Matrans = LaplaceTransform[Matime, t, s];
```

```
Ma = s Matrans;
```

Biot's modulus of matrix in the time domain:

$$\mathtt{Mptime} = \frac{1}{\frac{1}{\mathtt{Mcptime}} + \frac{1}{\mathtt{Mlptime}}};$$

Biot's modulus matrix in the transformed domain:

```
Mptrans = LaplaceTransform[Mptime, t, s];
Mp = s Mptrans;
```

Variables that are functions of both ΔT and degree of saturation

```
ΔTSatagg = 3 (-Scatime αa - Slatime αa + Scatime αc + Slatime αl) ϕoa ΔTt;
ΔTSatpas = 3 ((Scptime αc + Slptime αl) ϕop + (-Scptime - Slptime) αp ϕop) ΔTt;
ΔTtimesSatagg = LaplaceTransform[ΔTSatagg, t, s];
ΔTtimesSatpas = LaplaceTransform[ΔTSatpas, t, s];
```

Inversion to time domain

The following commands invert the required outputs in the time domain from the Laplace transformed domain using the Stehfest Algorithm.

```
PI = NLInvSteh[QINT, s, t, 6];
```

$$\mathtt{PAL} = \frac{\mathtt{NLInvSteh[Pla,\ s,\ t,\ 6]}}{1.30 \times 10^{13}};$$

$$\mathtt{PPL} = \frac{\mathtt{NLInvSteh[Plp,\ s,\ t,\ 6]}}{1.30 \times 10^{13}};$$

```
εkA = NLInvSteh[εka, s, t, 6];
εkP = NLInvSteh[εkp, s, t, 6];
εkkAVE = NLInvSteh[εkkave, s, t, 6];
```

$$\mathtt{\sigma tA} = \frac{\mathtt{NLInvSteh[\sigma ta,\ s,\ t,\ 6]}}{1.30 \times 10^{13}};$$

$$\mathtt{\sigma tP} = \frac{\mathtt{NLInvSteh[\sigma tp,\ s,\ t,\ 6]}}{1.30 \times 10^{13}};$$

```
σrA = NLInvSteh[σra, s, t, 2];
σrP = NLInvSteh[σrp, s, t, 2];
εtA = NLInvSteh[εta, s, t, 6];
εtP = NLInvSteh[εtp, s, t, 6];
εrA = NLInvSteh[εra, s, t, 6];
εrP = NLInvSteh[εrp, s, t, 6];
εRP = NLInvSteh[εrp, s, t, 6];
```

Check Initial Value

Initial values are checked here using the obtained results. Results are considered accurate if mw ≈ 0.

$$\mathcal{V}\Delta\rho\mathrm{a} = \mathtt{Stehfest}\left[\mathtt{Sca}\left(-1+\frac{\rho\mathrm{c}}{\rho\mathrm{l}}\right)\phi\mathtt{oa},\ \mathtt{s},\ \mathtt{t},\ 6\right]\ \mathtt{//.}\ \mathtt{t}\to 1$$

```
-0.00743987
```

$$\mathcal{V}\Delta\rho\mathrm{p} = \mathtt{Stehfest}\left[\left(\frac{\rho\mathrm{c}}{\rho\mathrm{l}}-1\right)\phi\mathtt{op}\ \mathtt{Scp},\ \mathtt{s},\ \mathtt{t},\ 6\right]\ \mathtt{//.}\ \mathtt{t}\to 1$$

```
-0.00743987
```

```
𝒱ϕa = Stehfest[(Aa Pla + Mla ρl
          (Bb ΔT + ba Ka Mca (Xx Zz ϵfaaver + Ww Zz ϵfpaver + Ro³ (1 + 2 χp) σapp))) /
    (Ka Mca Mla Zz ρl), s, t, 6] //. {r → 0.01 Ri, t → 0.000001}
```

```
{{{0.00747706}}}
```

```
𝒱ϕp = Stehfest[(Cc Plp + Mlp ρl (Dd ΔT +
            bp Mcp (Kp Uu Zz ϵfaaver + Kp Vv Zz ϵfpaver + Ro³ (Ka + 2 Kp χp) σapp))) /
    (Kp Mcp Mlp Zz ρl), s, t, 6] //. {r → Ri + 1 / 2 (Ro - Ri), t → 0.00001}
```

```
{{{0.00747706}}}
```

```
mwa = 𝒱Δρa + 𝒱ϕa
```

```
{{{0.0000371845}}}
```

```
mwp = 𝒱Δρp + 𝒱ϕp
```

```
{{{0.0000371845}}}
```

$$\mathtt{Aggerror} = \frac{\mathtt{mwa}}{\mathcal{V}\Delta\rho\mathrm{a}} * 100$$

```
{{{-0.4998}}}
```

$$\mathtt{Pasteerror} = \frac{\mathtt{mwp}}{\mathcal{V}\Delta\rho\mathrm{p}} * 100$$

```
{{{-0.4998}}}
```

Example Plots

Predicting Damage

```
LogLinearPlot[{PAL //. r → 0.01 Ri, PAL //. r → 0.5 Ri, PAL //. r → Ri,
  PPL //. r → Ri, PPL //. r → (Ri + 0.5 (Ro - Ri)), PPL //. r → Ro}, {t, 0.0001, 100},
 PlotLegend → {Style["p_l^a near center", 16], Style["p_l^a at r=1.27 cm", 16],
   Style["p_l^a at r=2.54 cm (agg-matrix interface)", 16],
   Style["p_l^p at r=2.54 cm (agg-matrix interface)", 16], Style["p_l^p at r=2.67 cm", 16],
   Style["p_l^p at r=2.8 cm (surface)", 16]}, LegendShadow → None,
 LegendBorder → Black, LegendPosition → {0.25, 0.1}, Frame → True,
 FrameLabel → {"Time (hr)", "Liquid  Pressure, p_l  (MPa)"}, LabelStyle → {16},
 PlotStyle → {{Black}, {Black, Dashing[0.02], Thick}, {Black, Dotted, Thick},
   {Black, Thick, Dashing[0.04]}, {Black, Thick, Dashing[0.06]}, {Black, Thick}}]
```

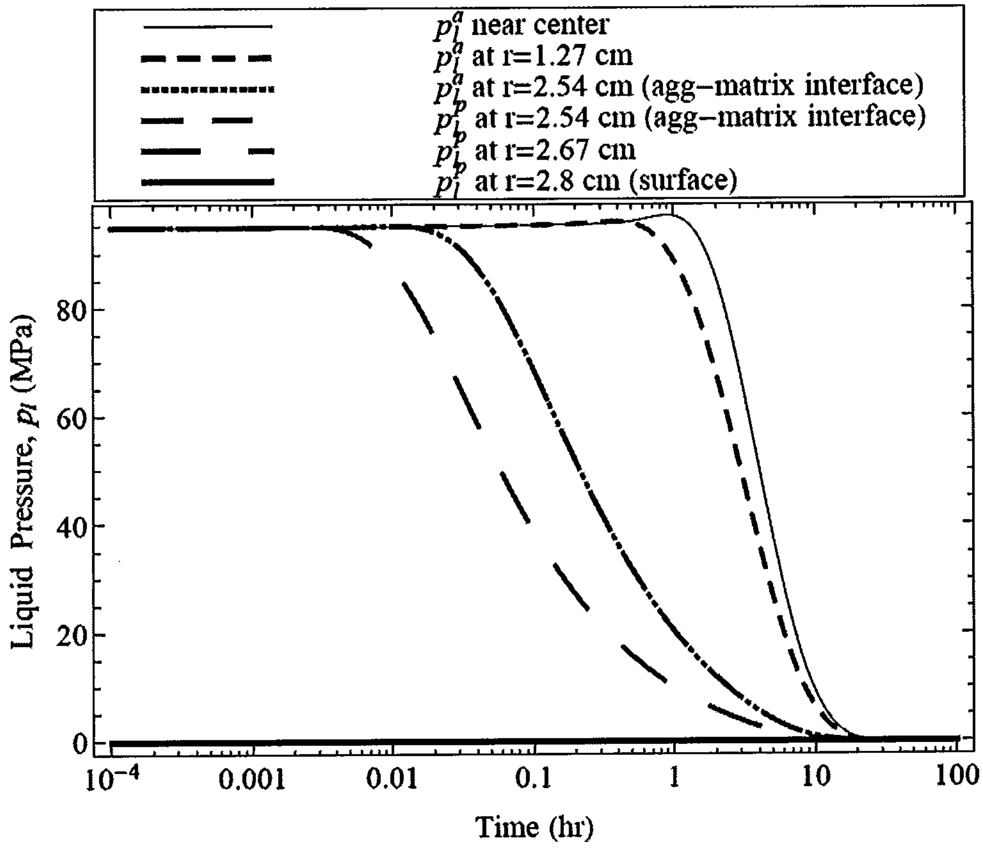

```
LogLinearPlot[{σtA //. r → 0.1 Ri, σtA //. r → 0.5 Ri, σtA //. r → Ri,
  σtP //. r → Ri, σtP //. r → (Ri + 0.5 (Ro - Ri)), σtP //. r → Ro}, {t, 0.0001, 100},
 PlotLegend → {Style["σ_θ^a near center", 16], Style["σ_θ^a at r=1.27 cm", 16],
   Style["σ_θ^a at r=2.54 cm (agg-matrix interface)", 16],
   Style["σ_θ^p at r=2.54 cm (agg-matrix interface)", 16],
   Style["σ_θ^p at r=2.67 cm", 16], Style["σ_θ^p at r=2.8 cm (surface)", 16]},
 LegendShadow → None, LegendBorder → Black, LegendPosition → {0.25, 0.1},
 Frame → True, FrameLabel → {"Time (hr)", "Tangential   Stress, σθ(MPa)"},
 LabelStyle → {16}, PlotStyle →
  {{Black}, {Black, Thick}, {Black, Dotted, Thick}, {Black, Dashing[0.02], Thick},
   {Black, Thick, Dashing[0.04]}, {Black, Thick, Dashing[0.06]}}]
```

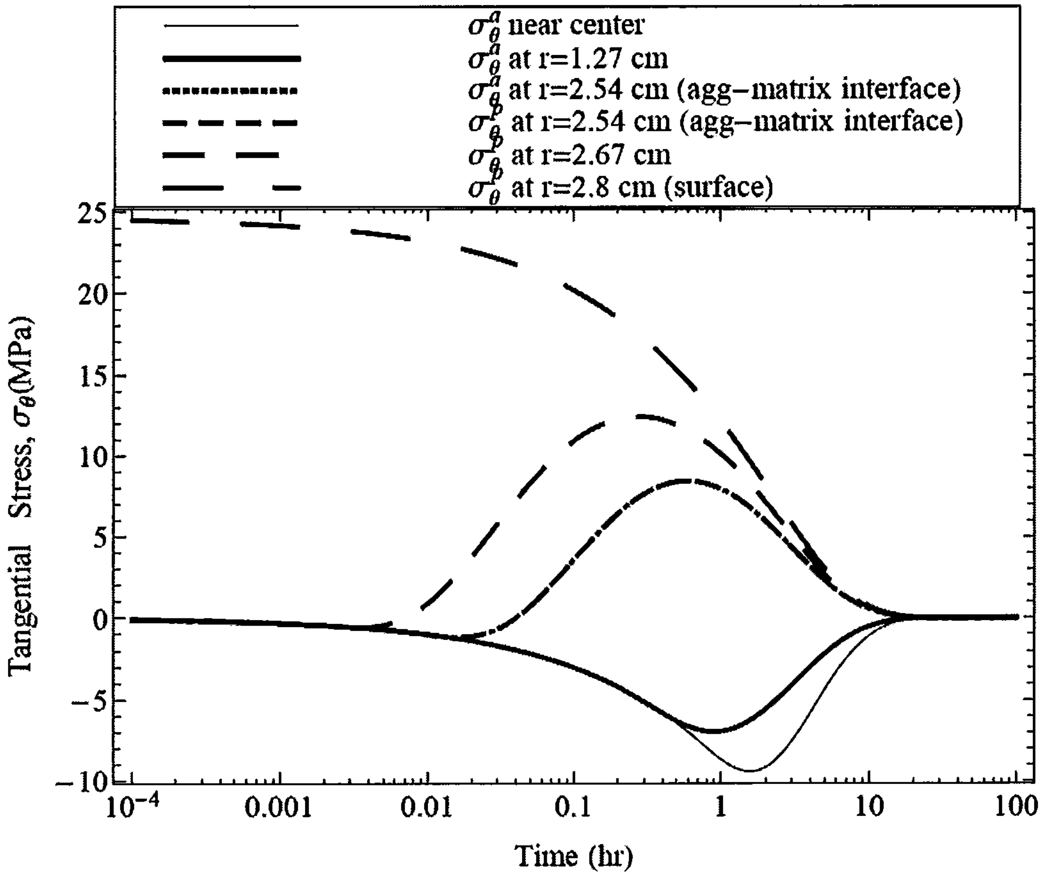

```
LogLinearPlot[{ϵkA //. r → 0.01 Ri, ϵkA //. r → 0.5 Ri, ϵkA //. r → Ri,
  ϵkP //. r → Ri, ϵkP //. r → (Ri + 0.5 (Ro - Ri)), ϵkP //. r → Ro}, {t, 0.0001, 100},
 PlotLegend → {Style["ϵ_kk^a near center", 16], Style["ϵ_kk^a at r=1.27 cm", 16],
   Style["ϵ_kk^a at r=2.54 cm (agg-matrix interface)", 16],
   Style["ϵ_kk^p at r=2.54 cm (agg-matrix interface)", 16], Style["ϵ_kk^p at r=2.67 cm", 16],
   Style["ϵ_kk^p at r=2.8 cm (surface)", 16]}, LegendShadow → None,
 LegendBorder → Black, LegendPosition → {0.25, 0.1}, Frame → True,
 FrameLabel → {"Time (hr)", "Bulk  Strain, ϵkk"}, LabelStyle → {16}, PlotStyle →
  {{Black}, {Black, Thick}, {Black, Dotted, Thick}, {Black, Dashing[0.02], Thick},
   {Black, Thick, Dashing[0.04]}, {Black, Thick, Dashing[0.06]}}]
```

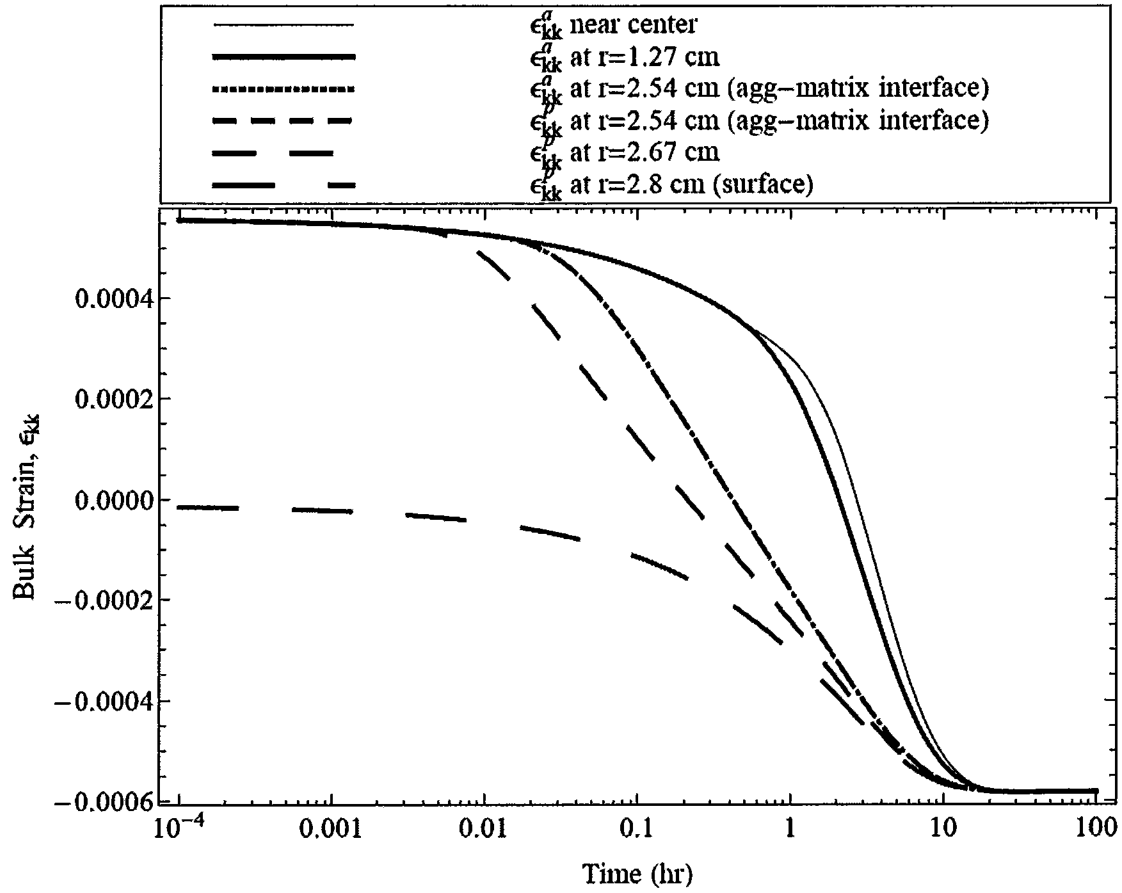

Check with the solution obtained by Coussy and Monteiro [15]

$$\mathrm{Aa} = \frac{1}{1 - \left(1 - \frac{\rho c}{\rho 1}\right) \frac{\mathrm{Ka\,Ma}}{\mathrm{Ka} + \mathrm{ba}^2\,\mathrm{Ma}} \left(\frac{1}{\mathrm{Mca}} + \frac{\mathrm{ba\,bca}}{\mathrm{Ka}}\right)}$$

1.01566

$$\mathrm{Plcryo} = \frac{\frac{-\mathrm{Aa\,Ka\,Ma}}{\mathrm{Ka} + \mathrm{ba}^2\,\mathrm{Ma}}\, \mathbb{S}\mathrm{m}\ \mathrm{Tamp} \left(\frac{1}{\mathrm{Mca}} + \frac{\mathrm{ba\,bca}}{\mathrm{Ka}}\right)}{1.30 \times 10^{13}}$$

-5.65062

$$\mathrm{plhydrau} = \frac{\frac{\mathrm{Aa\,Ka\,Ma}}{\mathrm{Ka} + \mathrm{ba}^2\,\mathrm{Ma}} \left(1 - \frac{\rho c}{\rho 1}\right) \phi \mathrm{oa\ Scatime}}{1.30 \times 10^{13}} \ //.\ t \to 0.1$$

93.0101

$$\mathrm{plthermo} = \frac{3\, \frac{\mathrm{Aa\,Ka\,Ma}}{\mathrm{Ka} + \mathrm{ba}^2\,\mathrm{Ma}}\, \phi \mathrm{oa}\ (\alpha \mathrm{a} - \mathrm{Scatime}\ \alpha \mathrm{c} - \mathrm{Slatime}\ \alpha 1)\ \mathrm{Tamp}}{1.30 \times 10^{13}} \ //.\ t \to 0.1$$

7.42552

$$\mathrm{Pl} = \mathrm{Plcryo} + \mathrm{plhydrau} + \mathrm{plthermo}$$

94.785